Dynamical basis of cellular sensing and responsiveness to spatial-temporal signals

technische universität dortmund

Akhilesh Padmanabhan Nandan

Fakultät für Chemie und Chemische Biologie Technische Universität, Dortmund

Zur Erlangung des akademischen Grades eines

Doktors der Naturwissenschaften (Dr. rer. nat.)

March 2022

.

Abstract

Under physiological conditions, cells continuously sense and migrate in response to chemoattractant signals that are noisy, conflicting, and changing over time and space. This suggests cells exhibit seemingly opposed characteristics, such as robust maintenance of polarized state longer than the signal duration, while still remaining adaptive to novel signals. However, the dynamical mechanism that enables such sensing capabilities is still unclear. In this thesis, I propose a generic dynamical mechanism based on critical positioning of receptor signaling network in the vicinity of saddle-node of a sub-critical pitchfork bifurcation (SubPB mechanism). The critical organization leads to the emergence of a dynamical "ghost" that gives transient memory in the polarized response, as well as the ability to continuously adapt to changes in signal localization. Using weakly nonlinear analysis, an analytical description of the necessary conditions for the existence of this mechanism in a general receptor network is provided. Comparing to three classes of existing mathematical models for polarization that operate on the principle of stable attractors, I demonstrate that the metastability arising from "ghost" in the SubPB mechanism uniquely enables sensing dynamic spatial-temporal signals in a history-dependent manner. By using a physical model that couples signaling to morphology, I demonstrate how this mechanism enables cells to navigate in changing environments. Using the well characterized Epidermal growth factor receptor (EGFR) sensing network in epithelial cells, I demonstrated that the described transient memory in signaling mimics working memory in neurons, enabling cells to process non-stationary signals.

Zusammenfassung

Unter physiologischen Bedingungen nehmen Zellen kontinuierlich Signale von Chemoattractanten wahr, die verrauscht, gegensätzlich und räumlich und zeitlich veränderlich sind. Dies deutet darauf hin, dass Zellen die scheinbar gegensätzlichen Anforderungen der Robustheit in der Polarisation über längere Zeiten als das Signal selbst, sowie die Anpassung an neue Signale erfüllen. Dennoch ist derzeit kein dynamischer Mechanismus der diese sensorischen Fähigkeiten ermöglicht bekannt. In dieser Thesis schlage ich einen generischen dynamischen Mechanismus auf Basis der kritischen Positionierung eines Rezeptorsignalnetzwerkes in der Nähe eines Sattel-Knotens einer sub-kritischen Pitchfork-Bifurkation (SubPB Mechanismus) vor. Die kritische Organisation führt zu der Entstehung eines dynamischen "Geistes", der ein transientes Gedächtnis einer Polarisation, sowie eine kontinuierliche Adaption an veränderte Signallokalisationen ermöglicht. Unter Verwendung der schwach nichtlinearen Analyse, wird eine analytische Beschreibung der notwendigen Bedingungen für die Existenz dieses Mechanismus in einem allgemeinen Rezeptornetzwerk geliefert. Mit einem Vergleich mit drei Klassen an existierenden mathematischen Modellen der Zellpolarisation, die das Prinzip der stabilen Attraktoren nutzen, demonstriere ich, dass nur die Metastabilität des "Geistes" des SubPB Mechanismus die Wahrnehmung von dynamischen raum-zeitlichen Signalen in einer geschichtsabhängigen Art ermöglicht. Durch ein physikalisches Modell, dass Signale mit der Zellmorphologie koppelt, zeige ich, dass dieser Mechanismus Zellen die Navigation in veränderlichen Umgebungen ermöglicht. Anhand des gut charakterisierten Signalnetzwerkes des epidermalem Wachstumsfaktorrezeptors (EGFR) demonstriere ich, dass das beschriebene transiente Gedächtnis in der Signalverarbeitung einem neuronalem Arbeitsgedächtnis ähnelt und die Verarbeitung nicht-stationärer Signale ermöglicht.

Contents

List of Figures

List of Tables

Abbreviations

Roman Symbols

EGF   Epidermal growth factor

EGFR   Epidermal growth factor receptor

GPCR   G-protein coupled receptors

GRN   Gene regulatory network

LEGI   Local excitation global inhibition

LPA   Local perturbation analysis

LSA   Linear stability analysis

PB   Pitchfork bifurcation

PTP   Protein tyrosine phosphatase

RTK   Receptor tyrosine kinase

SN   Saddle-node

TC   Transcritical

WNA   Weakly nonlinear analysis

WP   Wave pinning

Chapter 1

Introduction

1.1 Cellular sensing of non-stationary environment

Single cells sense different signals such as growth factors, cytokines etc. during physiological responses such as wound healing, embryogenesis, morphogenesis etc. [2, 3]. One of the defining features of living cells is their capacity to encode the extracellular information to an internal representation and to generate an optimal response.

A classic *in vitro* example demonstrating real-time information processing at the level of single cells is a human neutrophil that chases, engulfs and destroys a *Staphylococcus aureum* bacterium (Figure 1.1A). The neutrophil, a mere single cell rapidly adapts its direction of movement depending on the movement of the bacterium. In an *in vivo* setting, such capabilities aid immunological surveillance that requires coordinated movements of immune cells such as neutrophils, fibroblasts to combat invading pathogens. During inflammation, these cells can move rapidly and navigate through complex tissues over large distances to specific target inflammation sites [4]. During such pursuit cells encounter conflicting, simultaneous local gradient sources which they compare to direct their movement. *In vitro* studies have shown that fibroblast cells subjected to two simultaneous signal sources steer its migration direction towards the steepest gradient [5]. Similarly during embryonic development, short-range dynamic chemoattractant signals direct the migration of single cells to distant target regions as in the case of primordial germ cell (PGC) migration to somatic gonadal precursors (SGPs) in zebrafish, drosophila, mouse etc. [7, 2, 8]. During starvation conditions, a survival mechanism employed by social amoeba *Dictyostelium discoideum* requires cellular aggregation as the first step to trigger morphogenesis into fruiting bodies (Figure 1.1B). Non-dissipating waves of self-generated chemoattractant travel outward from aggregation centers and provide stable long-range cues to direct the migration of cells toward the wave source [9, 10]. The rising and falling part of a symmetrical wave that sweeps across
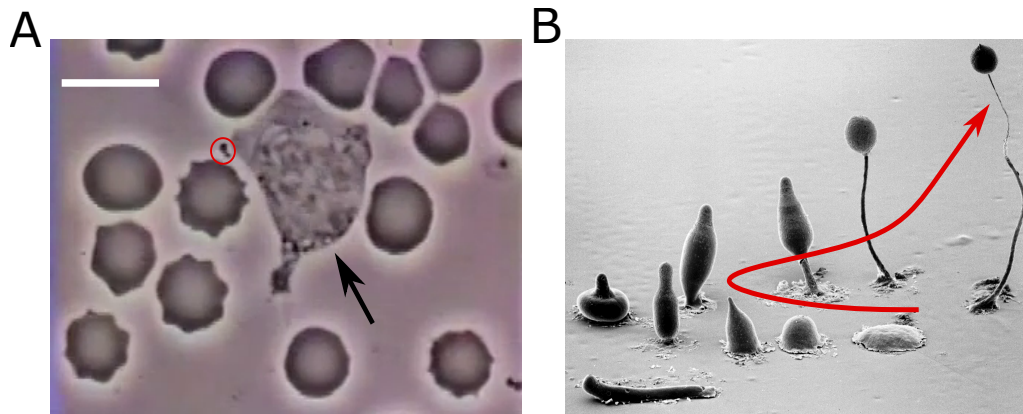
Figure 1.1 Examples of cellular response to non-stationary environments. A, A human neutrophil cell (black arrow) chasing a Staphylococcus aureus microorganism (red circle) on a blood film among red blood cells (imaged by David Rogers, courtesy of Thomas P. Stossel). Bar, 10 μm. B, SEM of *Dictyostelium discoideum* developmental stages showing coordinated morphogenetic response from aggregation to fruiting body formation [6] (courtesy of M.J. Grimson and R.L. Blanton, Texas Tech University). Red curved arrow: arrow of time.

the cells provides conflicting information about the gradient source. If the cells respond to simply spatial information, it would move forward in the front (rising part) of the wave and backward in the back (falling part) of the wave [11]. To overcome this conundrum cells require robust guidance mechanism that enables persistent directional migration. This poses the question, how cells achieve complex navigation in changing environment?

Cellular sensing was initially understood as process a by which external chemical ligands are binding and unbinding with receptors on the membrane. This stream of thought was first elaborated by Burg and Percell [12] in the context of chemotactic sensitivity of *Escherichia coli* bacteria. The study addressed the question - how receptor number and time limit the precision of sensing static ligand concentrations. In contrast to bacterial systems, eukaryotic cells exhibit high ligand affinity to receptor and activation of the receptors lead to rapid remodeling of the membrane through vesicular trafficking processes. Morover, receptors interaction with other proteins bring non linearity to its dynamics that Burg and Purcell's view didn't account for. Therefore, it requires that we need new approaches to understand ligand sensing in eukaryotes.

1.2   Real time signal sensing in cells.

In cells, membrane-bound receptor proteins play an essential role in translating extracellular signals into intracellular responses. However, the complexity of molecular details from

receptor sensing to cell's response hinders intuitive notions of how regulatory networks within cells functions. A course grained approach is therefore necessary to investigate dynamical properties of receptor networks giving rise to complex responses.

Receptor tyrosine kinases (RTKs) and G protein-coupled receptors (GPCRs) are the most prominent families of receptors that recognize variety of extra cellular ligands [13, 14]. They are both trans-membrane proteins that have extracellular domains that bind to ligand and undergo a ligand dependent canonical activation (Figure 1.2). This activation event causes structural and functional modifications to their intracellular regions and represents first step in receptor-mediated signal transduction.
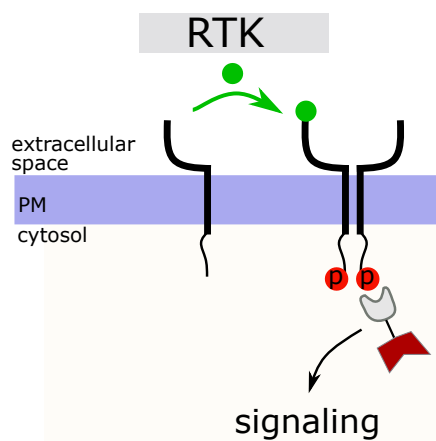
Figure 1.2 Canonical view of the ligand-induced dimerization and activation process of RTKs. For receptor tyrosine kinase (RTK), dimerization leads to trans phosphorylation and signal transduction. PM: Plasma membrane

In RTKs, the ligand binding induces dimerization and subsequent trans-phosphorylation at the cytoplasmic C-terminal tail of the receptor. The phosphorylated tyrosine residues further relay the signal downstream via scaffold proteins that are recruited to the phosphorylated tyrosine residues (Figure 1.2) [15–19]. Experimental evidences have shown that the receptors' activity can laterally propagate at the plasma membrane by sustaining their own activity in membrane areas unexposed to ligand, demonstrating ligand-independent activation processes based on an autocatalytic toggle switch reaction model [20–22].This process is initiated by liganded RTKs that could phosphorylate directly or indirectly (e.g., via RTK-phosphorylation-dependent recruitment of Src [23]) other RTK molecules forming transient dimers. For example for the Epidermal growth factor receptor (EGFR) the disassociated monomers that are phosphorylated on Y845 are catalytically active and can form transient dimers with ligandless EGFR, resulting in its autocatalytic phosphorylation [24–26].
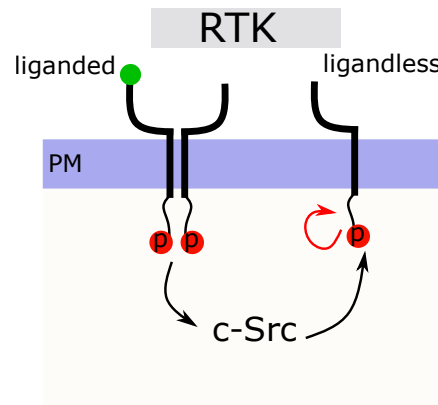
Figure 1.3 Ligand independent non canonical receptor phosphorylation mechanisms.
Autocatalytic activation of ligandless RTK mediated by c-Src. Arrows: Activating interactions. PM: Plasma membrane.

1.2.1 Spatial-temporal distribution of receptors through vesicular trafficking

Receptors that are activated at the membrane are internalized into plasma membrane derived vesicles and are trafficked into the cytoplasm. This process termed endocytosis typically happens within minutes of receptor activation. The vesicles carrying the receptors undergo a sorting process after which they are either recycled back to the membrane or are targeted for lysosomal degradation.

In RTK (Figure 1.4), both ligandless and liganded receptors are internalized, however liganded receptor undergoes a selective post-translational modification called Ubiquitination. This process is achieved via enzymes such as Ubiquitin ligase E3 that links a ubiquitin molecule to the cytoplasmic residues and later functions as a sorting determinant that enables vesicular re-routing [27]. These vesicles fuse into early endosomes that act as an endocytotic hub where liganded receptors are identified using the ubiquitin interacting protein containing proteins and transported to lysosomes for degradation. The remaining ligandless receptors are sent to recycling endosomes and are transported to the membrane. This recycling process is also accompanied by the deactivation process that involves phosphatases, thereby enabling replenishing of the plasma membrane with inactive receptors [25].

Vesicular trafficking mechanism that consists of internalization of activated receptors accompanied by two distinct vesicular routes, recycling or degradation, is therefore typical for RTKs and likely also for GPCRs [28]. While the unidirectional degradation route decrease the number of receptors on the membrane, recycling plays an important role by continuously
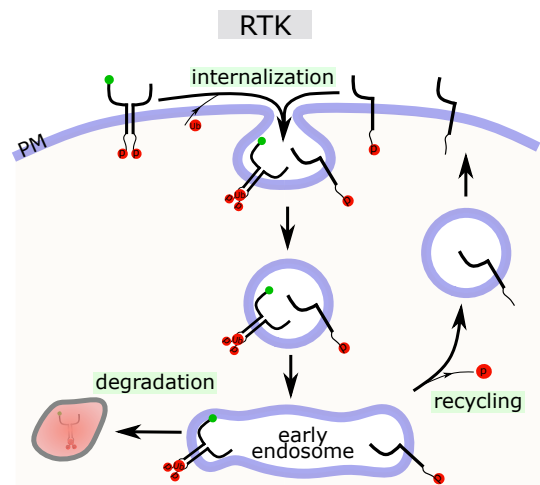
Figure 1.4 Schematic representation of vesicular trafficking of receptors. For receptor tyrosine kinase (RTK), internalization via endocytosis of ligandless and ubiquitinated liganded receptors. From the early endosomes, liganded receptors continue on the unidirectional route towards lysosomal degradation, whereas the unliganded receptors exit and are recycled back to the PM after dephosphorylation.

populating the plasma membrane with non-phosphorylated, ligandless receptors. These receptors therefore function as sensing entities of upcoming signals.

1.2.2 Vesicular trafficking establishes spatially extended biochemical networks that dictates ligand sensing

The receptors that are phosphorylated, either through ligand-dependent or independent processes at the plasma membrane undergo spatial cycles that re-distribute them within the cell (Figure 1.4). During this process, they interact with other proteins located at distinct cellular compartments. One of the major interacting partners of receptors is protein tyrosine phosphatases (PTPs) that dephosphorylate the receptors. Thus, different PTPs that are located at plasma membrane, cytosol or at membranes of intracellular organelles are key regulators of receptor signaling [29, 26, 22]

Throughout this thesis I will be using proto-oncogenic epidermal growth factor receptor (EGFR) as a typical example to represent RTK family. EGFR not only senses the presence of extracellular growth factors, but also interprets the complex dynamic growth factor patterns that can lead to diverse, functionally opposed cellular responses including proliferation, survival, apoptosis, differentiation, and migration [30, 26]. A recent study of EGFR signaling has revealed that the major PTPs that dephosphorylate EGFR are on the plasma membrane
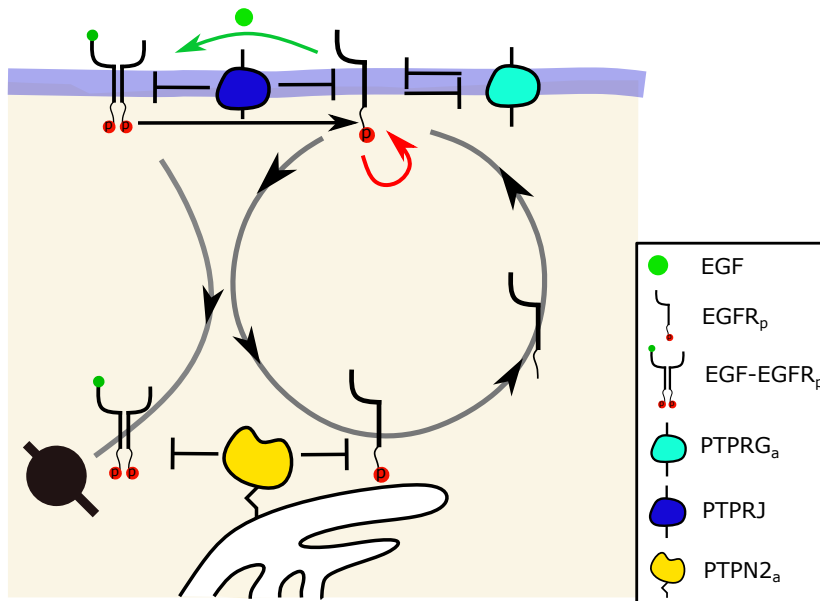
Figure 1.5 EGFR phosphorylation dynamics is regulated through interaction with PTPs in space. At the plasma membrane, ligand dependent and independent EGFR phosphorylation. ROS mediates a double-negative feedback between monomeric EGFR and PTPRGa, whereas PTPRJ negatively regulates EGFR phosphorylation. A negative feedback between EGFR and PTPN2a is established by vesicular recycling. Causal links: solid black lines. Vesicular trafficking: gray lines with black arrows (adapted from [25])

and the endoplasmic reticulum, and the vesicular trafficking of phosphorylated EGFR unifies the interactions with these PTPs into a network architecture whose sensing dynamics dictates responsiveness to time-varying growth factor signals [1].

The uncovered biochemical network (Figure 1.5) consists of multiple feedback interactions between EGFR and PTPs that are spatially segregated. In the study, dynamic signatures of EGFR phosphorylation response to EGF dose were analyzed to identify the type of underlying feedback motif and the findings were validated using genetic perturbations. It was identified that at the plasma membrane, ligandless, phosphorylated EGFR (EGFRp) interacts with two PTPs, PTPRG and PTPRJ. In addition to the dephosphorylation of the receptor by catalytically active PTPRG (PTPRGa), EGFRp-PTPRGa toggle switch interaction originates via EGFR-induced activation of H_2O_2 production by NADPH oxidases (NOX) [21, 31] that impairs the catalytic activity of PTPRG [1]. PTPRJ on the other hand constitutively interacts with both ligandless and liganded EGFR, and dephosphorylates them. While both species of receptors undergo distinct vesicular trafficking routes as in Figure 1.4A, they encounter ER-membrane bound PTP, PTPN2. The spatial recycling unifies various EGFR-PTP interaction motifs into a receptor network with EGFRp–PTPRGa toggle-switch with autocatalytic

EGFR activation at its core. This biochemical network in which receptor is embedded shapes the receptor dynamics and allows for the analysis of qualitatively different EGFR response that can arise. In order to systematically uncover the mechanism underlying the sensing capabilities of these networks, one can further use a dynamical systems theory approach [21, 1].

1.3   Bifurcation analysis enables identification of biochemical network dynamics

Biochemical network motifs consist of one or more components that interact with each other mostly in a nonlinear way. These systems are often mathematically conceived as a system of ordinary or partial differential equations. Each equation in the system represents the reaction term that captures the rate of change of concentration of a component and how it depends on other components in the network. The reaction term also depends on system parameters such as rate constants, diffusion constants, etc. The variables that describe the state of the dynamical system are called the state variables and the set of all the possible values of the state variables is the state space (Figure 1.6A, an example from a two variable system). In such a state space, the set of points that are the future states resulting from a given initial state is a trajectory whose local directions is determined by the direction of "flow" (blue arrows) at that point which in turn depends on the reaction terms. As shown in the example (Figure 1.6A) the region in the state space where all flows converge to is called a global attractor and any trajectory starting from any random point will eventually ends up there. It is also possible that regions in the state space have entirely opposite feature and it repels the flows around them, causing none of the trajectories to reach it (Figure 1.6).

Existence of such attactors or repellers or their combination in a given system thus dictates its overall dynamics. Theoretically, the two cases shown in Figure 1.6 can be distinguished using a small amplitude external perturbation. The method assumes that the trajectory is currently residing in a region of state space and the nature of that region is unknown. Under a perturbation that drives a trajectory away from the region, if it returns asymptotically, it implies that the region is attracting or is a *stable steady state*. Alternatively, if the trajectory does not return, then it is a repeller or an *unstable steady state*.

In a given system, the number and nature of the stability of the steady states depend on the parameter values in the system. This idea has been widely explored in nonlinear dynamics to understand the dynamics of networks using bifurcation analysis. According to this method, depending on the parameter value, if the steady state structure changes then a
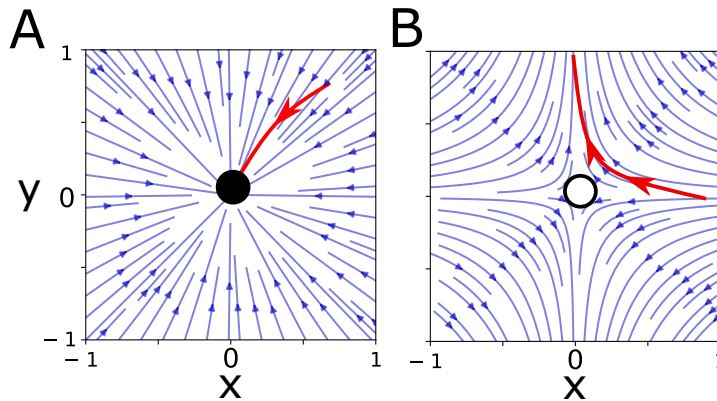
Figure 1.6 Schematic representation of two dimensional state space of an attractor (A) and a repeller (B) with their corresponding flows that dictates the evolution of trajectories. Filled/unfilled circle: stable/unstable state space region at the center of flow field. Blue arrow lines: state space flows. Red arrow lines: trajectory.

bifurcation has occurred [32]. Different types of transitions are characterized by different types of bifurcations and this knowledge helps to derive a better understanding of the system.

1.3.1 Quantitative measure of steady state stability using linear stability analysis

Consider a general two dimensional system given by,

$$\frac{dx}{dt} = f(x,y)$$
$$\frac{dy}{dt} = g(x,y)$$

$$(1.1)$$

where x and y are the variables of the system and $f(x,y)$, $g(x,y)$ are the reaction terms that govern the flow of the system. Let (x^*, y^*) be the steady state (*ss*) of the system. By definition, the rate of change of the system vanishes at the *ss*.

$$f(x^*, y^*) = 0$$
$$g(x^*, y^*) = 0$$

$$(1.2)$$

In linear stability analysis (LSA), to probe the stability of the steady state, the rate of decay/growth of a perturbation is quantified. The rate λ can be obtained by linearizing the system around the steady state by introducing a time-dependent perturbation of the form,

$$
\begin{aligned}
x(t) &= x^* + \delta x(t,\lambda) \\
y(t) &= y^* + \delta y(t,\lambda)
\end{aligned}
\tag{1.3}
$$

Plugging this perturbation into Eq. 1.1 and performing Taylor series expansion around the steady state yields a linearized equation,

$$
\begin{pmatrix} \dfrac{d\delta x(t)}{dt} \\ \dfrac{d\delta y(t)}{dt} \end{pmatrix} = \begin{pmatrix} \frac{\partial f}{\partial x} & \frac{\partial f}{\partial y} \\ \frac{\partial g}{\partial x} & \frac{\partial g}{\partial y} \end{pmatrix}_{(x^*,y^*)} \begin{pmatrix} \delta x(t) \\ \delta y(t) \end{pmatrix}
\tag{1.4}
$$

Where the matrix $J = \begin{pmatrix} \frac{\partial f}{\partial x} & \frac{\partial f}{\partial y} \\ \frac{\partial g}{\partial x} & \frac{\partial g}{\partial y} \end{pmatrix}_{(x^*,y^*)}$ is called the Jacobian matrix and the partial derivatives are evaluated at the steady state. The equation is further simplified by assuming an exponential time dependence for the perturbation.

$$
\begin{aligned}
\delta x(t) &= x_0 e^{(\lambda t)} \\
\delta y(t) &= y_0 e^{(\lambda t)}
\end{aligned}
\tag{1.5}
$$

where x_0 and y_0 are proportionality constants. Plugging this assumption about the perturbation into Eq. 1.4 yields its associated charateristic equation, with λ being the eigenvalue of the system.

$$
det(J - \lambda I) = 0
\tag{1.6}
$$

where I is the identity matrix. The solution to Eq. 1.6 gives λ, which is the rate of growth/decay of the perturbation and its algebric sign determines the stability of the steady state which is used to evaluate the Jacobian. If λ is positive *ss* is unstable and if λ is negative it is *ss* is stable. For an N-dimensional system, there are N λs associated with a particular steady state. In that case, the stability will be determined by the sign of the largest λ.

1.4 Different types of bifurcations and associated steady state transitions

In dynamical systems, there are fundamentally different bifurcations that dictates dynamical transitions such as saddle-node, transcritical, pitchfork bifurcation etc. Any given type of bifurcation can be realized through a large number of network topologies, thus they are not unique to a particular type of interaction topology. Therefore, prototypical examples of the form in Eq. 1.1 are used further in this section to demonstrate general steady state transitions associated with each bifurcation. Such simple representations are called normal forms and are fundamental to each bifurcation such that in any general system, around the bifurcation point, the steady state equations approximate to these forms [33].

1.4.1 Saddle node bifurcation

Consider the normal form equation,

$$
\begin{aligned}
\frac{dx}{dt} &= \mu - x^2 \\
\frac{dy}{dt} &= -y
\end{aligned}
\tag{1.7}
$$

where μ is the parameter in the system. This system has two steady states,

$$
(x^*, y^*) = (\pm\sqrt{\mu}, 0)
\tag{1.8}
$$

and they exist only for $\mu > 0$ and their eigenvalue estimation using Eq. 1.6 shows that $(\sqrt{\mu}, 0)$ is a stable and $(-\sqrt{\mu}, 0)$ is unstable (Figure 1.7A). As μ value changes from positive to negative, these steady states approach each other, collide when $\mu = 0$, and finally disappears for $\mu < 0$. The corresponding state space portrait shows that for $\mu > 0$, the stable steady state attracts the flow while the unstable state repels it (Figure 1.7B). Thus, any trajectory starting from an arbitrary state space point will eventually ends up in this stable attractor. At $\mu = 0$, the saddle point that exist at $(0,0)$ has features of stability and instability at the same time, by attracting trajectories from one side and repelling them from the other side. For $\mu < 0$, due to the absence of steady state, the trajectories diverge to infinity.
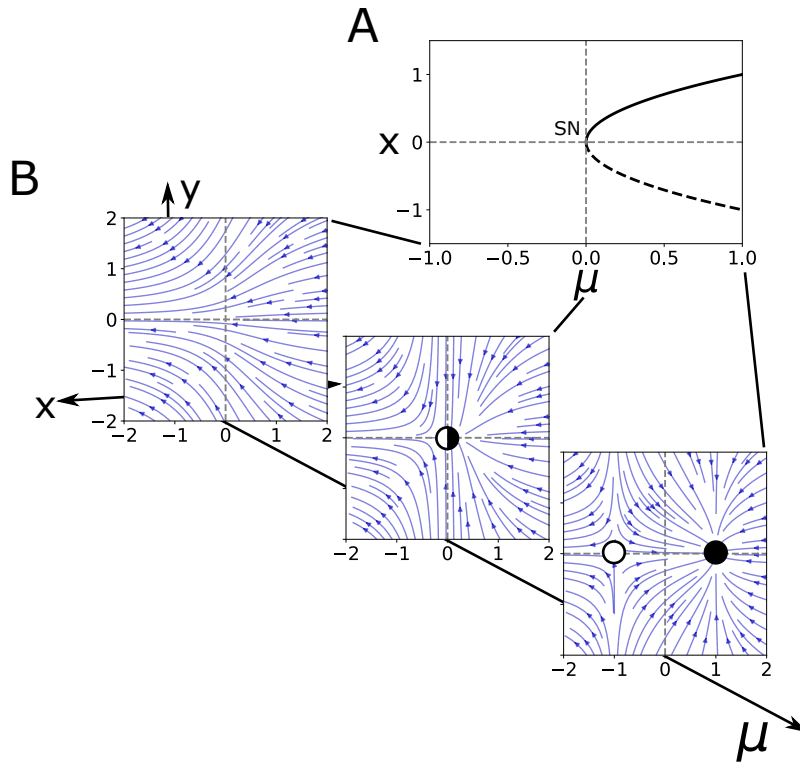
Figure 1.7 Saddle node bifurcation and corresponding state space transition. A, Bifurcation diagram showing a saddle-node bifurcation (Eq. 1.7). Black solid/dashed line: stable/unstable state. SN: Saddle node bifurcation. B, State space transition across μ corresponding to (A) showing steady states and their flows. Left: $\mu = -1$, middle: $\mu = 0$, right: $\mu = 1$. Filled/unfilled circle: stable/unstable steady state. Blue arrow lines: state space flows.

1.4.2   Transcritical bifurcation

The normal form associated with transcritical bifurcation has a different flow in the x-direction when compared with Eq. 1.7 and is given by,

$$
\begin{aligned}
\frac{dx}{dt} &= \mu x - x^2 \\
\frac{dy}{dt} &= -y
\end{aligned}
\tag{1.9}
$$

The largest eigenvalue associated with the two steady state of the system, $ss_1 = (\mu, 0)$ and $ss_2 = (0,0)$ are μ and $-\mu$ respectively. Thus, their stability is coupled together through μ. In the parameter space, when μ is negative ss_1 is stable and ss_2 is unstable. As the μ value crosses the origin, then these two fixed points exchanges the stability (Figure 1.8A).
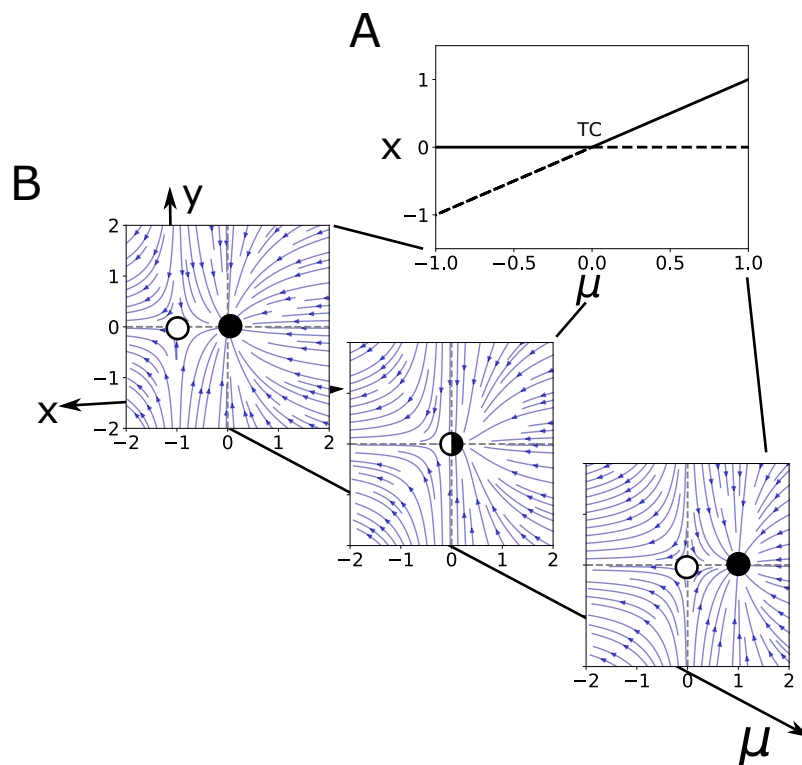
Figure 1.8 Transcritical bifurcation and corresponding state space transition. A, Bifurcation diagram showing transcritical bifurcation corresposning to Eq. 1.9. Black solid/dashed line: stable/unstable state. TC: transcritical bifurcation. B, State space transition across μ corresponding to (A) showing steady states and their flows around. Left: $\mu = -1$, middle: $\mu = 0$, right: $\mu = 1$. Filled/unfilled circle: stable/unstable steady state. Blue arrow lines: state space flows.

This exchange of stability between the steady states is the hallmark of transcitical bifurcation. Once the trivial state (ss_2) loses stability at the critical point, any further increase in parameter value leads the system to a nearby stable state ss_2 (Figure 1.8B). Eventhough the trivial state loses stability, in the vicinity of the TC point, its immediate neighbourhood has stable steady state that attracts the trajectories thereby rendering a continuous smooth transition across the bifurcation point. Such a lose of stability is "soft" and hence TC is a "soft" bifurcation ([34], chapter 6). When the parameter value is decreased, the system smoothly transits back to the trivial state.

1.4.3 Pitchfork bifurcation

When it comes to pitchfork bifurcation, there are two main types. Super-critical and sub-critical. The distinction between them is made depending on the stability of steady state

branches that that emerge at the bifurcation point. The super-critical pitchfork bifurcation is described by:

$$\begin{aligned} \frac{dx}{dt} &= \mu x - x^3 \\ \frac{dy}{dt} &= -y \end{aligned}$$

(1.10)

Because of the cubic term in the flow in the x-direction, there are three steady states for the system. $ss_1 = (0,0)$, $ss_2 = (\sqrt{\mu},0)$ and $ss_3 = (-\sqrt{\mu},0)$. The trivial state, ss_1 becomes unstable at a critical value $\mu = 0$, which marks the pitchfork bifurcation (PB) and the two new branches that exist for $\mu > 0$ are stable (Figure 1.9A). Similar to the TC bifurcation, super-critical PB enables a "soft" loss of stability.
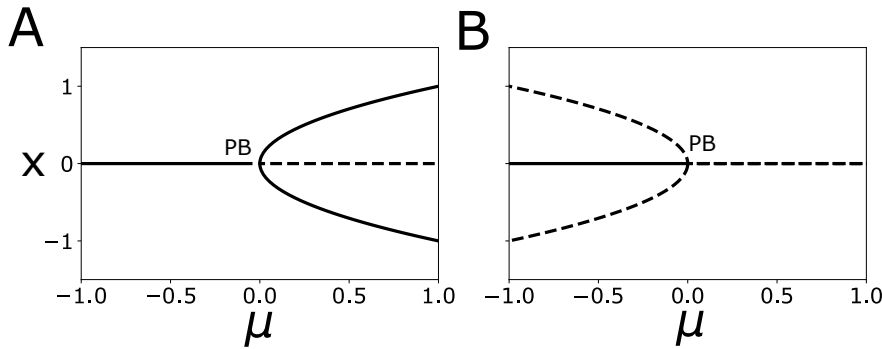
Figure 1.9 Two types of pitchfork bifurcations. A, Super-critical type corresponding to Eq. 1.10. B, Sub-critical type corresponding to Eq. 1.11. Solid/dashed lines: stable/unstable states. PB: pitchfork bifurcation.

A sub-critical pitchfork bifurcation has a normal form similar to Eq. 1.10, but with different sign for the cubic term.

$$\begin{aligned} \frac{dx}{dt} &= \mu x + x^3 \\ \frac{dy}{dt} &= -y \end{aligned}$$

(1.11)

There are three steady states, $ss_1 = (0,0)$, $ss_2 = (\sqrt{-\mu},0)$ and $ss_3 = (-\sqrt{-\mu},0)$. in contrast to the super-critical case the steady states exist together for $\mu < 0$. ss_2 and ss_3 are unstable which leaves only the trivial state ss_1 to be stable for $\mu < 0$ (Figure 1.9B).

This destabilizing effect from the sign of the cubic term can be reversed by introducing an additional fifth order term to the flow in x-direction.

$$\begin{aligned}
\frac{dx}{dt} &= \mu x + x^3 - x^5 \\
\frac{dy}{dt} &= y
\end{aligned}$$

(1.12)
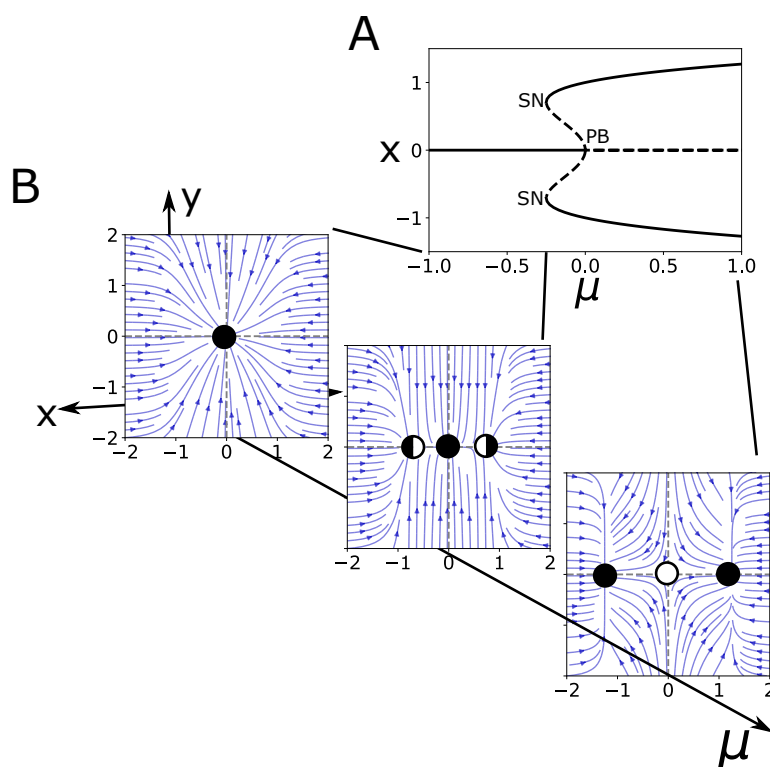
Figure 1.10 Sub-critical pitchfork bifurcation and corresponding state space transition. A, Bifurcation diagram showing sub-critical type corresponding to Eq. 1.12. Black solid/dashed line: stable/unstable state. PB: pitchfork bifurcation. SN: saddle node. B, State space transition across μ corresponding to (A) showing steady states and their flows around. Left: $\mu = -1$, middle: $\mu = -0.26$, right: $\mu = 1$. Filled/unfilled circle: stable/unstable steady state. Blue arrow lines: state space flows.

Bifurcation analysis shows that locally around $\mu = 0$, and for smaller x values, the sub-critical nature of the pitchfork bifurcation is retained (Figure 1.10). However, the unstable branches turn around and become stable at a smaller μ value ($\mu = \mu_s$). At this location the local bifurcation structure is equivalent to a saddle node bifurcation and it marks the stabilization of the unstable steady state branches that emerged from the sub-critical pitchfork

bifurcation. In the region $\mu_s \leq \mu \leq 0$, there are five steady states among which three are stable, making the region multi-stable. At $\mu = 0$, there is a "hard" loss of stability where once trivial state loses stability, there isn't any stable attractor region nearby. The system has to do transit to a far-off stable state (sometimes to infinity) similar to a large amplitude jump. Here in this case there are distant attractor state to which the system can settle to. In general, the super-critical bifurcations are associated with soft lose of stability and sub-critical with hard loss.

1.5 Dynamical modes of EGF sensing in epithelial cells

For any given biochemical network that can be written in the form of system of ODEs, bifurcation analysis help us to theoretically understand the parameter ranges in which possible dynamical regimes could occur. In [1, 21], this method was used to derive and understand different dynamical modes of operation associated with the EGFR-PTP network that was discussed before (Figure 1.5). The identified pairwise EGFR-PTP causal interactions unified by recycling, resulted in a receptor network that is distributed in space (Figure 1.11A). The modeling of the network using law of mass action enabled the use of bifurcation analysis to understand the mechanism behind EGF sensing.

Across an experimentally accessible intrinsic parameter (maximal activity of PTPRG relative to total concentration of EGFR ($PTPRG_{total}/EGFR_{total}$)), a bistable regime exist between two monostable regimes which are characterized by basal and high EGFR phosphorylation [21] (Figure 1.11B). This region is marked by the presence of two saddle-nodes ($SN_{1/2}$) and the coexistence of two stable states (solid lines) that represents high and low phosphorylation state together with an unstable state (dashed line) acting as a separatrix.

Different regimes of operation endows characteristic temporal features in EGFR phosphorylation (EGFRp) response. Parameter organization at monostable high region results in an irreversible pre-activation even in the absence of EGF (Figure 1.11C, top), while at the monostable low, an EGF pulse stimulation elicit a transient, reversible response that could not activate the system (bottom). For organization in the bistable region, EGFR can be in either in a basal or a high phosphorylation state in the absence of any stimulus. When starting from the basal EGFR phosphorylation state, the response shows abrupt activation upon supra-threshold EGF, however this activation sustained activation even after signal removal. This corresponds to an irreversibility (middle) in the response. These two properties associated with bistable mode of operation, ability to switch from basal to high in the presence of supra-threshold EGF and irreversibility, was described to explain experimentally observed lateral propagation of EGFR phosphorylation in epithelial cells [22, 21].

A

B   C
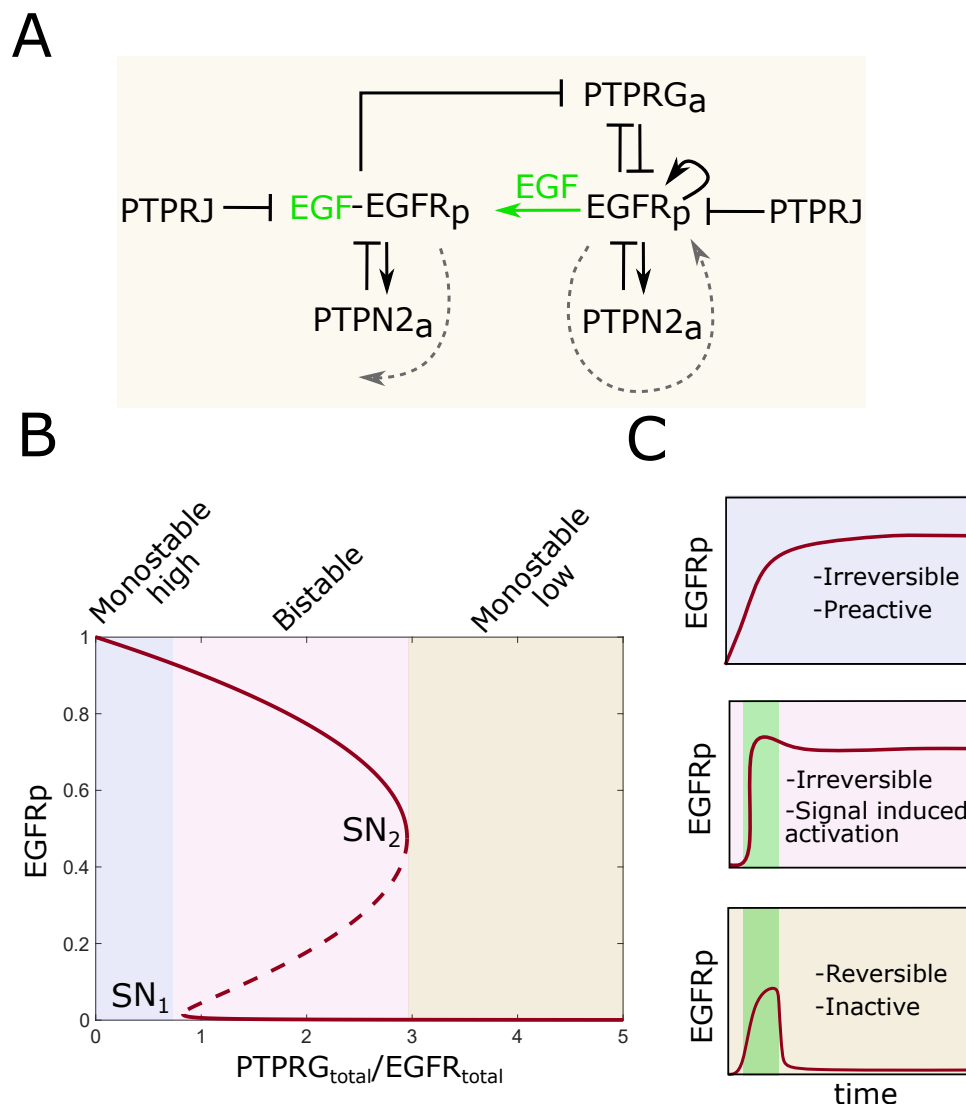
Figure 1.11 EGFR phosphorylation responses are determined by the dynamical modes of the spatially distributed EGFR-PTP network. A, Causality diagram (adapted from [1]) corresponding to spatially distributed EGFR-PTP network in Figure 1.5. Black lines: causal interactions. Green arrow: ligand binding. B, Bifurcation diagram for the network in (A) showing the dependence of ligandless EGFR phosphorylation dynamics (EGFRp) on $PTPRG_{total}/EGFR_{total}$ ratio [21]. $SN_{1/2}$: Saddle node bifurcations. Shading: dynamically different regions. C, Scheme of temporal profile of EGFRp with parameter organization corresponding to monostable high (top), bistable (middle) and monostable low (bottom). Green shaded region: presence of EGF. Background shading corresponds to (B).

However, the same irrirversible nature limits the system's responsiveness to temporal growth factor changes by switching it to a high EGFR phosphorylation state after the initial growth factor stimulus that leaves the system in a non-responsive state (Figure 1.12, left). On

the other hand, organization in the monostable low region leaves the system with a linear response that follows the growth factor profile (Figure 1.12, right), thus being unable to explain history-dependent response.
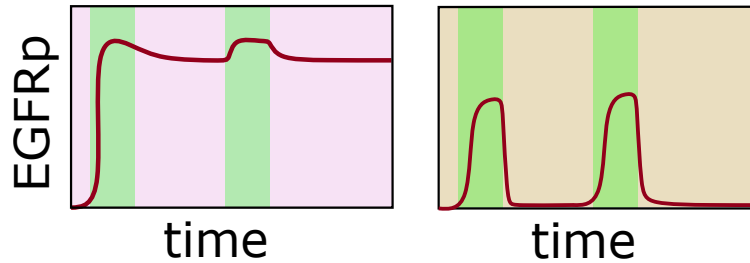
Figure 1.12 Schematic of EGFRp temporal evolution that shows bistable (left) and monostable (right) organizations are not suitable for time-varying growth factor sensing. Green shaded region: presence of EGF. Background shading corresponds to Figure 1.11B.

Both theory and experiments demonstrated that sensing growth factor signal changes cannot be realized when the system organization is in either the bistable or the monostable operation regime [1, 35, 26]. Namely, sensing time-varying EGF signals requires rapid amplification of EGFR phosphorylation together with the ability to reset to basal EGFR phosphorylation when growth factor levels decline [1, 26]. It has been proposed and demonstrated that these features arise for system's organization at the region of transition between the monostable low and bistable region.

1.5.1   Metastable dynamics at critical organization and sensing of changing environments

Among the different bifurcations that were discussed, saddle-node bifurcation is a basic mechanism for the creation and destruction of fixed points [33]. This process can give rise to regions in the state space where the flow is attracted although no steady states are present. This creates so-called "ghost" states [36, 37]. The "ghost" sucks trajectories, delaying the flow in phase space, rendering a metastable dynamics.

In Stanoev et al., from the inferences that EGFR phosphorylation was rapidly amplified as well as transiently maintained before resetting to basal levels in response to low-dose EGF pulses, they concluded that the EGFR-PTP system has dynamical organization close to the bistable region (Figure 1.11B, near SN_2). Theoretical analysis later showed that, for this critical organization (Figure 1.13A), due to the vicinity to a saddle node, the emergent metastable state gives rise to transient temporal memory in EGFR phosphorylation even after growth factor removal (Figure 1.13B, center). The corresponding reversible quasi-potential
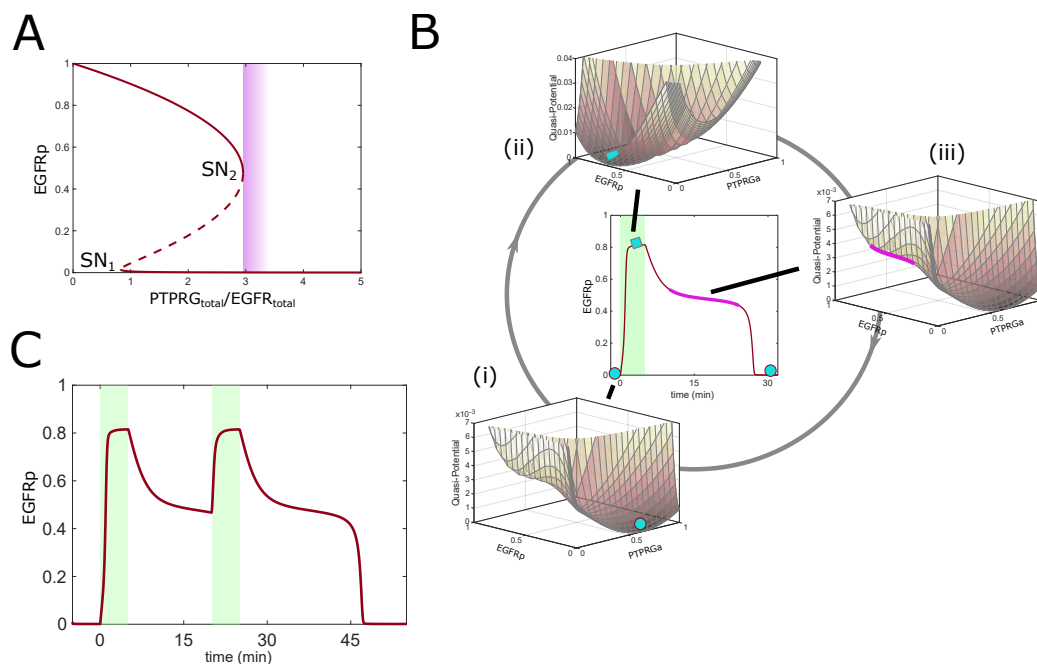
Figure 1.13 Critical organization and origin of dynamic transient memory. A, Bifurcation diagram in Figure 1.11B. Magenta shading: vicinity of the saddle-node (*SN*) bifurcation point. B, Center: EGFRp response to single growth factor pulse (green) for organization at criticality. $i \rightarrow ii \rightarrow iii \rightarrow i$: Corresponding quasi-potential landscapes showing (cyan circle) and active (cyan square) states. Magenta: metastable state trapping. C, EGFRp response to two subsequent growth factor pulses (green) corresponding to organization at criticality (compare with Figure 1.12, adapted from [35]).

landscape transitions (transition $i \rightarrow ii \rightarrow iii \rightarrow i$) shows that, when the trajectory transits back from the activated state (magenta square, *ii*) to the basal state (magenta circle, *i*), a shallow slope in the potential landscape shape (annotated with cyan, *iii*) gives rise to the metastable state that continues to capture the incoming trajectories. This dynamic transient memory of receptor phosphorylation that does not hinder further responsiveness of the system (Figure 1.13C), also enables the duration of EGFR phosphorylation to depend on previous stimulus history, effectively endowing signal-integration capabilities.

Thus, saddle-node (SN) "ghost" functions as a minimal dynamical mechanism that enables processing of time-varying growth factor signals [1, 35, 26].

1.6 Cellular response to spatially distributed signals

In tissues of organisms, cells secrete growth factor ligands into their environments that diffuse through the extracellular spaces, establishing spatial gradients which are ubiquitous for many

responses [38]. Such spatial gradients play a pivotal role during cellular chemotaxis that was observed across different cell types, as shown in Figure 1.1. Cellular polarization is the primary step in the response of cells to spatial signals and is the internal representation of the information in their surrounding.

Cell polarity establishment is the result of a concerted effort of multiple processes at different levels within the cell, at signaling level and the level of morphology. A polarized shape response, a direct observable, is actuated by anisotropic activity distribution of signaling molecules within the cell and this resulting shape can affect the signaling properties through mechanical feedback [39–41]. However, these processes are often studied independently from each other for simplification. Even though eukaryotic cells exhibit varying degrees of spatial gradient sensing capabilities through polarization response, they share common features. Following is a brief description of three main cell types that have been used to study polarity and chemotaxis to indicate those common features.

- Social amoeba *Dictyostelium discoideum* cells can sense cAMP gradients as shallow as 1 % across their length and can amplify their internal chemical polarization up to 7-fold [42]. These responses were measured either at the level of activated Ras accummulation [43] or downstream PIP3 localization [44]. The activity polarization is achieved quite rapidly (within $\approx$ 2min). In the absence of spatial gradient, these cells exhibited sensory adaptation [45] under uniform stimulation.

- In mammalian neutrophil cells, different types of G-protein coupled receptors at the membrane sense the chemoattractants [46] and during *in vivo* immune response chemoattractant such as N-formylated peptides emitted by dying cells or intravascular chemokines such as CXCL5 directs neutrophils to the site of inflammation [47, 48]. Different attempts to measure this *in vivo* gradients from the wounds by [49] and [50] have revealed that the extent of gradients that these cells sense across their length can be vanishingly small, depending on its position from the wound, showing that they exhibit high sensitivity towards shallow external gradients as well as features of memory in response. Similar to *Dictyostelium discoideum*, neutrophils can sense and rapidly polarize in gradients as shallow as 1 % [51] and can have strong internal amplifications up to 5-folds [52].

- Another type of mammalian cells which are involved in wound healing are fibroblasts. Platelet derived grwth factor (PDGF) produced by platelets and macrophages from the wound location, forms a gradient in the tissue and serves as a potent chemoattractant, thus accelerating the rate of fibroblast invasion [53]. In contrast to *Dictyostelium discoideum* and neutrophils, there was initial evidence suggesting that fibroblasts

cannot sense shallow gradients [54]. Robust PDGF sensing required steeper gradients and a much narrower range of absolute chemoattractant concentration. However, a recent theoretical study using a calibrated, mechanistic model have shown that the cells exhibit an internal amplification for PDGF gradients with 10 % relative steepness across their length [55].

There have been many theoretical modeling approaches to understand nonlinear responses during polarization. They were mainly focusing on the smaller molecular network with few components together with their diffusion to understand dynamical principles behind polarization [56]. Analysis of dynamical features associated with such spatially extended systems, modeled using reaction-diffusion equations, are performed differently than the stability analysis for ODEs (previously discussed in section 1.3.1). Here, in addition to time, the concentration/activity of components evolve in space as well. Classically, different approaches exist to understand instabilities and transitions in such spatially extended system.

1.7 Bifurcations and patterning in spatially extended systems

In a spatially extended biochemical network the diffusion of the components in their respective compartments plays a crucial role in shaping the global response. Since Turing's pioneering study on morphogenisis, reaction-diffusion models have occupied the center stage in theoretical studies of biological systems [57]. In this framework, the notion of steady states are substituted with spatially homogeneous and time invariant state of the system. Turing showed that in such a system the homogeneous steady state, under certain conditions, could lose its stability and give rise to spatially inhomogeneous pattern such as spots and stripes of animals [58]. When the components, he called morphogens, react and diffuse the instability arise when their diffusion constants have considerable disparity. This he termed diffusion driven instabilities (later called as Turing instability). In a given system, the existence of this instability can be checked using an extension of linear stability analysis. Analogous to LSA in ODEs, a perturbation, this time with spatial dependency, is introduced to check the stability of the homogeneous steady state.

At its simplest, a pair of partial differential equations (PDEs) for a pattern-forming RD system in one-dimensional space has the form,

$$\frac{\partial u}{\partial t} = f(u,v) + D_u \frac{\partial^2 u}{\partial x^2}$$

$$\frac{\partial v}{\partial t} = g(u,v) + D_v \frac{\partial^2 v}{\partial x^2}. \tag{1.13}$$

where f and g are nonlinear functions of u and v. D_u and D_v are the diffusion constants. The spatial dependency of perturbation around the homogeneous steady state (u_s, v_s) is assumed to be periodic across the domain with a specific wave number k.

$$\delta u(x,t) = u_s + e^{(kx+\lambda t)}$$

$$\delta v(x,t) = v_s + e^{(kx+\lambda t)} \tag{1.14}$$

Using this, the linearization of Eq. 1.13 yields a form equivalent to Ed. 1.4 but this time with Jacobian matrix,

$$J = \begin{pmatrix} \frac{\partial f}{\partial x} - k^2 D_u & \frac{\partial f}{\partial y} \\ \frac{\partial g}{\partial x} & \frac{\partial g}{\partial y} - k^2 D_v \end{pmatrix}_{(u_s,v_s)} \tag{1.15}$$

The eigenvalues of J is now not only a function of system parameters but also of the wave number (k) associated with the perturbation. From the characteristic equation corresponding to J, the largest eigenvalue ($\lambda_{max}(k)$) is estimated. The dispersion relationship between the $\lambda_{max}(k)$ and the wave number is then used to identify the perturbations modes which makes the homogeneous state are unstable, that means wave numbers for which $\lambda_{max} > 0$ (Figure 1.14, left). These unstable modes grow over time and eventually leads to stable spatial pattern formation (Figure 1.14, right).

The limitation of this method is that the mechanism/bifurcation that leads to instability cannot be identified. From our knowledge of bifurcations in ODEs, a steady state loosing stability means it could happen via multiple type of bifurcations and each of those bifurcations have unique features such as the "ghost" for *SN* bifurcation. In order to overcome this difficulty to find the type of bifurcation underlying an instability in a spatially extended system, [59] introduced a method called local perturbation analysis (LPA) where an approximate early evolution of an arbitrarily large perturbation of the homogeneous steady state is tracked. By doing so, the method allows for the conversion of PDEs to ODEs and the use of classic bifurcation analysis.
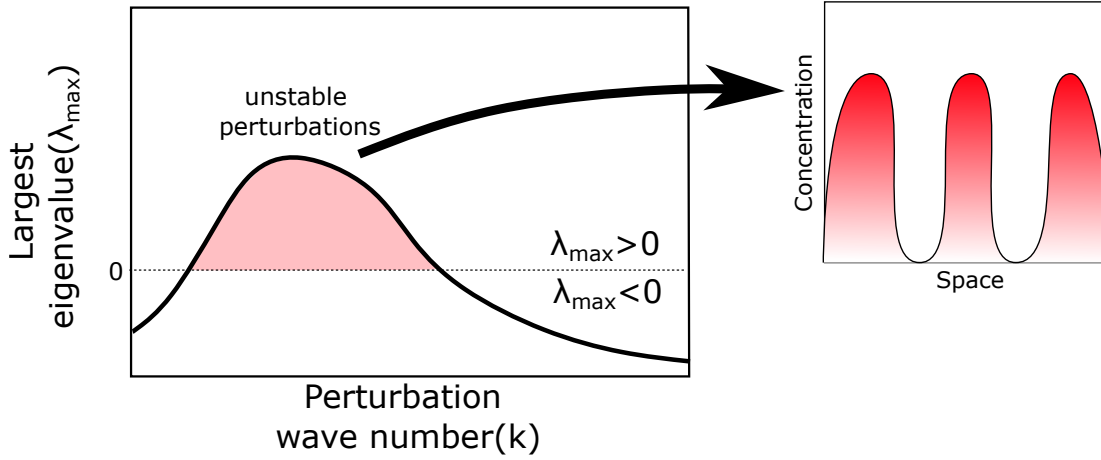
Figure 1.14 Linear stability analysis (LSA) showing origin of Turing instability in reaction-diffusion (RD) system. Left: Schematic of dispersion relation between maximal growth rate (λ_{max}) and wave number (k) of linear perturbation. Red shading: unstable perturbations/modes. Right: Resulting spatial pattern of concentration field.

For a PDE system as in Eq. 1.13 a central requirement for application of the LPA method is large size discrepancy between the diffusion constant values e.g. $D_u << D_v$. Under this assumption u is slowly diffusing and the height of the perturbation pulse on u can be represented by a single local variable, $u^l(t)$, that does not spatially spread. Due to the fast rate of diffusion, v can be represented by a uniform, global quantity, $v^g(t)$, on the entire domain. Since u does not spread and v is uniform on the domain, u can then be represented on the remainder of the domain by a global quantity, $u^g(t)$. The evolution of these quantities is described by,

$$\frac{du^g}{dt} = f(u^g, v^g)$$

$$\frac{dv^g}{dt} = g(u^g, v^g) \tag{1.16}$$

$$\frac{du^l}{dt} = f(u^l, v^g)$$

The ODEs corresponding to the global quantities (u^g and v^g) capture the evolution of the homogeneous state of the original PDE system (Eq. 1.13), while the local quantity (u^l) captures the perturbation part. When the homogeneous state is stable, then the perturbation decays and results in $u^l = u^g$ and if it is unstable the perturbation deviates away from the

global quantity and results in $u^l \neq u^g$. The stability of these possible steady states can be checked using either LSA outlined in section 1.3.1 or using bifurcation analysis softwares such as XPPAUT [60]. The LSA can only identify the Turing regime but the bifurcation analysis can reveal the underlying bifurcation/mechanism [61] that leads to the Turing instability. For an illustration, consider a two component substrate inhibition model [62] with,

$$
\begin{aligned}
F_u &= \quad a - u - \frac{\rho uv}{1 + u + Ku^2} \\
F_v &= \quad \alpha(b - v) - \frac{\rho uv}{1 + u + Ku^2}
\end{aligned}
\tag{1.17}
$$

The LSA analysis (Figure 1.15A, left) reveals that, for the parameter value range 103<a<116 (shaded region), $\lambda_{max} > 0$ and the homogeneous steady state is unstable. Therefore, this region has Turing instability and solving the PDE for the system Eq. 1.17 with arbitrarily small perturbation around the homogeneous steady state results in spatial patterns (Figure 1.15A, right). Outside this Turing regime, λ_{max} value indicate that any perturbation around the homogeneous steady state will decay over time and does not cause patterning (not shown). LPA analysis of the same system in Eq. 1.17 reveals that the mechanism underlying this instability is a pitchfork bifurcation (Figure 1.15B). The parameter range between the two *PB*s, where the homogeneous state is unstable (dashed line, $u^l = u^g$), coincide with the Turing regime that LSA identified. In this region, the red branches corresponds to $u^l \neq u^g$ which is a symmetry broken branch, resulting in spatial patterns similar to (Figure 1.15A, right).

In addition to this, the region before and after Turing regime shows coexistence of this symmetry broken, inhomogeneous branch and stable homogeneous state separated by an unstable inhomogeneous branch (separatrix). Existence of such a region suggest that the *PB* is of sub-critical type and this region also posses pattern forming capabilities (Figure 1.15B, right). However, it is not a Turing pattern because the homogeneous state is stable in this regime and amplitude of the perturbation around homogeneous steady state should be large to elicit pattern due to the existence of the separatrix. This additional non-linear patterning regimes were not detected with LSA [61, 59, 63].

However, the application of LPA is limited to networks that have large diffusion discrepancy. For those networks that do not satisfy this condition, it is possible to identify the type of bifurcation via an extension of LSA called weakly nonlinear analysis (WNA) [64, 65]. The LSA can be used to identify the existence of instability that could lead to pattern formation
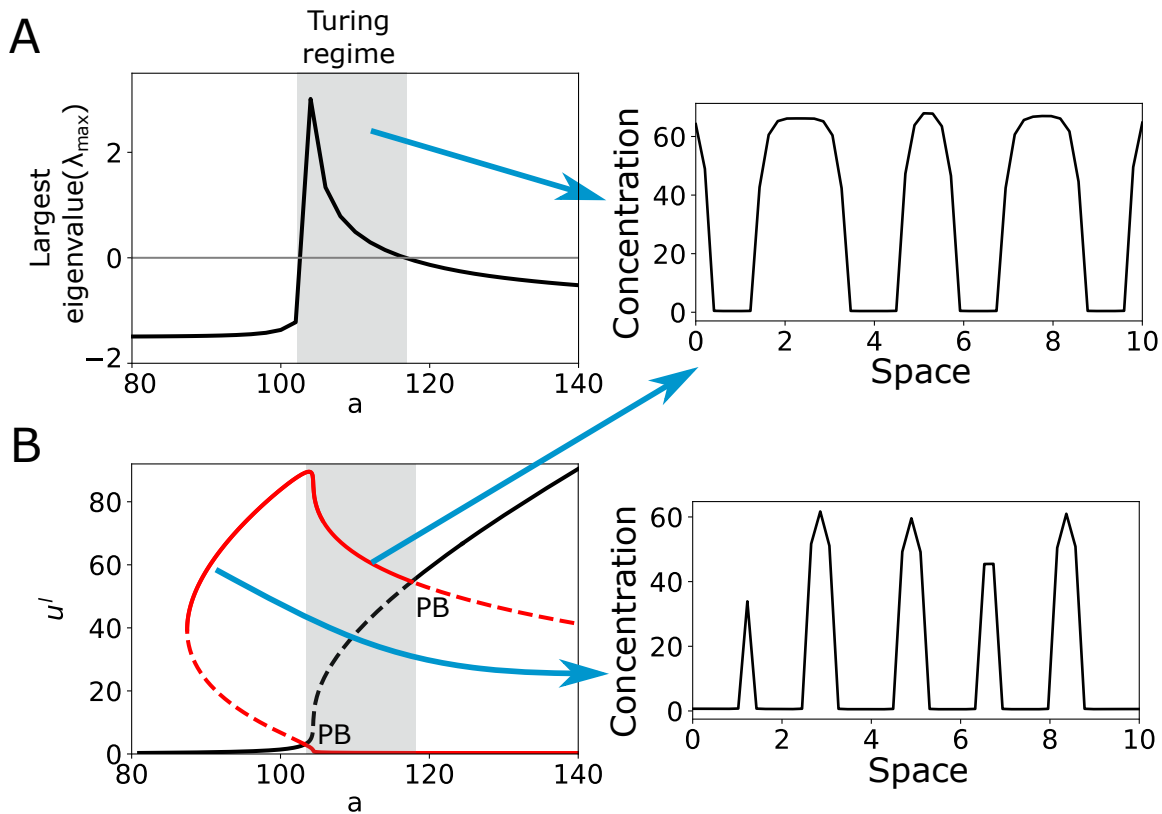
Figure 1.15 Comparison of linear stability and local perturbation analysis for the substrate inhibition model (Eq. 1.17) with Turing instability. A, Results from linear stability analysis. Left: Largest eigenvalue as a function of system parameter a. Right: Turing pattern obtained by solving corresponding partial differential equation for a=110. B, Bifurcation diagram from local perturbation analysis. Left: Bifurcation analysis showing u^l as a function of a. Red branch: $u^l \neq u^g$, black branch: $u^l = u^g$. PB: pitchfork bifurcation. Solid/dashed lines: Stable/unstable branches. Right: Spatial pattern obtained by solving corresponding partial differential equation for a=95. Shaded region: Turing regime.

and then the WNA can be used to identify the type of bifurcation that leads to instability by finding an approximate expression of the equation governing the early time evolution of perturbation amplitude [66]. This amplitude equation can be then compared with the normal form equation discussed in section 1.4 to specify what type of bifurcation underlies the instability.

1.8   Different mathematical models for cellular polarization

Majority of the mathematical modeling approaches for polarization in biochemical networks are describing feedbacks in the form of activation, inactivation, depletion of substrate,

diffusion enabled long range interactions etc. to account for polarization features that were observed in many cell types.

Most of the modeling approaches have focused to identify smaller network motifs consisting of most relevant components embedded within. This reduction in the number of components reduced the complexity in analysis and identification of principles that govern polarization events that actually represent the response of the molecular network as a whole [67, 68].

1.8.1 Local excitation global inhibition model

Directional sensing at the level of signalling response through local excitation and global inhibition was initially proposed in [69] to describe the observations in *Dictyostelium discoideum*. Later on, observations about adaptation to uniform stimulation and amplification of shallow gradients led to the proposal of the basic network motif of LEGI (Figure 1.16A). It consists of a signal (s), an activator (w) and an inhibitor (v). A response component (u) depends on the balance of v and w. This incoherent feedforward loop (IFFL)network was sufficient to account for the transient response and adaptation to uniform stimulus [70].

Later a variant of this LEGI model, referred as balanced inactivation model [71] was proposed to explain the switch-like behavior observed in the spatial distribution of PH-domains, that the LEGI didn't account for. Here, the need for an additional feedback loop was substituted with the inhibitor having two forms - fast diffusing cytosolic (v_c) and slow diffusing membrane (v_m) bound forms. This model also ruled out the need for an intermediate activator w (Figure 1.16B).

Like the balanced inactivation model, derivatives of LEGI model were proposed in order to account for different inherent features that were experimentally observed such as the propagating waves within the actin cytoskeleton. LEGI-biased excitable network (LEGI-BEN) was introduced and is a combination of LEGI module and a classical two component excitable network [72] (Figure 1.16C). This extended model accounted for spontaneous cytoskeletal activity, signaling responses to temporal stimuli, and spatial gradient sensing.

Biochemical description of LEGI models were focused around G-protein coupled receptors (GPCRs) and their downstream effectors. The biochemical steps between ligand binding and the experimental readout variables are not completely known, and, hence, it is difficult to identify the model components in a definitive way [71]. Experimental evidences about GPCR mediated activation of PI3K or Ras made them a proper candidate for the activator, w. However, the gradient sensing in classical LEGI model or the balanced inactivation models depend on the activity and diffusivity of the inhibitor, that enables termination and adaption of the response. It has been however reported that biochemical identification of these inhibitors
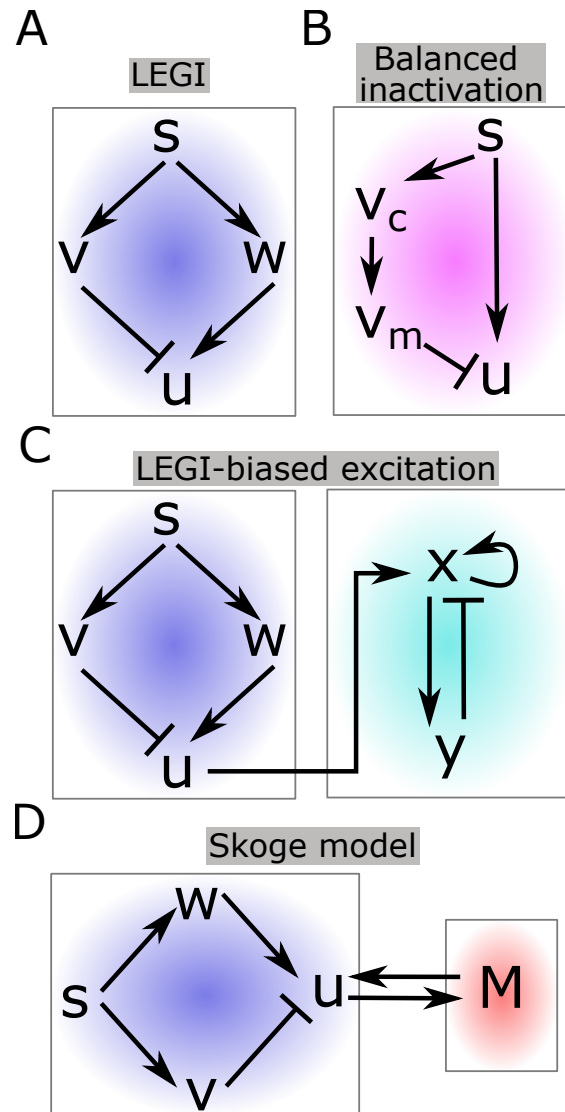
Figure 1.16 Local excitation and global inhibition (LEGI) and its derivative models. *s*: stimulus, *v*: inhibitor in LEGI (*v_c*: cytosolic, *v_m*: membrane bound), *w*: activator in LEGI, *u*: response element, *x*: activator in excitable module, *y*: inhibitor in excitable module, *M*: output of memory module. Lines: causal links.

is difficult, despite extensive experimental work [71]. PTEN, a phosphatase and an antagonist to PI3K in PIP3 production was a suspected candidate, but recent experiments with PI3K knockout cells showed that they were still able to polarize, casting shadow over this combination as *w* and *v* in LEGI [73]. Recently, experimental investigation in *Dictyostelium discoideum* revealed that adaptation in Ras activity is achieved through the proportional activation of upstream components, suggesting an incoherent feed forward network which

was consistent with LEGI model for gradient sensing [74]. They suggested Ras guanosine triphosphatase–activating protein acting as a possible global inhibitor. However to this date an actual description about a the inhibitor is lacking.

One of the recent LEGI model derivative model is in [43] where they observed a cellular memory in direction migration after the gradient removal in *Dictyostelium discoideum*. In order to account for this observed memory, LEGI model was coupled with a bistable memory module (whose output is *M*) and it was activated in a threshold dependent manner (Figure 1.16D). However the biochemical identity of *M* and proposed positive feedback were not substantiated.

Additionally, the LEGI-models cannot account for spontaneous polarization, a basic feature of many cell types including netrophils and fibroblasts [75, 76]. This is a consequence of the the adaptive nature of the network motif.

1.8.2   Turing models

Turing models are based on the Turing instability (or Turing bifurcation) that is described in section 1.7. It was Gieger and Meinhardt who showed that such pattern forming mechanisms can be used to model and understand chemotactic response in cells [77]. The experimentally observed spontaneous polarization in cells led them to propose Turing instability as an underlying mechanism. The assumed cell-internal pattern forming reaction network consists of a self-enhancing activator (*u*) and a long-ranging inhibitor (*v*) (Figure 1.17A). Either an internal noise or a slightly asymmetric external signal could lead to symmetry breaking and polarization. A polarized activity profile corresponds to a single, global peak in the pattern. The activator-inhibitor system, however created multi peak solutions. To explain the simultaneous extensions of new and the retraction of existing peak, a second antagonist of the activator is assumed in the model. In contrast with the first inhibitor, this one acts locally and has a longer time constant than the activator [77]. Turing-based models are not always activator-inhibitor type. Narang [78] derived a minimal three-component model consisting, this time, of two mutually inhibiting local activators (u_1 and u_2) that promote the synthesis of a common diffusible inhibitor (*v*) that, in turn, inhibits both the activators (Figure 1.17B). Unlike activator-inhibitor model, the mutual inhibition between the two activators substitutes the autocatalysis required for amplification. Shortly after Narang's model, a substrate-depletion model was proposed by Otsuji [79] (Figure 1.17C). The network used was similar to the activator-inhibitor model but the inhibitor replaced with a substrate. This bought mass conservation and autocatalytic activation which is damped by the substrate consumption, hence substrate-depletion. Another notable Turing model is from [80] where

they proposed that during the early phase of yeast budding, the biochemical mechanism that leads to Rho GTPase Cdc42 polarization is Turing instability.
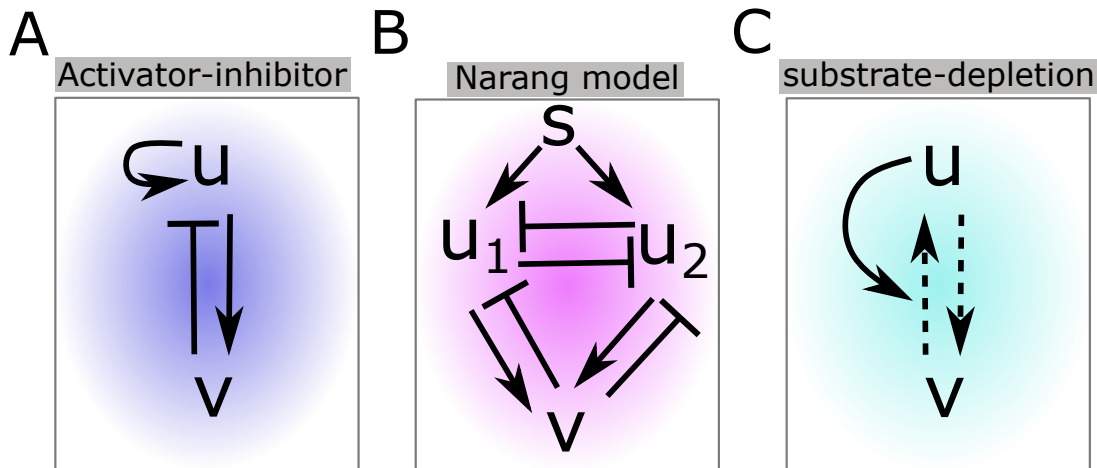
Figure 1.17 Different types of Turing models and corresponding protein interaction motifs. s: signal, u: activator (also u_1 and u_2), v: inhibitor. Solid/dashed lines: causal links/conversion.

Polarization features accounted by Turing models were based the experimental observations in *Dictyostelium discoideum*, neutrophil cells (except Goryachev model with yeast cell) and the molecular description has changed since the first activator-inhibitor model. Geiger and Meinhardt suggested the possibility of involvement of G proteins and Ca^{2+} in intracellular pattern formation [77]. In their three component network, Ca^{2+} or the channel receptors such as the inositol 1,4,5-trisphosphate receptor (InsP3R) could be the activator u. Main reason was the evidences about calcium-induced-calcium release based on voltage-gated channel opening as a autocatalytic/self-enhancement mechanism [81]. This, in turn, can lead to an electrophoretic movement of the charged channel molecules, increasing in this way the local accumulation of channels. Since any local accumulation of channel molecules at one side leads to their depletion on the remaining surface, a long ranging antagonistic reaction becomes possible. Additionally, the type I InsP3R has the property to open at low and to close at high Ca^{2+} concentrations [82] which could play the role of local inhibitor. Identity of biochemical species was entirely different in Narang model. The chemoattractant binds to G-protein-coupled receptors and simultaneously activate the actin polymers (u_1) through PIP3 at the protrusion sites and myosin (u_2) through RhoA at the contracting site. There is no biochemical counterpart for the inhibitor (v) but the global inhibition is achieved through actin-polymer mediated inhibition of Rho and actin-myosin mediated inhibition of PIP3. Turing models that came after Narang model described the dynamics of Rho GTPases.The

Rho GTPase family, mainly Cdc42, Rac, and Rho, is conserved from amoeba to mammalian cells. They play central role in cell motility, yeast budding, cytokinesis, and wound healing etc. Each Rho GTPase cycles between the plasma membrane bound active form and cytosolic inactive form with conversions facilitated by GAPs, GEFs, and GDIs [83]. Thus they became the ideal candidate for Otsuji's two component conceptual model. Goryachev model for yeast polarity has this conceptual model with Cdc42 cycle but it included other proteins and protein complexes that are involved in the activation and inactivation processes.

Turing models were successful in explaining spontaneous polarization and high degree of internal amplification. Due to the ability to spontaneously polarize in the presence of small amplitude noise in the surrounding, however Turing models fail to account the existence of a unpolarized state observed in neutrophil cells. The model also result in a self-locking or "freezing" of the polarized response. Thus, if a sharp intracellular gradient results as a response to an external chemoattractant gradient, any change in the direction of the external gradient won't elicit any new leading edge. Such a permanent polarized response was not observed in any of the cell types described [84].

1.8.3   Wave pinning models

Wave pinning models were based on Rho GTPases that have an inherent polarization ability (Figure 1.18A). This wave pinning dynamics refers to propagation of wavefront in reaction diffusion systems with bistability [85], that eventually undergoes a pinning into a stable polar distribution due to overall mass conservation [86, 87]. Even though the molecular architecture of the wave pinning model is similar to the conceptual mass conserved Turing model from Otsuji, they exhibit qualitatively different responses. Existence of an un-polarized state in wave pinning model even in the presence of small amplitude stimuli is one of them. This is because of the existence of a threshold for activation. Once the stimulus crosses the threshold, a stable amplified polarized peak appears and it travels to the nearby area with a characteristic velocity that depends on the amount of cytosolic component (v) and halts due to the substrate depletion. Unlike Turing models, polarization here is not based on diffusion driven instability but is wave based [86]. The position of this pinned wave peak can be shifted depending on the peak of a new and stronger gradient.

Similar to the other polarity model based on bistability, wave pinning model exhibits a saturation in polarized response upon stimulation. This magnitude of the polarized front becomes independent of the stimulus amplitude. Like Turing models, wave pinning also suffers the "freezing" of the polarized response. The only difference here is that a stimulus of higher amplitude could "unfreeze" and re-orient the system. However, in experiments
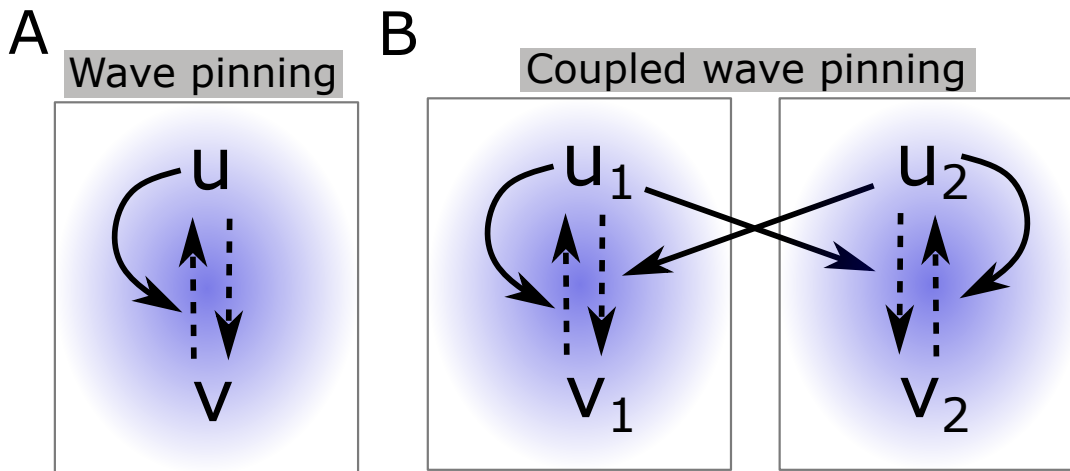
Figure 1.18 Different types of wave pinning models and corresponding protein interaction motifs. *u*: activator (also u_1 and u_2), *v*: inhibitor (also v_1 and v_2). Solid/dashed lines: causal links/conversion.

neutrophils and *Dictyostelium discoideum*, stimuli of similar amplitudes could elicit this re-orientations.

Wave pinning models were extended to include cross talks between different Rho GTPases (Figure 1.18B). This coupled model include mutual antogonism between two different Rho GTPases with their own auto activation and mass conservation [88]. As Rho GTPases are well-known cytoskeletal regulators whose activity levels have been causally linked to cell shape [89], this extended model was able to capture several phenotypical features associated with migrating cells. Depending on the relative levels of the two Rho GTPases this extended model yielded several types of polarized and un-polarized shapes while original wave pinning model could only account for a restricted set of cell morphologies.

1.9   Limitations in existing cell polarity models

To operate in non-stationary environments, cells must have optimal features in both polarization as well as in processing dynamic information in real time. These essential features are shared by many cell types.

In terms of polarization features,

- The cellular sensing networks must quickly and robustly polarize the signaling at the plasma membrane in the direction of the gradient, enable sensing of steep and shallow gradients. Similar sensing, while accounting for threshold activation to filter out noise, and **internal amplification** capabilities are exhibited by *Dictyostelium*

discoideum, neutrophil and fibroblast where the difference between front and back signal concentration as small as 1%–2% were amplified to have asymmetric response at macroscopic level [42, 51].

- Cells should exhibit **adaptation** in a uniform stimulus, that is, the cells generate transient response to a temporal change in a uniform stimulus [45].

- Cells **spontaneously polarize** and establish an axis of asymmetry in the absence of stimuli [75, 76, 90].

In terms of information processing features,

- The sensing networks must enable responsiveness to consecutive signals, quickly adapt and **re-polarize** to subsequent deferentially localized signals. Chemotactic cells exhibit such reorientation capabilities when the stimulus gradient is reversed [71].

- In response to multiple stimuli, such as two sources of stimuli with varying strengths, cells should rapidly **resolve** the conflict with a unique axis of polarity [5].

- When the triggering spatial stimulus is removed, the cells should be able to maintain the polarization response transiently (**transient memory**) in order to integrate the dynamic signals and thereby generate history-dependent responses [43].

Various polarization models and their derivatives that we discussed so far could only account for a subset of these cellular response features. A summary of strengths and weakness of those models are summarized in Table 1.1.

Table 1.1 Strengths and weaknesses of different cell polarity models.

Features	LEGI type	Turing type	Wave pinning type
Internal amplification	No	Yes	Yes
Adaptation to uniform stimulus	Yes	No	No
Spontaneous polarization	No	Yes	Yes
Reversal of polarization	Yes	No	No
Resolving multiple stimuli	Yes	Yes	Yes
Transient memory	No	No	No
Permanent memory	No	Yes	Yes

These inferences show that none of the modeling approaches so far captured polarization features that were conserved across different cell types. Further investigation into the dynamical features of each model is needed to help us understand the reasons for their weaknesses.

1.10   Objectives

The main objective of this thesis is to identify the dynamical mechanism that enables single cells to operate in non-stationary environments. The mechanism should account for optimal features in cell surface receptor polarization response such as the ability to robustly polarize in a threshold dependent manner in the direction of spatial cues, as well as optimal features in information processing such as the ability to maintain a memory of the location of recent signals while still being adaptive towards novel signals. We set out to investigate whether the existing paradigm of attractor-based computation of biochemical networks is sufficient to fulfill these opposed features. If not, what is the characteristics of symmetry-breaking transitions and parametric organization of these networks that allow for real-time information processing? We also addressed the question whether an analytical description of the necessary conditions for the existence of such a mechanism can be derived. Finally, we probe this hypothesized mechanism experimentally, to outline the functioning of the system.

Chapter 2

Materials and Methods

2.1 Cell Culture

MCF10A cells (sex: female, ATCC-CRL 10317) were grown at 37 °C and 5 % CO_2 in Mammary Epithelial Cell Growth Basal medium (MEBM from Lonza Pharma & Biotech), supplemented with 5 % Horse Serum (HS) (Invitrogen), $20\,\mathrm{ng\,mL}^{-1}$ EGF (Sigma-Aldrich), $0.5\,\mathrm{mg\,mL}^{-1}$ hydrocortisone (Sigma-Aldrich), $100\,\mathrm{ng\,mL}^{-1}$ cholera toxin (Sigma-Aldrich), $10\,\mathrm{\mu g\,mL}^{-1}$ insulin (Sigma-Aldrich), $100\,\mathrm{\mu g\,mL}^{-1}$ penicillin and $100\,\mathrm{\mu g\,mL}^{-1}$ streptomycin. Serum starvation was performed by culturing the cells in the DMEM supplemented with 0.5 % HS, $0.5\,\mathrm{mg\,mL}^{-1}$ hydrocortisone (Sigma-Aldrich), $100\,\mathrm{ng\,mL}^{-1}$, cholera toxin (Sigma-Aldrich) $100\,\mathrm{\mu g\,mL}^{-1}$ penicillin and $100\,\mathrm{\mu g\,mL}^{-1}$ streptomycin. MCF10A cells were authenticated by Short Tandem Repeat (STR) analysis and did not contain DNA sequences from mouse, rat and hamster (Leibniz-Institut DSMZ). Cells were regularly tested for mycoplasma contamination using MycoAlert Mycoplasma detection kit (Lonza).

2.2 Reagents

Imaging media: DMEM without Phenol Red was mixed with 25 mM HEPES. For nuclear staining, 20 mM Hoechst 33342 (Thermo Fisher Scientific) was mixed with DPBS and diluted to $2\,\mathrm{\mu M}$ working concentration.

2.3 Confocal and wide-field microscopy

Confocal images were recorded using a Leica TCS SP8i confocal microscope (Leica Microsystems) with an environment-controlled chamber (Life Imaging Services) maintained at

37°C and HC PL APO 63x/1.2 N.A / motCORR CS2 water objective (Leica Microsystems) or a HC PL FLUOTAR 10x/0.3 N.A. dry objective (Leica Microsystems). Hoechst 33342 (Thermo Fisher Scientific) were excited with a 405 nm diode laser. The detection of fluorescence emission was restricted with an Acousto-Optical Beam Splitter (AOBS):Hoechst 33342 (425 nm-500 nm). Transmission images were recorded at a 150-200% gain. To suppress laser reflection, Notch filter 488/561/633 was used whenever applicable. When using the dry objective for migration experiments, the pinhole was set to 3.14 airy units and 12-bit images of 512x512 pixels were acquired in frame sequential mode with 1x frame averaging.

Wide field images were acquired using an Olympus IX81 inverted microscope (Olympus Life Science) equipped with a MT20 illumination system and a temperature controlled CO_2 incubation chamber at 37°C and 5% CO_2. Fluorescence and transmission images were collected via a 10x/0.16 NA air objective and an Orca CCD camera (Hamamatsu Photonics). Hoechst 33342 fluorescence emission was detected between 420 nm-460 nm via DAPI filter. The xCellence (Olympus) software was used.

2.4 Gradient establishment for migration experiments

The CellAsic Onix Microfluidic Platform (EMD Millipore) was used for gradient cell migration experiments.

For migration experiments under subsequent gradient stimuli / gradient quantification, the following steps were performed:

- Pre-stimulus: Imaging media was flowed from well groups 3 and 4 (CellAsic Onix Manual - www.merckmillipore.com/) at low pressure (2.5 kPa) for 5 min.

- First gradient establishment: After closing well group 3, pre-loaded EGF^{647} (30 ng mL^{-1}) was flowed through well group 2 and imaging media from well group 4 at high pressure (15 kPa) for 15 min.

- First gradient maintenance: The pressure was reduced to 10 kPa for 225 min.

- Washout: After closing well groups 2 and 4, imaging media was flowed from well groups 3 and 5 at high pressure (15 kPa) for 15 min and maintained at low pressure (7 kPa) for 15 min.

- Second gradient establishment: After closing well group 3, EGF^{647}(30 ng mL^{-1}) / 2.5 μM Fluorescein was flowed from well group 2 and imaging media from well group 4 at high pressure (15 kPa) for 15 min.

- The second gradient thus formed was maintained by reducing the pressure to 10 kPa for 45 min.

- Washout: imaging media was flowed from well groups 3 and 4 at high pressure (15 kPa) for 15 min and maintained at low pressure (7 kPa) for 15 min.

- Third gradient establishment: After closing well group 4, EGF^{647} (30 ng mL^{-1}) / 2.5 µM Fluorescein was flowed from well group 5 and imaging media from well group 3 at high pressure (15 kPa) for 15 min.

- The third reversed gradient was maintained by reducing the pressure to 10 kPa for 225 min.

- Washout: imaging media was flowed from well groups 3 and 4 at high pressure (15 kPa) for 15 min and maintained at low pressure (7 kPa) for 285 min.

2.5 Imaging single cell migration and tracking

For migration experiments under EGF^{647} stimulation, confocal laser scanning microscopy of MCF10A cells was done on a Leica TCS SP8i or Olympus IX81 for multiple positions at 2 min time interval, using the 10x dry objective for 14 hours. Single cell migration trajectories were extracted using Trackmate[91] in Fiji [92] using Hoechst 33342 / transmission channel. From the positional information (x and y coordinates) of individual cell tracks, $\cos\theta$ value was extracted using custom made Python code (Python software foundation, versions 3.7.3, https://www.python.org/).

Chapter 3

Results

3.1 SubPB mechanism underlies sensing of changing environment

Symmetry breaking in a protein interaction network is an event in which a spatially uniform activity state of the components becomes unstable and an inhomogeneous activity distribution arises. Generally, a pitchfork bifurcation (*PB*) characterizes a transition from a homogeneous to an inhomogeneous steady state. In relation to protein activity polarization in cells, the homogeneous state represents an un-polarized state, while the inhomogeneous state represents a polarized state. A robust polarized response alone cannot facilitate an optimal response to a changing environment. That requires a mechanism that enables plasticity in the response. Our hypothesis is that this plasticity can be achieved if the protein networks operate away from steady states. In our previous work, we identified that when a saddle-node bifurcation (*SN*) and thereby a steady-state is lost in a dynamical transition, i.e., upon signal removal, a remnant or a dynamical "ghost" of the stable attractor serves as a mechanism for sensing time-varying growth factors in biochemical receptor networks [35]. We thus hypothesized that *PB* that enables robust polarization should be sub-critical and the system organization in the vicinity of *SN* of *PB*.

To provide quantitative description of sub-critical pitchfork bifurcation in a protein network, local perturbation analysis (LPA detailed in section 1.7) can be applied [59]. However, this analysis is mainly restricted to networks whose components have large discrepancy in their diffusion constants. In a general case, this diffusion discrepancy cannot be guaranteed, for instance if all components are bound within a single cellular

compartment. Moreover, pattern generating mechanisms need not rely on diffusion-driven instabilities. Therefore, it is necessary to identify an analytical procedure by which a sub-critical pitchfork transition can be identified in a general reaction-diffusion model.

3.1.1   Analytical description of sub-critical pitchfork bifurcation in spatially extended systems

Let us assume a generalized form of a RD model of M ($\mathbf{U} \in \mathbf{R}^M$) components in N ($\mathbf{x} \in \mathbf{R}^N$) dimensional space,

$$\frac{\partial \mathbf{U}(\mathbf{x},t)}{\partial t} = \mathbf{F}(\mathbf{U}(\mathbf{x},t)) + \mathbf{D} \cdot \nabla^2 \mathbf{U}(\mathbf{x},t) \tag{3.1}$$

where $\mathbf{F} \in \mathbf{R}^M$ is the reaction term, $\mathbf{D}$ is a $M \times M$ diagonal matrix of diffusion constants $D_j, j = 1,...,M$, and ∇^2 is the Laplacian operator. The conditions for a pitchfork bifurcation (*PB*)-induced transition in a generic RD model therefore must be formally defined.

Let $\mathbf{U_s} = (u_{is})$ for $i = 1,..,M$, be the stable homogeneous symmetric steady state of the RD system. Consider a linear perturbation of the form,

$$\mathbf{U}(\mathbf{x},t) = \mathbf{U_s} + \delta \mathbf{U}(\mathbf{x})e^{(\lambda t)}, \quad \delta \mathbf{U}(\mathbf{x}) \in \mathbf{R}^M \tag{3.2}$$

where $\delta \mathbf{U}(\mathbf{x})$ is the spatial and $e^{(\lambda t)}$ is the temporal part of the perturbation.

Substituting Eq.(3.2) in Eq.(3.1) yields a linearized eigenvalue equation whose solution can be determined by solving the characteristic equation, $F_\lambda = det(\lambda I_{M \times M} - J_{M \times M}) = 0$. J is the Jacobian matrix of the system defined by $J_{ij} = \frac{\partial \mathbf{F}_i(\mathbf{U}(x,t))}{\partial U_j}, i = 1,....,M, j = 1,.....,M$ is evaluated at the homogeneous symmetric steady state.

The system exhibits a *PB* if, an odd eigenfunction $\delta \mathbf{U}(\mathbf{x})$ such that $\delta \mathbf{U}(-\mathbf{x}) = -\delta \mathbf{U}(\mathbf{x})$, taken in the limit $\lambda \to 0$, fulfills the following condition [93]:

$$\lim_{\lambda \to 0} F_\lambda = det(J) = 0. \tag{3.3}$$

When these conditions are satisfied, the symmetric, homogeneous steady state of the system undergoes a pitchfork bifurcation and an inhomogeneous steady state (IHSS) with two branches of asymmetric steady states emerges. In terms of polarization, these branches correspond to front-back-polarized states, where the orientation depends on the direction of the external signal.

To identify whether the *PB* is of sub-critical type, and thereby identify the presence of a SN_{PB}, a weakly nonlinear analysis of Eq.(3.1) must be performed to obtain a description of the amplitude dynamics of the inhomogeneous state. This can be achieved using an approximate analytical description of the perturbation dynamics based on the Galerkin method [65, 94, 64]. For simplicity, we outline the steps for a one-dimensional system ($N = 1$). As we are interested in the description of a structure of finite spatial size (i.e. finite wavelength k), the final solution of the PDE is expanded around the fastest growing mode, k_m into a superposition of spatially periodic waves. That means that $u(x,t) \in \mathbf{U}$ can be written as the following:

$$u(x,t) \approx \sum_{n=-\infty}^{+\infty} \left(u_n(t) e^{nik_m x} + u_n^*(t) e^{-nik_m x} \right) \tag{3.4}$$

where $u_n(t)$ is the complex amplitude of the nth harmonics. Let the amplitude corresponding to the leading harmonics ($n = 1$) is $\phi(t)$. After assuming that the amplitude of each harmonic can be written as a power series of $\phi(t)$, substituting Eq.(3.4) into Eq.(3.1) allows to write an equation that describes the evolution of $\phi(t)$. In the case when the resulting equation is of Stuart-Landau type:

$$\frac{d\phi}{dt} = c_1 \phi + c_2 \phi^3 - c_3 \phi^5 \tag{3.5}$$

with $c_1, c_2, c_3 > 0$, this corresponds to the normal form of a sub-critical pitchfork bifurcation [33]. With the condition given by Eq.(3.3), the existence of a sub-critical pitchfork (PB) for the full system (Eq.(3.1)) is guaranteed. A numerical or analytical analysis of Eq.(3.5) enables the identification of the position of the SN_{PB}.

3.1.2   Sub-critical pitchfork bifurcation and different regimes of parameter organization
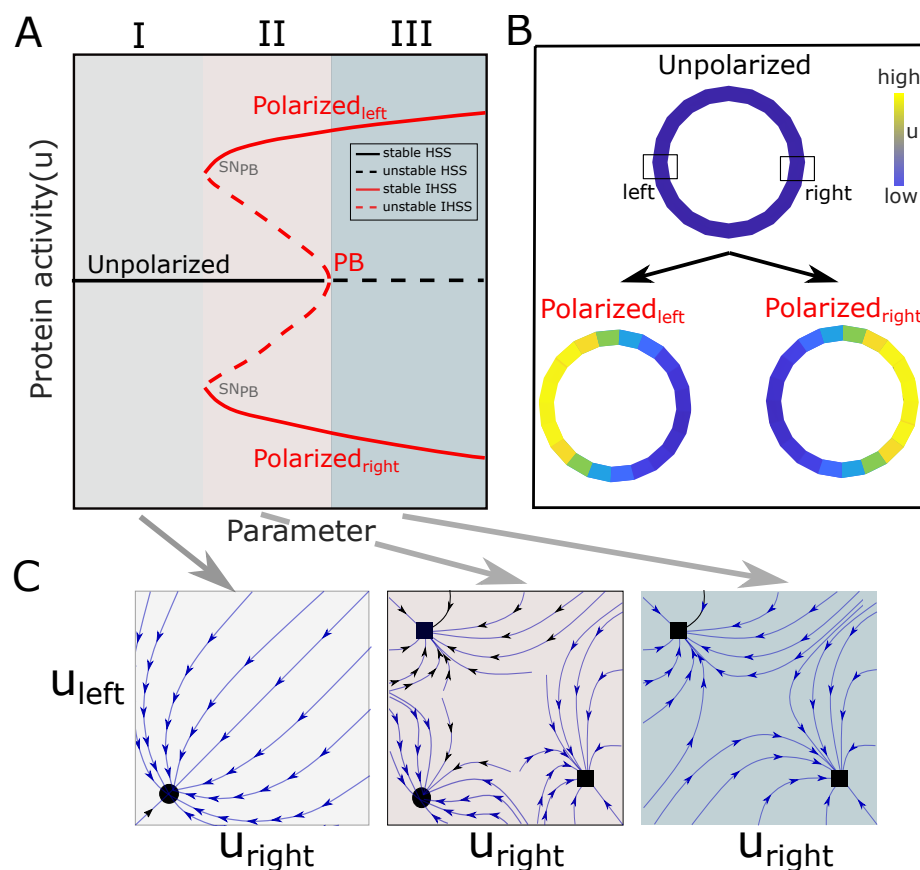
Figure 3.1 Schematic representation of sub-critical pitchfork bifurcation. A, Bifurcation diagram in the absence of external signals depicting protein activity steady states with respect to system parameter. Stable/unstable steady states (solid/dashed lines): unpolarized (homogeneous, black) and polarized (inhomogeneous, red) protein activity. SN_{PB}: saddle-node bifurcation through which pitchfork (*PB*) is stabilized. Shading: dynamically distinct regions. B, Schematic of an unpolarized cell (top) resulting in a left/right-polarized cell with *u* activity colour coded membrane. C. Schematic of protein activity state space ($u_{left} - u_{right}$) corresponding to three regions in A. Circle: homogeneous attractor; square: inhomogeneous attractor; blue lines with arrows : state space flows showing basin of attractors. Background colour: same as in (A).

The schematic of sub-critical pitchfork bifurcation, in the absence of an external signal, shows that the system exhibits qualitatively different dynamics for different parameter values. At lower values of the parameter, Region I, the system exhibits monostable behavior (Figure 3.1A, black line). In the context of a cell, this monostable state

manifests as a uniform protein activity across the cell membrane (Figure 3.1B, top) and renders an un-polarized state. Thus, the diametrically opposite sides of the cell populate the same state ($u_{left} = u_{right}$) and its projection falls on the main diagonal in the u_{left} - u_{right} state space (Figure 3.1C, left, black circle). However, at a critical parameter value, this homogeneous steady state (HSS) loses stability via a symmetry breaking pitchfork bifurcation (*PB*). From the viewpoint of dynamical systems, as the HSS loses its stability via *PB*, a pair of fixed points is generated, giving rise to IHSSs (Figure 3.1A, red lines) stabilized via saddle-node bifurcations (SN_{PB}s). These IHSSs represent symmetry-broken protein activity states and it describes simultaneously both polarization orientation of the cell: left- and right-polarization. There is no preference which side of the cell will acquire higher protein activity. Therefore, both possibilities ($u_{left} < u_{right}$ and $u_{left} > u_{right}$) are present as branches (upper and lower solid red lines in Figure 3.1A, respectively). In Region II, there is a co-existence between the HSS and the IHSSs before the *PB*, rendering the transition sub-critical. Because of the presence of unstable IHSS branches (dashed red line), the dynamical transition from HSS to stable IHSSs at this region is 'hard' which enables a threshold for polarization and thereby robustness to noise. Since the IHSSs render an unequal protein activity levels across the cell membrane, their corresponding attractors in the state space have an off-diagonal localization (Figure 3.1C, middle, red squares). This demonstrates that *PB* provides a unique mechanism for a dynamical transition from a homogeneous (HSS) to a single but heterogeneous (IHSS) state of the protein activity profile. Region III on the other hand, the state space is shared between the symmetry-broken states, hence only polarized state of the cells can be realized.

3.2 Symmetry breaking via unfolding of the pitchfork bifurcation

To numerically demonstrate different dynamical signatures characteristic to different regions of sub-critical pitchfork bifurcation, a simple protein network that resembles small Rho GTPase cycle is considered. It consists of two biochemical species (active, u and inactive, v : two forms of the same protein) that undergo interconversion. The forward reaction that produces u is a cooperative positive feedback from the active form onto its own production (via Guanine nucleotide exchange factor (GEF)). Multistability necessitates nonlinearity in at least one of the reaction terms and is implemented using third-order kinetics in the forward reaction. GAP mediated reverse reaction is assumed

to occur at a constant basal rate. The active form bound to the membrane diffuses more slowly than the inactive-cytosolic form and this spatially –distributed network is described using the following one-dimensional system of partial differential equations (PDEs),

$$\frac{\partial u}{\partial t} = F_u(u,v) + D_u \frac{\partial^2 u}{\partial x^2}$$

$$\frac{\partial v}{\partial t} = F_v(u,v) + D_v \frac{\partial^2 v}{\partial x^2}.$$

(3.6)

$F_u(u,v) = (k_0 + \gamma u^2/(K^2 + u^2))v - \delta u$, is the forward reaction term where k_0 is a basal GEF conversion rate and γ, K are the maximal rate and saturation parameter respectively of the Hill function . δ is the basal GAP-mediated inactivation rate in the reverse direction. $F_v(u,v) = -F_u(u,v)$, which is a consequence of mass conservation. To perform linear stability analysis, a simplified one-dimensional projection of Eq. (3.6) is considered,

$$\frac{du_L}{dt} = F_u(u_L, v_L) - \tilde{D}_u(u_L - u_R) = G_1(u_L, v_L, u_R)$$

$$\frac{dv_L}{dt} = F_v(u_L, v_L) - \tilde{D}_v(v_L - v_R) = G_2(u_L, v_L, v_R)$$

$$\frac{du_R}{dt} = F_u(u_R, v_R) - \tilde{D}_u(u_R - u_L) = G_3(u_L, u_R, v_R)$$

$$\frac{dv_R}{dt} = F_v(u_R, v_R) - \tilde{D}_v(v_R - v_L) = G_4(v_L, u_R, v_R)$$

(3.7)

where the subscripts L (left) and R (right) stand for diametrically opposite sides of the one-dimensional domain. $\tilde{D}_u$ and $\tilde{D}_v$ are the diffusion like terms.

Let, $\mathbf{U_s} = \begin{pmatrix} u_{Ls} \\ v_{Ls} \\ u_{Rs} \\ v_{Rs} \end{pmatrix}$ be the stable symmetric steady state of the system ($u_{Ls} = u_{Rs}$, $v_{Ls} = v_{Rs}$). A small amplitude perturbation on this symmetric steady state of the form,

$$
\begin{pmatrix} u_L(t) \\ v_L(t) \\ u_R(t) \\ v_R(t) \end{pmatrix} = \begin{pmatrix} u_{Ls} \\ v_{Ls} \\ u_{Rs} \\ v_{Rs} \end{pmatrix} + \begin{pmatrix} \delta u_L \\ \delta v_L \\ \delta u_R \\ \delta v_R \end{pmatrix} \cdot e^{\lambda t} \tag{3.8}
$$

yields a linearized equation,

$$
\lambda \begin{pmatrix} \dfrac{d\delta u_L}{dt} \\ \dfrac{d\delta v_L}{dt} \\ \dfrac{d\delta u_R}{dt} \\ \dfrac{d\delta v_R}{dt} \end{pmatrix} = \mathbf{J} \begin{pmatrix} \delta u_L \\ \delta v_L \\ \delta u_R \\ \delta v_R \end{pmatrix} \tag{3.9}
$$

where λ is the growth rate of the perturbation. $\mathbf{J}$ is the Jacobian of the system evaluated at the symmetric steady state given by,

$$
\mathbf{J} = \begin{pmatrix} \frac{\partial G_1}{\partial u_L} & \frac{\partial G_1}{\partial v_L} & \frac{\partial G_1}{\partial u_R} & 0 \\ \frac{\partial G_2}{\partial u_L} & \frac{\partial G_2}{\partial v_L} & 0 & \frac{\partial G_2}{\partial v_R} \\ \frac{\partial G_3}{\partial u_L} & 0 & \frac{\partial G_3}{\partial u_R} & \frac{\partial G_3}{\partial v_R} \\ 0 & \frac{\partial G_4}{\partial v_L} & \frac{\partial G_4}{\partial u_R} & \frac{\partial G_4}{\partial v_R} \end{pmatrix}
$$

To identify the existence of *PB* in the system, the condition given in Eq.(3.3) should be satisfied for an odd mode of the perturbation. For the one-dimensional projection (Eqs.(3.7)), the odd mode of the perturbation $(\delta \mathbf{U}(-\mathbf{x})) = -\delta \mathbf{U}(\mathbf{x}))$ must yield: $\delta u_L = -\delta u_R$ and $\delta v_L = -\delta v_R$. Substituting this into Eq.(3.34) to obtain $F_-(\lambda)$, in the limit $\lambda \to 0$ renders,

$$
\lim_{\lambda \to 0} F_-(\lambda) = det \begin{pmatrix} \left(\frac{\partial G_1}{\partial u_L} + \frac{\partial G_3}{\partial u_R}\right) - \left(\frac{\partial G_1}{\partial u_R} + \frac{\partial G_3}{\partial u_L}\right) & \left(\frac{\partial G_1}{\partial v_L} + \frac{\partial G_2}{\partial v_R}\right) \\ \left(\frac{\partial G_2}{\partial u_L} + \frac{\partial G_4}{\partial u_R}\right) & \left(\frac{\partial G_2}{\partial v_L} + \frac{\partial G_4}{\partial v_R}\right) - \left(\frac{\partial G_2}{\partial v_R} + \frac{\partial G_4}{\partial v_L}\right) \end{pmatrix} = 0 \tag{3.10}
$$

Thus, there exists a parameter set for which the existence of *PB* in the system Eq.(3.7) is guaranteed.

To identify whether the *PB* is sub-critical and thereby identify existence of a SN_{PB}, the solution of the system Eqs.(3.6) is approximated as in Eq.(3.4). For simplification, the Hill function in $F_u(u,v)$ is approximated by assuming $(K/u) >> 1$ to yield $F_u(u,v) = (k_0 + \gamma u^2)v - \delta u$,

$$u(x,t) = \phi(t)e^{ik_m x} + \phi^*(t)e^{-ik_m x} + u_0(t) + \sum_{n=2}^{3}(u_n(t)e^{nik_m x} + u_n^*(t)e^{-nik_m x})$$

$$v(x,t) = \phi(t)e^{ik_m x} + \phi^*(t)e^{-ik_m x} + v_0(t) + \sum_{n=2}^{3}(v_n(t)e^{nik_m x} + v_n^*(t)e^{-nik_m x})$$

(3.11)

The expansion is taken to $n = 3^{rd}$ order, rendering an amplitude equation of 5th order. By substituting expansions of solution in (3.11) into Eqs.(3.6) gives,

$$\frac{d\phi}{dt}e^{ik_m x} + \frac{du_0}{dt} + .. = k_0(\phi e^{ik_m x} + v_0..) + \gamma((3|\phi|^2\phi + 2u_0v_0\phi)e^{ik_m x} + 2(u_0+v_0)|\phi|^2 + ...)$$
$$- \delta(\phi e^{ik_m x} + u_0 + ..) - D_u(k_m^2\phi e^{ik_m x} + v_0 + ..)$$

(3.12)

collecting coefficients of harmonics up to first order on either side give ordinary differential equations that govern the evolution of amplitudes,

$$\frac{d\phi}{dt} = (k_0 - (D_u k_m^2 + \delta))\phi + 3\gamma|\phi|^2\phi + 2\gamma u_0 v_0 \phi$$

(3.13)

$$\frac{du_0}{dt} = (2\gamma|\phi|^2 - \delta)u_0 + (k_0 + 2\gamma|\phi|^2)v_0$$

(3.14)

As described in [65], the complex coefficients of the $n = 0^{th}, n = 2^{nd}$ and $n = 3^{rd}$ harmonics are approximated as power series of $\phi(t)$.

$$u_0(t) \approx u_0^{(2)} |\phi|^2 + ...$$

$$v_0(t) \approx v_0^{(2)} |\phi|^2 + ...$$

(3.15)

this approximate expansion of the coefficients are further substituted into Eqs. (3.13), (3.14) giving,

$$\frac{d\phi}{dt} = (k_0 - (D_u k_m^2 + \delta))\phi + 3\gamma |\phi|^2 \phi + 2\gamma u_0^{(2)} v_0^{(2)} |\phi|^4 \phi$$

(3.16)

$$\frac{du_0}{dt} = (2\gamma |\phi|^2 - \delta) u_0^{(2)} |\phi|^2 + (k_0 + 2\gamma |\phi|^2) u_0^{(2)} |\phi|^2$$

(3.17)

Higher order amplitudes were assumed to be in quasi-steady state thus Eq. (3.17) vanishes. We could then obtain $v_0^{(2)} \propto -u_0^{(2)}$. Substituting this into Eq. (3.16) yields the approximated leading harmonics ($n = 1^{th}$) amplitude expansion of the form,

$$\frac{d\phi}{dt} = c_1 \phi + c_2 \phi^3 - c_3 \phi^5$$

(3.18)

where $c_1 = (k_0 - (D_u k_m^2 + \delta))$, $c_2 = 3\gamma$ and $c_3 = 2\gamma (u_0^{(2)})^2$. Eq.(3.18) is of Stuart-Landau type and represents a normal form of a sub-critical pitchfork bifurcation. This shows the existence of SN_{PB} in the exemplary small Rho GTPase cycle.

To corroborate this, we also performed numerical bifurcation analysis on one-dimensional projection (Eqs.(3.7)). In the absence of any signal, the system exhibits a sub-critical pitchfork bifurcation with three distinct organization regimes (Figure 3.2 A, left. Compare with Figure 3.1A). The presence of an external inhomogeneous signal ($s_{left} \neq s_{right}$) act as an imperfect perturbation that destroys this bifurcation structure of the signal-free case. The symmetry-breaking bifurcation (*PB*) undergoes a universal unfolding which leads to the emergence of new symmetry broken IHSS branches (Figure 3.2A, right)[95]. Thus, the signal-induced unfolding causes reinforcement of the inhomogeneous nature to the steady states. Left- or right- orientation of the IHSS depends on the signal localization (here in this case both left- and right- orientation are depicted

corresponding to signals $(s_{left}, s_{right}) = (0.02, 0.0)$ and $(s_{left}, s_{right}) = (0.0, 0.02)$ respectively). The extend of unfolding characterized by how different u_{left} is to u_{right}, depends on the strength of the inhomogeneous signal. In order to demonstrate this dependence, the evolution of the upper inhomogeneous branch in Figure 3.2A (left) is traced as a function of s_{left} (keeping $s_{right} = 0$). The two-dimensional bifurcation diagram shows that, when $s_{left} = 0$, different dynamical regimes (regions I, II, and III) exist as in Figure 3.2A (left). As s_{left} is increased, the inhomogeneous nature is re-inforced globally, including in region I. The inhomogeneity in the unfolded branches is quantified using degree of inhomogeneity (DI) which is the percentage difference between left- and right- responses. Region I in the absence of signal has 0 % DI due to stable homogeneous branch while the upper IHSS branch in regions II and III has >80 % DI. As s_{left} is increased, this level of inhomogeneity is conserved in regions II and III but in region I, it increases from 0 % to 80 %. Simultaneously, two $SN_{PB}s$ (black dots) come together and region II vanishes after a threshold signal strength marked by a cusp bifurcation (star). Beyond this point, the cell only has symmetry broken monostability.

Due to unfolding, region I that initially ($S_L = 0.0, S_R = 0.0$) only allowed basal, unpolarized state can now achieve higher degree of polarization depending on the external signal strength and can effectively match with DI values of region II and region III (Figure 3.2B, horizontal and vertical dashed gray line intersection). The temporal profile of response in Figure 3.2C shows that, an initially unpolarized cell organized in region I, in the presence of an inhomogeneous signal ($s_{left} = 0.02$ and $s_{right} = 0.0$), achieves robust polarization. Thus universal unfolding of symmetry breaking pitchfork bifurcation enables polarization of protein activity profile. However, robust polarization that enables external gradient sensing alone cannot facilitate optimal response of cell in a changing environment. The plasticity of this polarized state in the presence of novel signals is crucial. We demonstrate further that, initial parameter organization of the system close to the SN_PBs endows the system with this plasticity in its response.

3.3   Organization at criticality and "ghost" of the saddle node

In Figure 3.3A, at the transition between region I and region II, in the vicinity of the $SN_{PB}s$ (magenta region), the system is monostable and it corresponds to an un-polarized state. As demonstrated before, a single homogeneous attractor characterizes the region

A

B   C
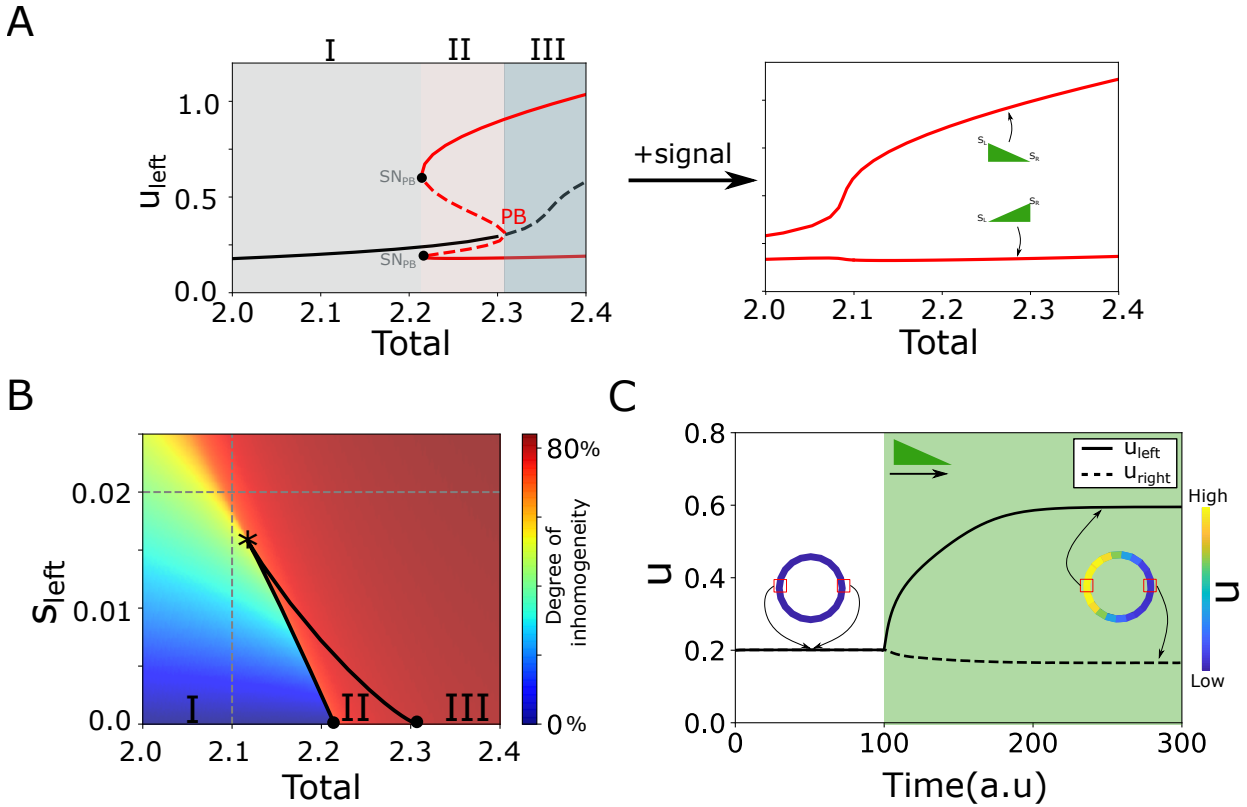
Figure 3.2 Signal induced unfolding for pitchfork bifurcation enables robust polariza-tion. A, Left: sub-critical pitchfork bifurcation corresponding to Eq. 3.7. Notation and line description as in Figure 3.1 A. Right: pitchfork unfolding in the presence of inhomogeneous signals. Top branch: $s_{left} = 0.02, s_{right} = 0.0$, bottom branch: $s_{left} = 0.0, s_{right} = 0.02$. B, Two-parameter ($s_{left}$, Total) bifurcation diagram depicting degree of inhomogeneity (DI). Vertical and horizontal dashed gray line's intersection: organization in Region I that achieves 80 % DI. Black dots : SN_{PB} and PB in A. Black line encloses Region II as a function of signal. C: Time series depicting robust polarization corresponding to dashed gray line's inter-section in (B), Total=2.1, $s_{left} = 0.02$. Black solid/dashed line: u_{left}/u_{right}. Other parameters: $k_0 = 0.067$, $\gamma = 1$, $K = 1$, $\delta = 1$, $\tilde{D}_u = \tilde{D}_v = 0.01$.

I (Figure 3.1C, left). Since the critical transition region is in region I, a single global attractor exist (Figure 3.3A, B black circle) but because of the vicinity of the SN_{PB} there are regions in the state-space where the flow of the system is partially attracted, despite the absence of a stable attractor at that region (Figure 3.3B, triangle). Thus those regions are metastabile and trajectories starting near them have to go through a "bottleneck" before reaching the basal attractor. The presence of this metastable state is unique to the organization of the system at this critical region. This metastability

is because of a saddle -remnant or "ghost" and has been previously associated in dynamical systems with delayed dynamics or slow remnants [37].

Recently, in [35], we have demonstrated that a saddle-node "ghost" serves as a unique dynamical mechanism that manifests as a transient temporal memory of the cell receptor activity, enabling it to be maintained at high levels for a limited period after signal removal. Moreover, this trapping in the dynamically-metastable memory state does not hinder sensing of and adapting to subsequent signals. In the context of cellular polarization via sub-critical pitchfork bifurcation critical organization thus unifies features from two unique bifurcations: *PB* and *SN*. For instance, in the presence of a transient inhomogeneous signal, unfolding of the *PB* enables robust polarization of protein activity. As the signal is removed, the trajectory of this polarized state passes through the metastable state. The polarized signaling state is maintained for a transient period after removal of the signal, corresponding to the manifestation of memory of the localization of the encountered signal (Figure 3.4A).
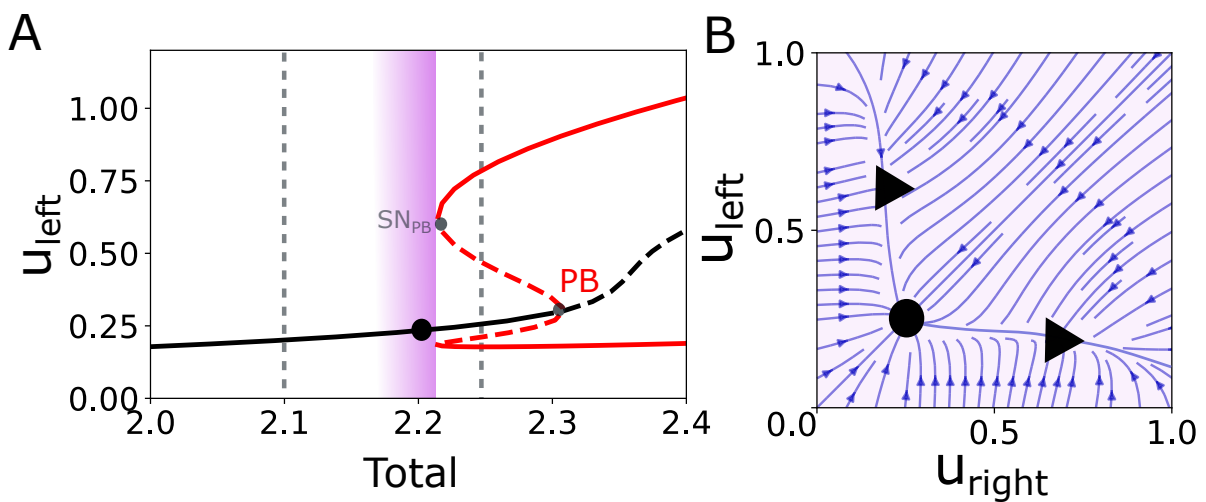
Figure 3.3 Critical organization and metastability through "ghost" attractors. A, Subcritical pitchfork bifurcation same as in Figure3.3 A. Magenta shaded region: region of criticality. Dashed vertical lines: parameter organization at region I (left) and II (right). B, State space for organization at criticality (Total=2.21). Triangle: metastable states/"ghost" attractors. Arrows and markers as in Figure 3.1 C.

3.3.1 Signal induced quasi-potential landscape transitions reveals the origin of transient memory at criticality

To understand how transient memory occurs for critical organization, we studied qualitatively, the system's behavior by analyzing how the response evolves with the changes in the geometry of the underlying state space. The transient inhomogeneous signal in Figure 3.4A (green shaded region), is an external parameter to the system that modulates the steady-state structure of the state space. In such non-autonomous or input-driven systems, either the geometry of the underlying state space can be altered (change in the positioning, shape, and size of the attractors), or its topology (change in the number or stability of the attractors) [96, 97].
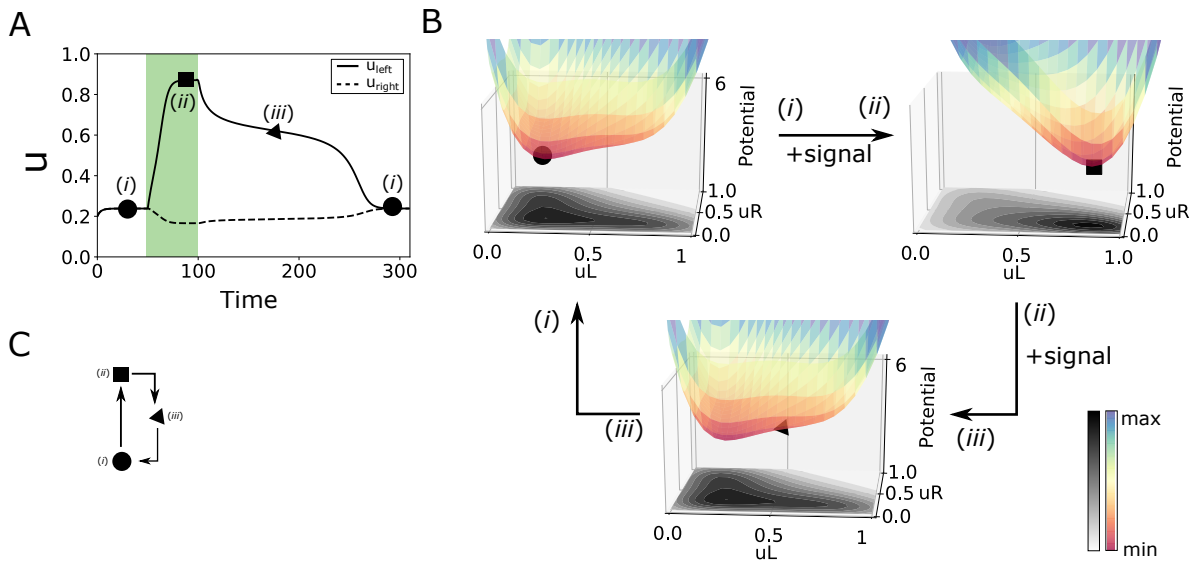
Figure 3.4 Metastability gives rise to transient memory of polarized protein activity. A, Temporal profile of protein response (Eqs. 3.7) upon transient gradient stimulation at critical organization ($Total = 2.21$, signal : (s_{left},s_{right})=(0.01,0)). Solid/dashed line : u_{left}/u_{right}. Green shaded region: signal presence. B, Potential landscape transitions corresponding to A. Gray projection in the $u_{left} - u_{right}$ plane: steady state probability (P_{ss}). C, Reduced state transitions corresponding to A. Circle/*i*, square/*ii*, triangle/*iii* : unpolarized, polarized and metastable state respectively. Arrows : state transitions.

We can use the dynamics of the system described by Eqs. 3.7 to assign potentials to the attractor states and determine their distinct relative depth within the same frame of reference. The idea of a potential landscape helps to describe how forces acting in a system relate to its global behavior. The state-space trajectories flow downhill the landscapes, towards the valleys defined by the steady-states. A global stable attractor

thus translates to a potential surface with a global minimum where all the trajectories end up. In order to estimate the potential associated with non-equilibrium systems, [98] estimated the steady-state probability (P_{ss}) and then estimated the associated potential using the relation $U = -log(P_{ss})$. The time evolution of the P_{ss}, and hence U, not only depends on the forces that drive the system (Eqs. 3.7) but also the stochastic transitions between every possible point in the state space. The solution to the resulting Fokker-Planck diffusion equation for the system can be used to estimate the potential, U.

At critical organization regime, in the absence of the signal, the cell exhibits an initial un-polarized state (Figure. 3.4A, circle, i). In the corresponding potential landscape, this state resides at the global minima (Figure. 3.4B, top left, circle). The presence of an inhomogeneous signal (Figure. 3.4A, green shaded region) induces transition from this basal, un-polarized state to active, polarized state in a switch-like manner (transition $i \rightarrow ii$). This transition happens via the unfolding of the *PB*. In the state space, this corresponds to a topological change and causes the vanishing of the initial basal valley and the emergence of a new global minimum which is the polarized state (square). Upon signal removal, these topological transitions are reversed ($ii \rightarrow iii$, $iii \rightarrow i$). However, there is a delay between establishing the single stable attractor (state i) and the system trajectory eventually converging to it, resulting in prolonged polarized protein activity before relaxation to basal level (Figure. 3.4A). During the transition from polarized- state to basal-state (triangle, *iii*), because of the shallow slope of the potential landscape, the state-space retains a transient memory of polarized receptor activity (Figure. 3.4B, bottom, triangle). A reduced state transition diagram (Figure. 3.4C) captures this crucial feature associated with the critical organization. The reversible signal-induced transition shows unification of features arising from the two bifurcations: polarization through unfolding of *PB* (transition $i \rightarrow ii$) and memory of the polarized state (*iii*, transition $ii \rightarrow iii \rightarrow i$) through "ghost" of the SN_{PB}.

In contrast to this, if the system organization in the monostable regime (region I, dashed vertical line to the left of magenta shaded region, Figure. 3.3A), the system does not exhibit any memory in protein activity (Figure. 3.5A). During the reversible transition, an intermediate state is absent as shown in the reduced state transition diagram (Figure. 3.5A). In this case, the signal induced changes in the state space geometry of the system (adding/removing stimulus: $i \rightarrow ii$/ $ii \rightarrow i$), that triggers continuous and reversible re-positioning of the single steady-state attractor, captures the state trajectory. This leads to a receptor response that closely follows the input (Figure. 3.5A).
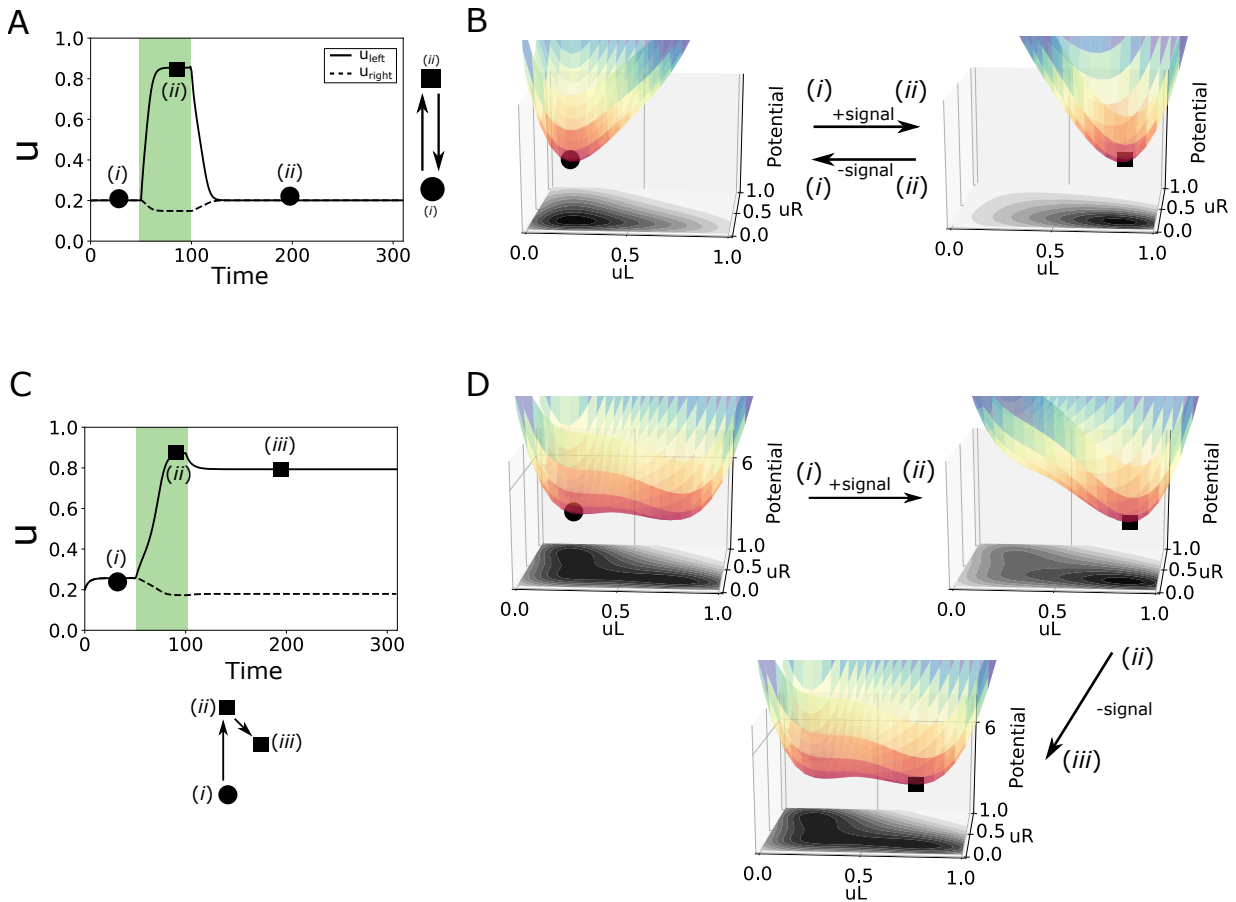
Figure 3.5 Away from critical organization leads to lack of transient memory. A, Left: Temporal response upon transient gradient stimulation for organization in region I (*Total* = 2.1, dashed vertical line in Figure. 3.3A). Right: Corresponding reduced state transition. B, Potential landscape transitions associated with A. C, Top: Same as in A but for organization in region II (*Total* = 2.25, dashed vertical line in Figure. 3.3A). Bottom: Corresponding reduced state transition. D, Potential landscape transitions associated with C. Parameters, colours, markers and arrows as in Figure. 3.4

When the system is poised in multistable region II (dashed vertical line to the right of the magenta shaded region, Figure. 3.3A), in the absence of signal, the system has three minima corresponding to three stable states, the un-polarized HSS (in which the system initially resides, Figure. 3.5C, D, circle *i*) and two IHSSs that corresponds to left- and right-polarized states. (Figure. 3.5D left top, P_{ss} projection). In the presence of signal, this HSS vanishes (transition $i \rightarrow ii$), and result in the left-polarized state (square *ii*). The left-polarized state is favored because of the left-localization of the signal applied. The signal removal reverses the topological changes and re-establishes the initial multistability (transition $ii \rightarrow iii$). However, the trajectory stays at the

occupied left-polarized state (Figure. 3.5D, bottom). Thus, a single signal leads to permanent polarization and will hinder further responsiveness to upcoming signals due to long-term memory (Figure. 3.5C). If the cell is posed at region III, beyond the PB (Figure. 3.3A), then an un-polarized state does not exist hence state will be locked in one of the polarized states again rendering permanent memory (results not shown).

Comparison between the shape of the potential landscape at different regions of organizations in the absence of signal (compare Figs. 3.4B, 3.5B, D) leads us to the conclusion that the shallow slope which is a manifestation of metastability is unique to the organization at criticality and this endows a transient memory of polarized protein activity. For cells, memorization of recent stimuli encounter is crucial when the signals are time-varying. The properties of the state in which this information is stored then become crucial. For instance, the organization in the multistable region II endows a permanent memory of the stimulus encounter because of the stable polarized attractor in which the trajectory ends up. The state of the cell cannot escape from this potential valley and new signals fail to perturb this stable state. The memory state corresponding to the critical organization is metastable. Therefore, the memory of the polarization response is transient and because of the shallow slope of the potential landscape state can be further triggered by new signals.

3.3.2 Dynamic temporal memory enables processing of time-varying signals

To integrate and interpret the information contained in time-varying signals the transient memory in protein activity polarization must be dynamic. We, therefore, probed the features of this transient memory resulting from the saddle-node of the PB using two subsequent inhomogeneous signals from the same direction with an inter-stimulation interval shorter than the duration of the transient memory. The numerical simulations, when the cell is posed at criticality, demonstrate that the protein activity polarization could rapidly adapt to the second signal (Figure. 3.6A, top). When the second signal is posed to the cell, the trajectory is at the metastable state (t=200 sec). The presence of the second signal again creates the polarized attractor (square, ii) and the trajectory is triggered from a metastable state to the polarized state (transition $iii \rightarrow ii$) suggesting that the cell has responsiveness to upcoming stimuli while being in the memory state. After the removal of this second stimuli, the state transits from the polarized state to the un-polarized state through the metastable state (transition $ii \rightarrow iii \rightarrow i$). These transitions are summarized in the reduced state transition diagram (Figure. 3.6A,

bottom). The metastable state thus acts as a flexible node in this transition from which it can be shuttled to polarized or unpolarized states depending on the presence or absence of signal.

The absence of such a flexible node affects how the system responds to the second stimuli. As demonstrated in the previous session, the cell loses transient memory when it is organized away from the critical region (Figure. 3.5). If the cell is organized in the region I (organization same as Figure. 3.5A), because of the absence of memory state, history dependent signal integration is not possible and the response closely follows the signals (Figure 3.6B, top). Subsequent transient signals shuttle the response between unpolarized and polarized states (Figure 3.6B, bottom). Meanwhile, if the cell is organized in region II (same as Figure 3.5B), the first signal polarizes the cell and because of the long-term memory, the responsiveness to further stimuli is hindered (Figure 3.6C). The cell remains polarized after its encounter with the first signal. Due to multistability at this region, noise-induced transition to one of the polarized states is also probable. Such spontaneous polarization in the absence of external signals also leaves the cell in a state where it cannot perceive new signals.
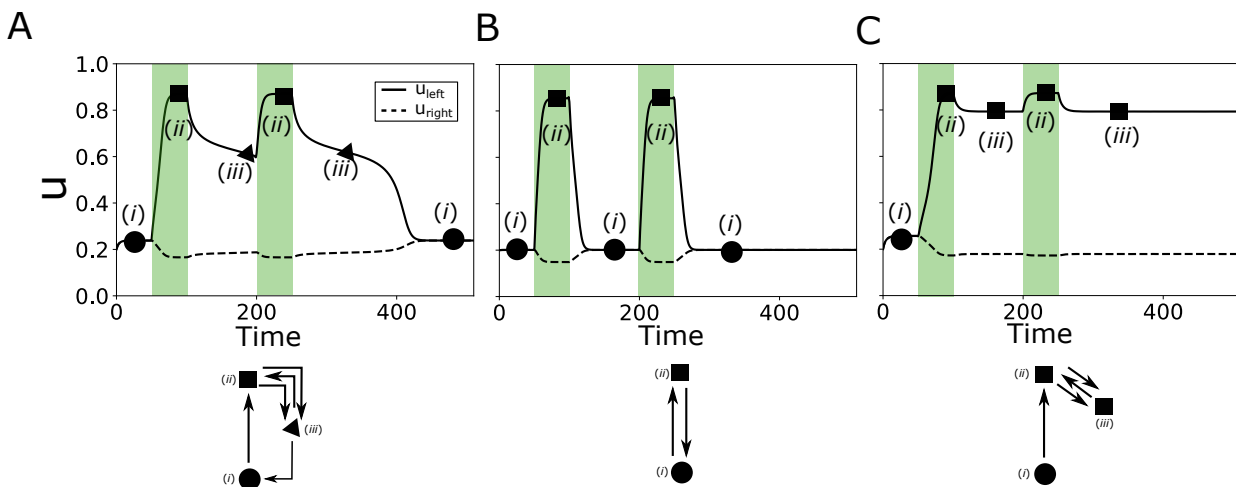
Figure 3.6 Transient memory of polarization enables signal integration. A, Top: Temporal response of protein activity upon two consequent gradient stimulation for organization at criticality. B,C, Top: same as in A but for organization at region I and region II respectively. A,B,C, Bottom: Schemes of corresponding reduced state transition. Parameters, colours, markers and arrows as in Figure3.4.

Thus, different parameter organization causes different responses to time-varying signals. Figure 3.6A suggests that metastability enables integration of subsequent signals by prolonging the period in which the protein activity is maintained high

longer than in the case of a single stimulation (compare Figs. 3.4A and 3.6A). Such signal integration capability is not present for organization away from criticality. Organization in region I lead to response duration equal to the duration of the signals and the organization in region II, because of the permanent memory, leaves the presence or absence of subsequent signals irrelevant.

The critical organization maintains protein network dynamics away from a steady state and through this metastability, the protein response exhibits plasticity in sensing and responsiveness to dynamic signals in real-time. On the other hand, computation through stable attractors is not sufficient to describe this plasticity. Thus a SubPB mechanism (sub-critical pitchfork bifurcation with the critical organization) unifies two properties required for optimal response: robust polarization via unfolding of *PB* and plasticity in response via metastability from *SN*. So far the principles of SubPB mechanism have been demonstrated on a one-dimensional projection model. Introducing spatial dimension is required to capture how it shapes the protein activity profiles in cells when they are posed with dynamic spatial gradients of signals.

3.4 Gradient sensing and memory in polarization by SubPB mechanism

To investigate whether the proposed SubPB mechanism enables processing of dynamic gradient signals, a cell is subjected with a transient gradient of signal from one side as in Figure 3.7A. The reaction-diffusion system in Eq. 3.26 was used to demonstrate the gradient sensing capabilities of SubPB mechanism. In this conceptual model, since *u* and *v* represent active and inactive forms of a small Rho GTPase, the effect of an external signal can be introduced such that it causes the conversion of *v* to *u*. This term implicitly captures the signal-induced up-regulation of GEFs that mediates this conversion [86]. To perform the reaction-diffusion simulation, the cell membrane contour was divided into radial bins from $0 - 2\pi$. The activity state of *u* along the cell membrane is initiated around the basal, homogeneous steady state that corresponds to the un-polarized state. The cell is then subjected to a stimulation protocol as in Figure 3.7B. The gradient from the top was made dynamic by changing its steepness progressively over time from steep to 50% shallower (Figure 3.7C, top), and is switched off after a transient period of time. Kymograph analysis (Figure 3.7C, bottom) shows that the stimulation leads to rapid polarization of response protein (*u*) in the direction of the maximal signal strength. The polarized signaling state was maintained for
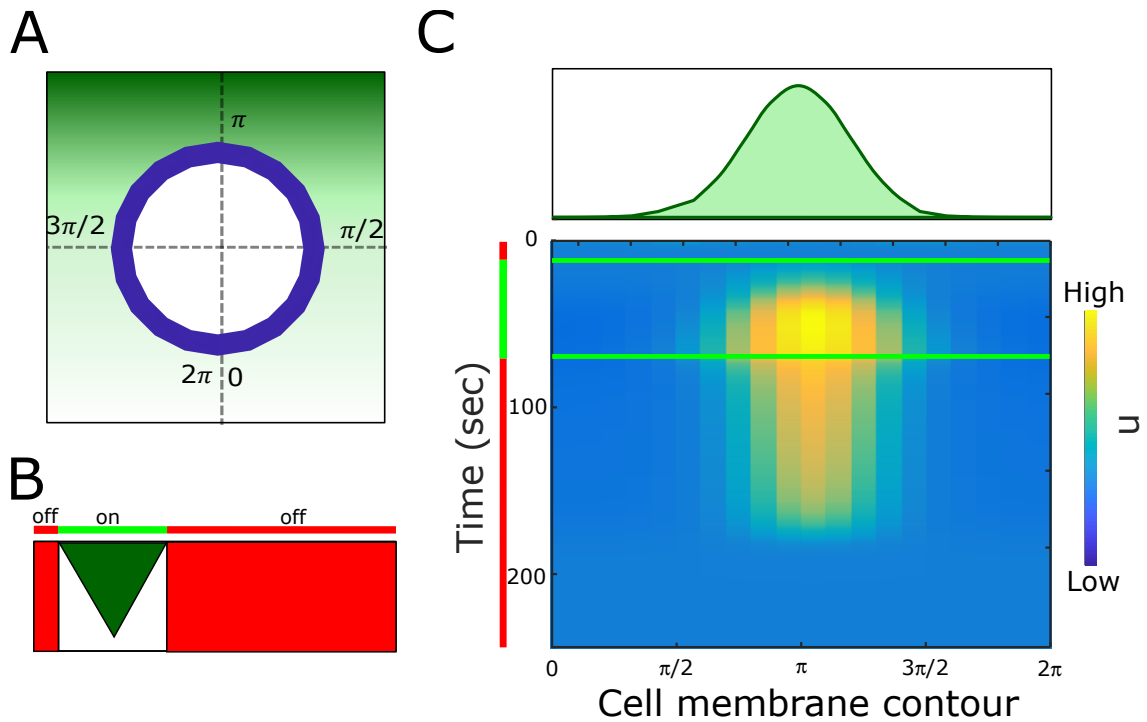
Figure 3.7 SubPB mechanism underlies optimal sensing of dynamic spatial-temporal signals. A, Scheme of a cell stimulated with a gradient emanating from the top. Cell membrane contour from $0 - 2\pi$. B, Scheme of stimulation protocol with horizontal dimension indicating time. Green/red: presence/absence of dynamic gradient. C, Top: Evolution of spatial gradient distribution. Bottom: Kymograph of u for organization at criticality from reaction-diffusion simulations of the network corresponding to Eq. 3.6. Horizontal green lines: Beginning and end of gradient. Left vertical bar: Signal presence or absence as in B.

a transient period after removal of the gradient, corresponding to the manifestation of memory of localization of the previously encountered signal. After maintaining polarized activity in the memory state, the system reverts to its initial un-polarized state. The importance of this memory can be substantiated by considering situations where the spatial cues are numerous and diverse, changing both in time and space. To understand such a situation let us consider a slightly complex gradient field.

3.4.1   Memory enabled plasticity and signal integration in polarization response

To further examine the sensitivity and signal integration capabilities of SubPB mechanism, a slightly complex stimulation protocol is introduced (Figure 3.8A). Here, in

addition to two subsequent gradients from the same direction, the third gradient with reversed localization is also introduced (Figure 3.8B, top). The second gradient is short and static (does not change its steepness over time) and is introduced within the memory phase of the first gradient. The response kymograph (Figure 3.8B, bottom) shows that the transient memory enables the integration of these two signals with prolonged protein activity polarization and subsequently when the dynamic reversed gradient is introduced the polarization direction rapidly reverses and adapt to the reversed gradient localization. This shows that a polarized memory state retains responsiveness to novel cues irrespective of its direction of localization. This feature is particularly important when it comes to cellular navigation in chemoattractant fields. In such a situation, from the frame of reference of the cell, the localization of the source of gradients changes depending on the cell's movement and its orientation. In addition to that, even if the gradient has a stable profile, due to the movement of the cell towards the source, the cell perceives changing steepness. In the simulation, this complexity is tested by the use of dynamic gradient and SubPB mechanism could account for this changing steepness by maintaining the extended polarized front.

With these results, we, therefore, propose that the SubPB mechanism captures features of polarization that enable optimal cellular response under changing gradient fields. The critical parameter organization is the key feature of SubPB mechanism. Because of this organization, the *PB* will confer the polarization features and the meta-stable state from the *SN_{PB}* "ghost" will allow for the memory of the polarized state and thereby capability for temporal signal integration.

3.5   Polarization mechanisms of existing mathematical models rely on organization in stable attractor regime

As already mentioned in the introduction, the literature on models for cell polarization is large, with a variety of models of many types [56]. It poses a challenge when it is necessary to understand and compare their functionalities. One way is by simulating the response of models to various stimulation protocols, but this can only probe a limited set of parameters in each case. As a solution to this, it is necessary to understand the dynamical mechanism that underlies these different mathematical models. The evolution of the state trajectory of the biochemical system corresponding to these models depends on the topology (attractor number, position, and stability) of its state-space. Understanding the bifurcations associated with the dynamical system is
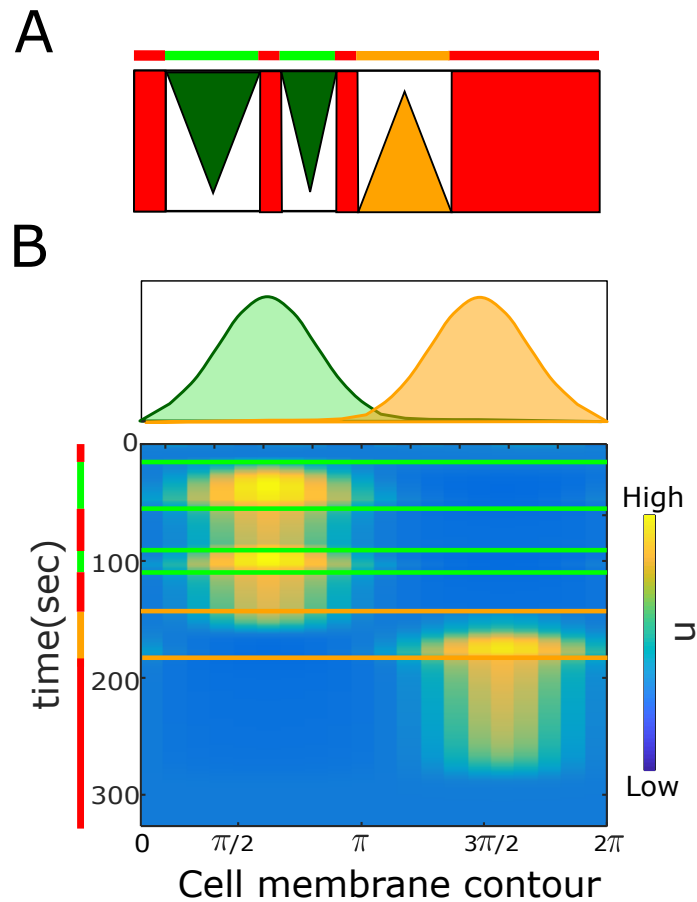
Figure 3.8 SubPB mechanism enables history-dependent activity response to spatially and temporally varying gradient fields. A, Scheme of dynamic spatial-temporal gradient field implemented in the simulations Green(orange)/red: gradient presence/absence. B, Top: Snapshots of spatial gradients with opposite localizations. Bottom: kymograph of *u* corresponding to organization at criticality. Colour coding and lines as in Figure 3.7.

thus important since it captures the nature of topological transitions as the system's intrinsic or extrinsic parameter changes. As discussed in the introduction (section 1.4), the signatures of different types of bifurcations(Saddle node, Transcritical or Pitchfork bifurcation) on system dynamics are different since they correspond to distinct topological structures and the characteristics of any process directly follow from the type of those dynamical bifurcations through which they emerge. In this chapter, different existing models for cellular polarization are analyzed in detail from the perspective of their underlying bifurcation/symmetry breaking mechanism. Thus this approach further helps us to compare and study different polarization features

associated with these models and how it is different from the SubPB mechanism that we are proposing.

As discussed in the introduction, we have categorized the most prominent polarity models into three distinct classes, 1) Wave Pinning type, 2) Turing-type and 3) LEGI-type models. To relate their respective polarization features with the underlying dynamical mechanism, we utilized linear perturbation analysis (LPA) that allows us to identify the dynamical transitions in the RD models employing bifurcation analysis and then reaction-diffusion simulations to demonstrate those features. For all the models, these simulations of the RD models were performed on a one-dimensional domain of length $L = 10\mu m$ using no-flux boundary conditions.

Wave Pinning-type models

The exemplary protein interaction network that exhibit wave pinning consists of a membrane-bound receptor protein(u) that receives an extra-cellular signal (s) and it has positive feedback activation onto its production that converts its cytosolic inactive form (u) (Figure 3.9A). The reaction-diffusion equation for the model is given by the PDEs,

$$\frac{\partial u}{\partial t} = F_u(u,v) + D_u \frac{\partial^2 u}{\partial x^2}$$

$$\frac{\partial v}{\partial t} = F_v(u,v) + D_v \frac{\partial^2 v}{\partial x^2}.$$

(3.19)

where $F_u(u,v)$ and $F_v(u,v)$ are the reaction terms corresponding to u and v same as in Eq. 3.6 and total protein mass conservation (Total, $T = u + v$) implies that $F_v(u,v) = -F_u(u,v)$. D_u, D_v are the diffusion constants of u and v such that $D_u << D_v$. In order to elucidate the underlying dynamical mechanism, LPA is performed on the PDEs system in Eq. 3.19. It gives a system of ODEs that describes the evolution of local and global variables associated with u and v (see section 1.7 for more details).
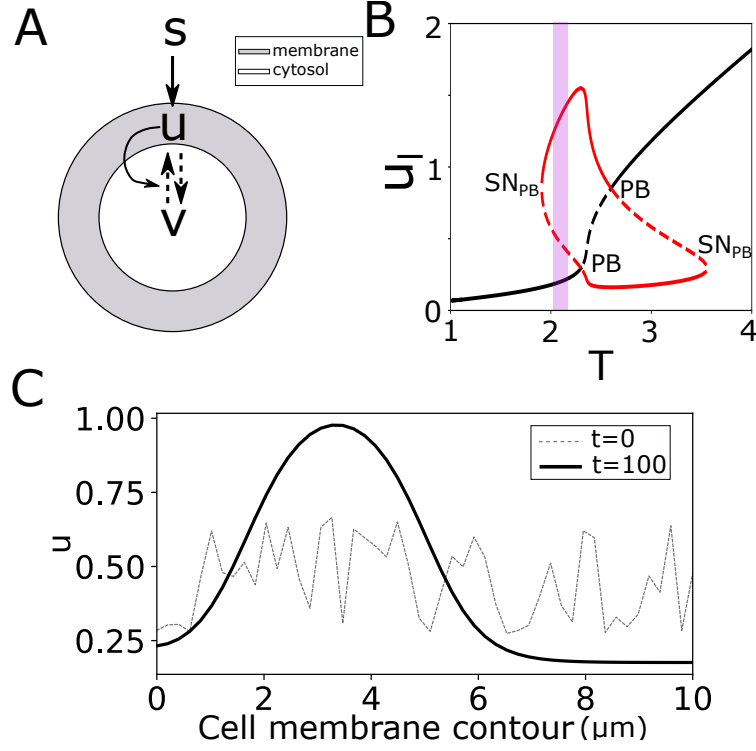
Figure 3.9 Wave pinning model has *PB* as symmetry breaking mechanism. A, Schematic of exemplary protein network exhibiting Wave pinning. Dashed line with arrows: conversion, Solid lines with arrowhead: activating reaction links. B, Bifurcation diagram corresponding to reaction network in (A) for $s = 0$. Solid/dashed lines: stable/unstable states. Black/red: HSS/IHSS. SN_{PB}: Saddle-node bifurcation. *PB*: Pitchfork bifurcation. Magenta shade region: parameter organization. C, Spontaneous polarization in u with noisy initial condition around the HSS corresponding to magenta region in (B). Noise intensity, $\sigma = 0.2$. Other parameters: $k_0 = 0.067$, $\gamma = 1$, $K = 1$, $\delta = 1$, $D_u = 0.1$, $D_v = 10$.

$$\frac{du_l}{dt} = F_u(u_l, v_g)$$

$$\frac{du_g}{dt} = F_u(u_g, v_g)$$

(3.20)

where $v_g = T - u_g$. The dynamics of these ODEs under a wide range of parameter variations can be explored readily using standard bifurcation software [60]. The result of the analysis in Figure 3.9B shows that the polarization features of the WP-type model rely on a symmetry-breaking pitchfork bifurcation (*PB*). Variation of the steady-state value of u_{local} with respect to the bifurcation parameter T shows that at lower values of

the total protein amount (T), the system only has a stable homogeneous branch (black solid line). This state loses stability via a pitchfork bifurcation (*PB*). In contrast to the SubPB mechanism, WP-type has a parameter organization inside the symmetry broken regime (pink shaded region) which is equivalent to the organization in region II in Figure 3.1C. At this region of organization, there is a stable homogeneous branch (solid dark line) that corresponds to an un-polarized protein activity state, together with inhomogeneous branches (solid/dashed: stable/unstable). The stable branches stems from spatial features captured by the LPA equations corresponds to polarized protein activity states. Because of this coexistence, the existing dynamical transition is "hard" (also see section 1.4) and would in principle enable a threshold activation (defined by the unstable IHSS branches) and thereby robustness to noise. However, RD simulations show that, even if the system state is initiated around the un-polarized stable state, higher intensity of noise enough to jump over the threshold, leading to spontaneous polarization(Figure 3.9C) where the absence of the direction cue leads to random localization of polarization peak on the cell membrane. The threshold value required for activation varies across this region II (between SN_{PB} and *PB*). As the system organization moves towards the SN_{PB} from the left, it becomes harder to cause spontaneous polarization as the slope of unstable IHSS branches increases.

Turing-type models

The Turing-type models, such as Goryachev et. al. [80] or Otsuji et. al. [79], has protein interaction network similar to the WP-type (Figure 3.10A). The membrane-bound u has positive feedback, that resembles auto-catalytic activation, and coverts more of v to u. The RD model description for Turing-type models is the same as Eqs. 3.19.

As an exemplar, reaction term ($F_u(u, v)$) of Otsuji model(OT) is considered and is given by, $F_u(u, v) = a_1(v - \frac{(u+v)}{(a_2(u+v)+1)^2})$ where a_1 and a_2 are the parameters of the model and has mass conservation similar to WP-type. Similar to WP-type, the OT model also meet the criteria for applying LPA ($D_v >> D_u$). In Otsuji et. al. is reported that the reaction kinetics allow for a classical Turing instability that causes symmetry breaking. The bifurcation analysis on this system reveals that the model relies on a symmetry-breaking transcritical bifurcation (*TC* in Figure 3.10B), that marks the transition from un-polarized (homogeneous steady state) to polarized (symmetry-broken steady-state) protein activity state. This suggests that, in this system, generic Turing instability manifest as a *TC* bifurcation. By performing Linear stability analysis along with
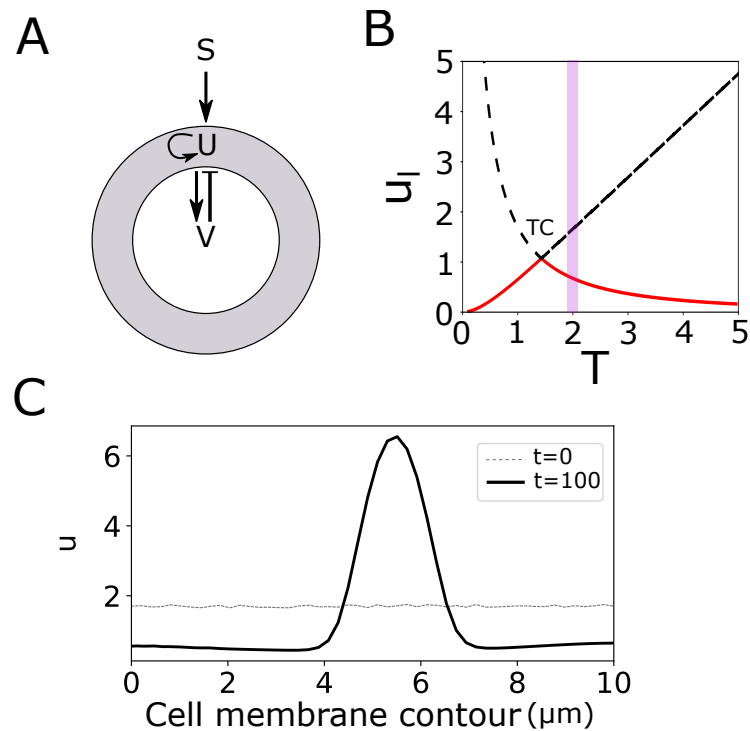
Figure 3.10 Turing model has TC bifurcation as symmetry breaking mechanism. A, Schematic of exemplary protein network as in [79]. Dashed arrows: conversion, Solid lines with arrowhead: activating reaction links. B, Bifurcation diagram corresponding to reaction network in (A) with $s = 0$. Solid/dashed lines: stable/unstable states. Black/red: HSS/IHSS. TC: Transcritical bifurcation. Magenta shade region: parameter organization. C, Spontaneous polarization in u with noisy initial condition around the HSS corresponding to magenta region in B. noise intensity, $\sigma = 0.1$. Other parameters: $a_1 = 2.5$, $a_2 = 0.7$, $D_u = 0.1$, $D_v = 10$.

LPA, it has been previously illustrated that TC bifurcation marks the onset of Turing instability [61]. For small values of T, only the global HSS branch(black line) is stable. This branch exchanges stability with unstable symmetry broken branch(red dashed) at super-critical TC bifurcation. Thereafter, for larger T values, we have a Turing regime, whereby a perturbation of arbitrarily small amplitude can lead to patterning. This is because the un-polarized state is unstable to start with and even the presence of negligible noise levels leads to symmetry breaking (Figure 3.10C) and polarized protein activity profile. The absence of a threshold for activation thus enables a spontaneous "soft" transition in contrast to the "hard" transition in WP-type.

LEGI-type models

The LEGI-type models have a network architecture that consists of three interacting proteins in which the effect from the signal, s reaches the response protein u via two different branches. One activation branch through another membrane-bound, slow diffusing activator protein w and an inhibition branch through a cytosolic, fast diffusing inhibitor v (Figure 3.11A). This constitutes an incoherent feed-forward loop that has characteristic global adaptation in the sustained signal presence. Three-component RD model for LEGI-type is given by,

$$\frac{\partial u}{\partial t} = F_u(u,v,w) + D_u \frac{\partial^2 u}{\partial x^2}$$

$$\frac{\partial v}{\partial t} = F_v(u,v,w) + D_v \frac{\partial^2 v}{\partial x^2} \tag{3.21}$$

$$\frac{\partial w}{\partial t} = F_w(u,v,w) + D_w \frac{\partial^2 w}{\partial x^2}$$

where $F_u(u,v,w) = -k_{-u}w$, $F_v(u,v,w) = -k_{-v}v$ and $F_w(u,v,w) = k_w w(u_{total} - u) - k_{-w}uv$. The distinct spatial localization of the components (w and u at the membrane, v in cytosol) implies discrepancy between diffusion constant values that is required for applying LPA ($D_v >> D_u$, $D_v >> D_w$ and $D_u \approx D_v$). LPA shows that in contrast to WP- and Turing- type models, polarization features of the LEGI-type model do not rely on any distinct dynamical transition. With total amount of response protein (u_{total}) as the parameter, LEGI-type exhibits homogeneous monostability (Figure 3.11B). Such a monostable organization (magenta region) does not facilitate spontaneous symmetry breaking. That means in the absence of any signal, irrespective of the noise intensity in the initial conditions, the homogeneous protein activity distribution is restored asymptotically (Figure 3.11C). However, in the presence of a gradient signal, local production of response protein u is triggered at the side closest to the gradient source. Simultaneously, the same signal triggers fast global inhibition of u activity at the farther end. This concerted reaction results in u activity polarization along the cell membrane.

Using bifurcation analysis, we have identified the underlying mechanisms associated with the main three classes of models. The dynamical signatures of these mechanisms are independent of the parameter sets that we use. For example, independent of the parameter set, due to the monostable behavior of LEGI-type, it cannot allow for
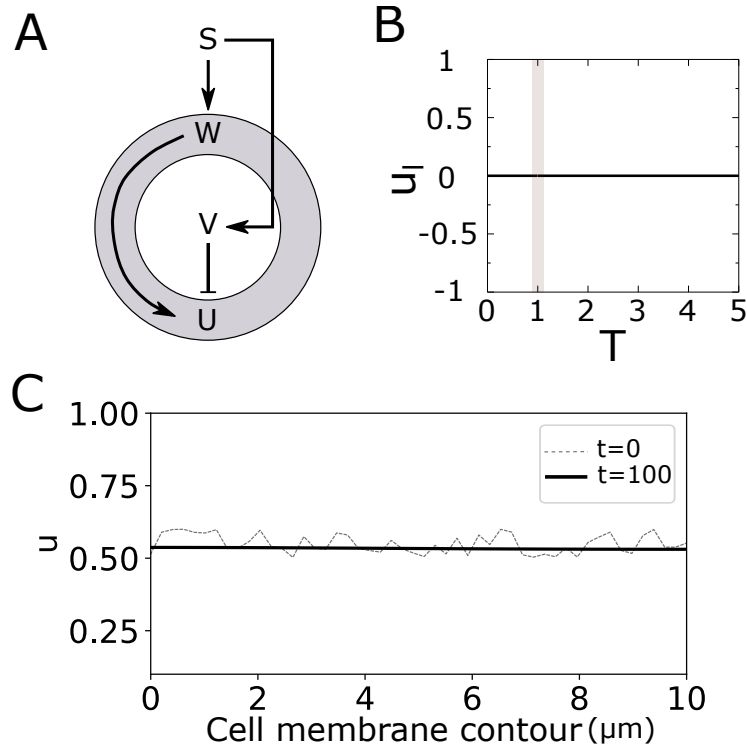
Figure 3.11 LEGI-type lacks a symmetry breaking mechanism. A, Schematic of protein network with incoherent feed forward topology. Signal (*s*) activate *w* and inhibit *v*. *v* and *w* activate response protein *u*. Solid lines with arrowhead: activating reaction links. B, Bifurcation diagram corresponding to reaction network in (A) with $s = 0$. Solid black line: stable homogeneous state. Magenta shaded region: parameter organization. C, Lack of spontaneous polarization in *u*. Noise intensity, $\sigma = 0.1$. Parameters: $k_{-u} = 2$, $k_{-v} = 1$, $k_w = k_{-w} = 1$, $D_u = 0.1$, $D_v = 10$.

spontaneous symmetry breaking. Thus dynamical mechanisms enable a platform for model comparison.

In short, given the different bifurcation scenarios, the different model types will display different polarization features, as they are determined by the intrinsic characteristics of the bifurcations which are present in the system. What is however common about all of the current models (WP-, Turing- and LEGI-types), as well as all remaining in the literature which are variants of these generic classes [99, 100], is that they operate in the stable attractor regime i.e after the dynamical transition. In contrast, the SubPB mechanism we proposed, is based on the organization before the SN_{PB} of the sub-critical *PB* and therefore utilizes a meta-stable state for signal processing.

3.6 Comparison of response features between polarity models

In order to probe how different dynamical mechanisms for polarization manifest their features in sensing, we subjected each of the models, including SubPB mechanism, to a set of stimulation protocols. These standard protocols were designed to quantitatively compare features of polarization and information processing (session in introduction) that are required for optimal navigation in changing environments. A cell (like neutrophil in Figure 1.1A), while executing a long-range migration, encounters spatial gradients of signals and these gradients change their direction (e.g. switching its direction entirely to opposite localization). Sometimes they are also posed with simultaneous, conflicting gradients and they need to resolve between those signals in real-time. The mechanism that underlies sensing in these cells should enable processing information from such dynamic environments in an optimal way. Therefore, responses of all the models under these scenarios were separately captured and were quantified for comparison.

3.6.1 Comparison of polarization features

To investigate the polarization features associated with the respective polarization mechanisms, we quantified for each of these models, their capability to sense shallow and steep gradients, as well as the time required for polarization. In this setting, a cell is posed to a gradient that extends throughout its length (Figure 3.12A, top). Simulations were done by assuming that the cell membrane contour is a one-dimensional domain with no-flux boundary conditions. This enables a simplistic representation of the stimulation scenario where an external linear gradient of stimulus causes polarization in response protein u across the cell from left to right (Figure 3.12A, bottom). The steepness of the gradient, which varies depending on the strength of the source or the relative position of the cell from the source, is quantified using percentage difference (PD %, Figure 3.12A) given by, $PD = (s_{left} - s_{right}) * 100$. Higher PD indicates higher steepness of gradient. In the presence of a gradient, the extend of polarization response is quantified using polarization ratio (PR) which is the ratio between the response amplitude at the left and rightmost location ($PR = \dfrac{u_{left}}{u_{right}}$). For each model 5 independent realizations were performed. The summary of the quantification in Figure 3.12B shows that both LEGI- (magenta) and Turing-type (green) models do not
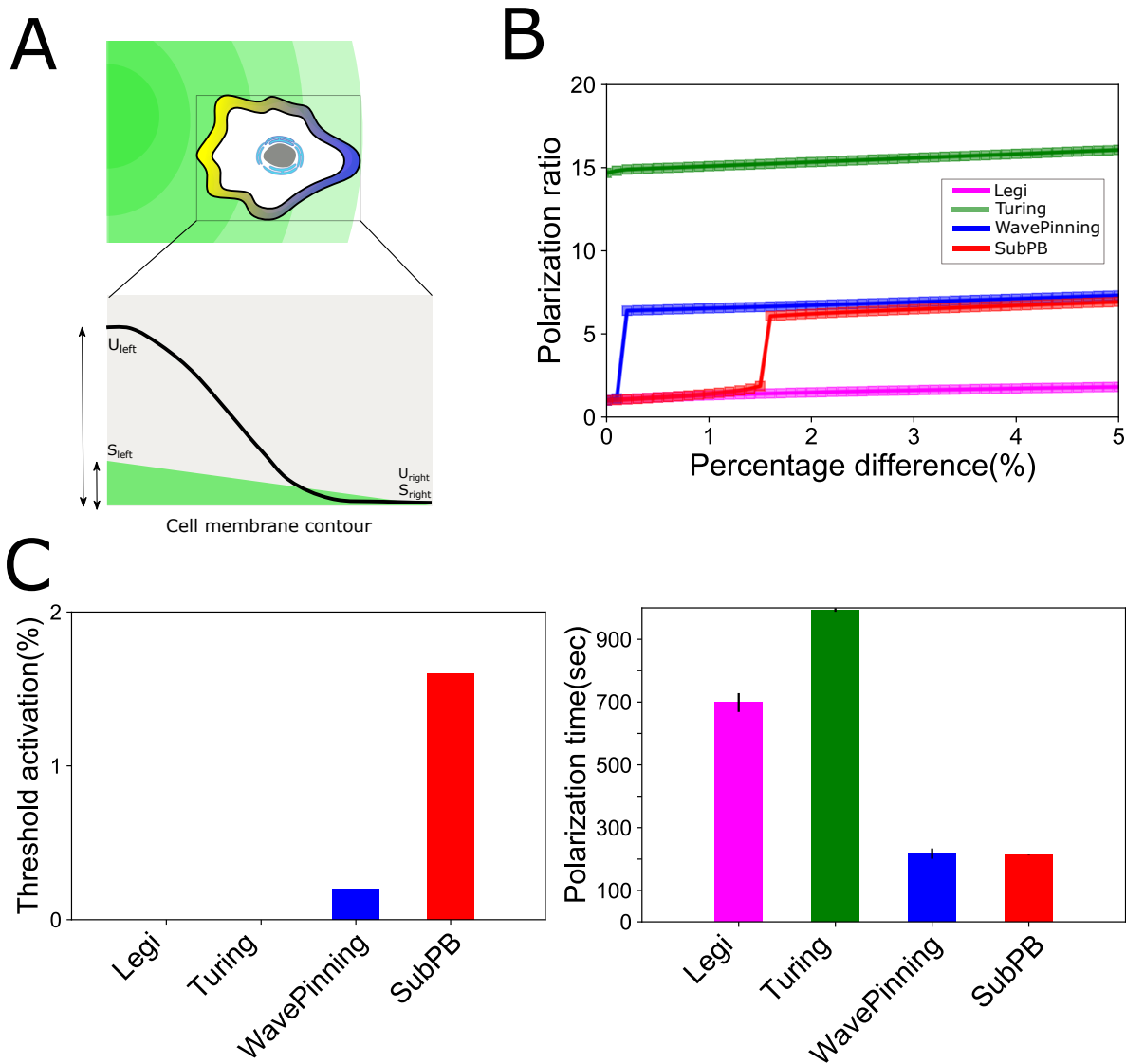
Figure 3.12 Comparison of polarization features between different dynamical mechanisms upon gradient stimulation. A, Schematic of gradient stimulus protocol and polarization response u across cell membrane contour. B, Polarization ratio ($PR = \frac{u_{left}}{u_{right}}$) as a function of gradient percentage difference ($PD = (s_{left} - s_{right}) * 100$). In B,C, magenta: LEGI-; green: Turing-; blue: Wave pinning (WP)- and red: SubPB- type model. C, left: Quantification of the threshold PD leading to stable polarization. right: Quantification of polarization time corresponding to threshold PD. For LEGI- and Turing-type minimal non-zero PD is chosen ($PD = 0.1\%$). Mean $\pm$ s.d from 5 independent RD realizations of the respective system are shown.

require a threshold gradient steepness for activation and LEGI-type exhibits the lowest polarization ratio. The WP-type (blue), effectively generates a robust polarization

response with moderate levels of polarization ratio, however in this case random polarization could be achieved even for low gradient steepness indicating susceptibility to spurious activation under noisy conditions. SubPB mechanism (red), on the other hand with a similar polarization ratio of WP-type, however exhibited a higher threshold for activation and is more robust to spurious activation. We also quantified for each of the models what is the minimal PD % for which stable polarization could be achieved. The quantification in Figure 3.12C shows that WP-type leads to polarization even for relatively lower gradient steepness (PD=0.2 %), suggesting that LEGI-, Turing-, and the WP-type models are not robust to noise. This in turn also implies that a unique description of the un-polarized state in absence of external signal cannot be provided within the framework of these models.

The identified polarization features can be attributed to the underlying dynamical mechanisms in each of the three models. As the LEGI-type model is characterized by a single steady-state, external signal or any variation or noise will induce a change in the geometry of the phase space, triggering a continuous and reversible re-positioning of the single steady-state attractor. Thus near-linear relationship exists between polarization ratio and gradient steepness. This shift of the steady-state position does not allow for amplification of the external signal, thereby generating only negligible polarization ratios.

In the Turing-type model, on the other hand, the existence of the TC bifurcation provides a "soft" transition from the homogeneous steady state describing the un-polarized to the symmetry-broken state describing the polarized state. Since the system organization is in the stable symmetry-broken state (after the TC), such that small variations around the un-stable homogeneous steady-state will switch the system to the stable polarized state, rendering the system not robust to noise. In the WP-type, the existing dynamical transition is "hard" and would enable a threshold activation and thereby is not susceptible to low-intensity noise perturbations. However, as shown in Figure 3.12C, the activation occurs with higher noise intensity.

The SubPB mechanism has a higher threshold of activation (PD=1.6 %) when compared to other mechanisms (Figure 3.12C) and thereby has the robustness to noisy signals with a larger range of amplitudes. Time taken for achieving stable polarization at respective threshold values (for LEGI- and Turing-type PD=0.1 % is chosen) shows that both WP-type and SubPB mechanism enables faster polarization (within 150 sec) when compared with LEGI- and Turing-types (Figure 3.12C, right).
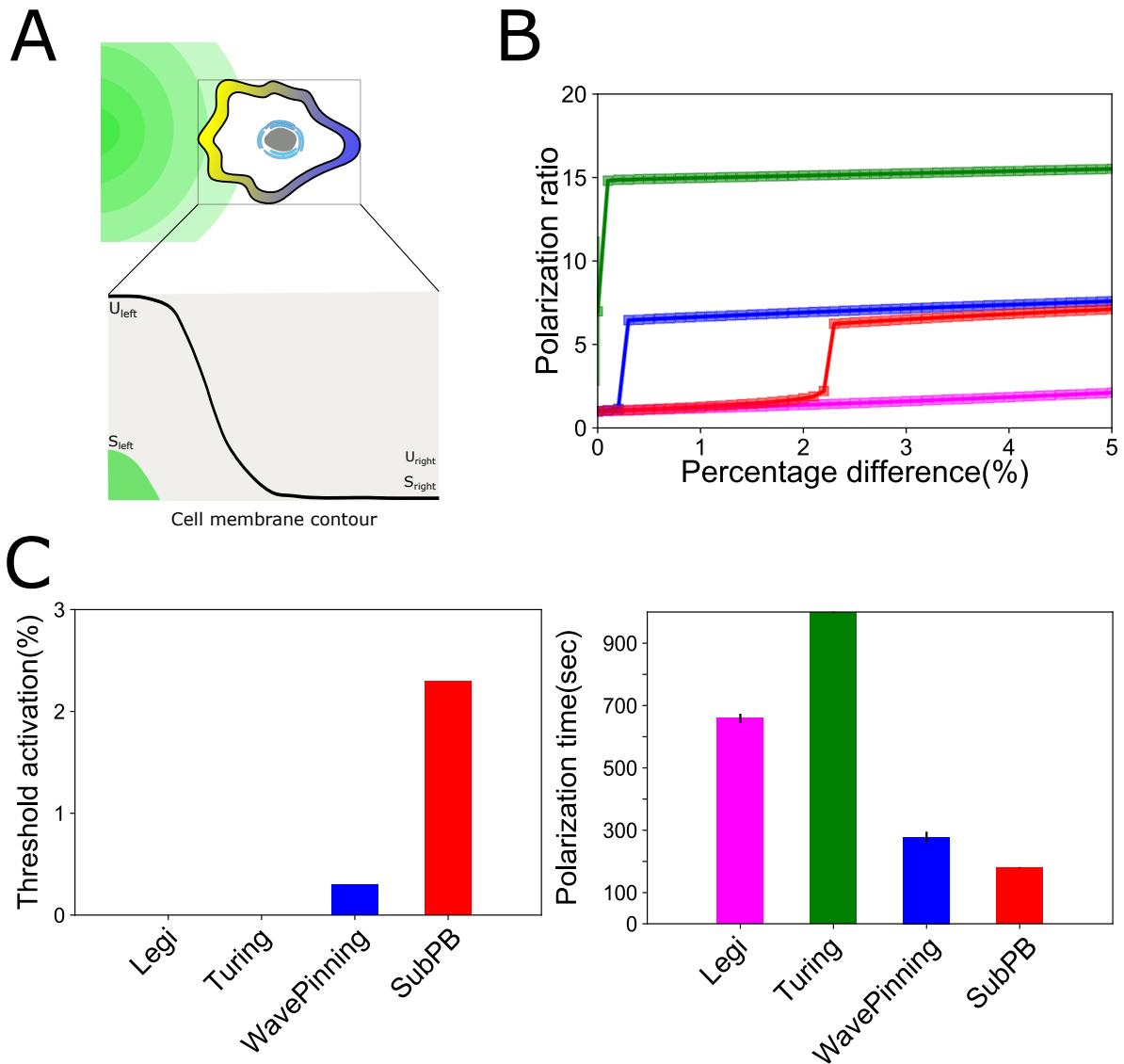
Figure 3.13 Comparison of polarization features between different dynamical mechanisms upon localized gradient stimulation. A, Schematic of localized stimulus protocol and polarization response u across cell membrane contour. B, Polarization ratio as a function of gradient percentage difference (PD). C, left: Quantification of the threshold PD leading to stable polarization. right: Quantification of polarization time corresponding to threshold PD. For LEGI- and Turing-type minimal non-zero PD is chosen ($PD = 0.1\%$). In B,C colour same as in Figure 3.12. Mean $\pm$ s.d from 5 independent RD realizations of the respective system are shown.

Other than spatial gradients, cells are also posed with localized gradient signals whose spatial extent is less than the size of the cell. In order to test how these spatial profiles of the stimulus affect polarization and hence directional sensing, we stimulated cells

with signals that are localized within 10 % of the cell size (Figure 3.13A). The signal is similar to a gradient signal, but here not linear.

Nevertheless, similar to spatial gradient simulation, by varying the localized signal amplitude, a dose-response simulation is performed and the results are quantified in the same way. They suggest that qualitative features of each model remained the same as in the gradient stimulus case in Figure 3.13. While both LEGI- and Turing-type lacked thresholds for activation, SubPB mechanism showed the highest threshold for activation and is the quickest to achieve stable polarization (Figure 3.13 B and C). However, the gradient steepness required for activation has increased (from PD=1.6 % in gradient stimulation to PD=2.3 % in localized gradient). This means that when a gradient with a steepness 1.6 % polarize the cell, a localized gradient stimulus with the same PD cannot. A similar increase is also present for WP-type (from PD=0.1 % in gradient stimulation to PD=0.2% in localized gradient stimulation). This suggests that the spatial profile of the stimulus could affect the extent of the unfolding of the *PB*, hence the threshold for activation.

Since the threshold for activation with a localized gradient signal is higher than or equal to the threshold for activation with a gradient signal, for further analysis stimulus amplitude is set to the threshold for activation corresponding to localized gradient stimulation.

3.6.2 Comparison of information processing features

In response to a spatial gradient, when cells polarize in the direction of the source they are translating the information about signal source localization onto their membrane-bound protein activity state. However, stimulus patterns outside could change over time. The polarized state should be flexible to account for these changes and to continuously adapt to those changes. As shown in Figure 3.8, the SubPB mechanism displays sensitivity to dynamic signals, generates memory of previous signal localization as well as retains responsiveness to subsequent spatially disperse signals, and therefore provides a mechanism that describes history-dependent cellular responses. To compare these features between all four models, the polarization responses are quantified by subjecting the cells to more complex stimulation protocols.

First, we looked at how cell adapt to changes in gradient localization, specifically once the direction of the initial gradient is flipped 180° (Figure 3.14A). For each of the models, initial gradient steepness was chosen from threshold value associated

with localized gradient stimulus dose-response, and time taken for achieving stable polarization at those threshold values was chosen as the duration (Figure 3.14 C, left and right respectively). At the end of the first gradient, the direction is instantly flipped to the opposite direction, and plasticity in response is measured using polarization amplification (PA), which is the ratio of amplitudes at the right-side (u_{right}) after the reversed polarization profile is stable to the amplitude at the left-side (u_{left}) at the time of reversal (Figure 3.14A, bottom), given by PA=$\frac{u_{right}}{u_{left}}$. Thus a proper reversal of polarization corresponds to PA ≥ 1. Polarization amplification is measured as a function of stimulus ratio, $\Delta = \frac{s_{left}}{s_{right}}$ and the amplitude of reversed gradient is varied from $s_{right} = s_{left}$ ($\Delta = 1$) to $s_{right} = 2s_{left}$ ($\Delta = 2$) (Figure 3.14B).

The results show that both LEGI-type and SubPB can reverse their direction of polarization in response to the reversed gradient while WP- and Turing-types didn't allow for it. For WP- and Turing-type, their organization in the stable symmetry broken region causes stable polarization in the direction of the first gradient, remains locked in that state, and becomes insensitive to further temporal or spatial variation of the gradient. Even though LEGI-type enables re-polarization, it requires a larger time for achieving stable reverse polarization. For instance, at $\Delta = 2$ LEGI-type requires > 500 sec to achieve a stable reversed polarization profile suggesting that it cannot account for the rapid responsiveness under physiological conditions when compared with SubPB mechanism that re-polarizes within 100 sec. This together with a lower polarization ratio in comparison with SubPB suggests that the lack of a proper symmetry breaking mechanism slows down the re-polarization capability of LEGI-type models. The SubPB mechanism enables rapid re-polarization to spatially inverted gradient signals and this rapid responsiveness results from the unique topological phase space changes: upon initial gradient signal removal, the system reverts to the stable homogeneous state by transiting through the "ghost" state (Figure 3.3B). Since this state is only meta-stable, the system can be easily re-triggered by the upcoming signal, resulting in rapid re-polarization in the direction of the novel stimulus.

Next, signal resolving capability is tested by presenting the cell with two simultaneous, but distinctly localized signals, each of them occupying 10 % of the cell size from opposite ends, with different amplitudes (Figure 3.15A). As before, polarization amplification is measured as a function of stimulus ratio. After stimulation, simulation is continued till stable polarization is achieved and then polarization amplification is estimated from the response at both sides (u_{left} and u_{right}). All the models can resolve conflicting signals when $\Delta > 1$ with varying extend of resolved polarization

A

B

C
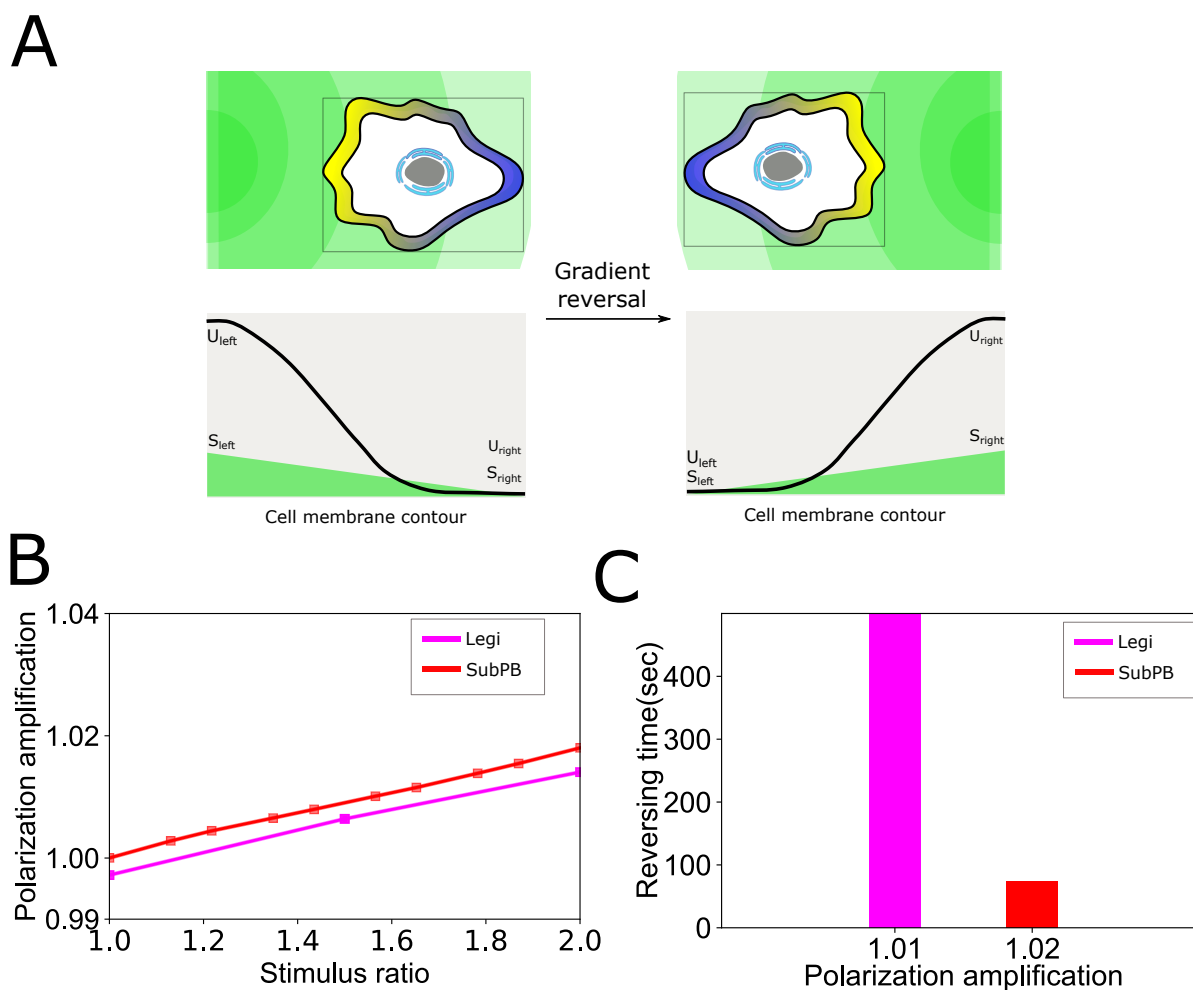
Figure 3.14 Comparison of information processing features between different dynamical mechanisms upon rapid gradient reversal. A, Schematic of gradient reversal protocol and reversal of polarization response *u* across cell membrane contour. B, Polarization amplification as a function of stimulus ratio. C, Time for reversal and corresponding polarization amplification at stimulus ratio 2. Mean $\pm$ s.d from 5 independent RD realizations of the respective system are shown. Colour same as in Figure3.12.

response (Figure 3.15B). However, only WP-type and SubPB mechanisms resolved the presented stimuli rapidly and polarized in the direction of the stronger signal which is evident from the quantification of time taken for resolving at $\Delta = 2$ (Figure 3.15C). LEGI- and Turing-types require > 900 sec to achieve signal resolving.

We next tested whether the models can account for memory in polarization, and thereby retain information about recent signal localization, as demonstrated for the SubPB mechanism in Figure 3.4. The cell was subjected to a pulsed localized stimulus at one
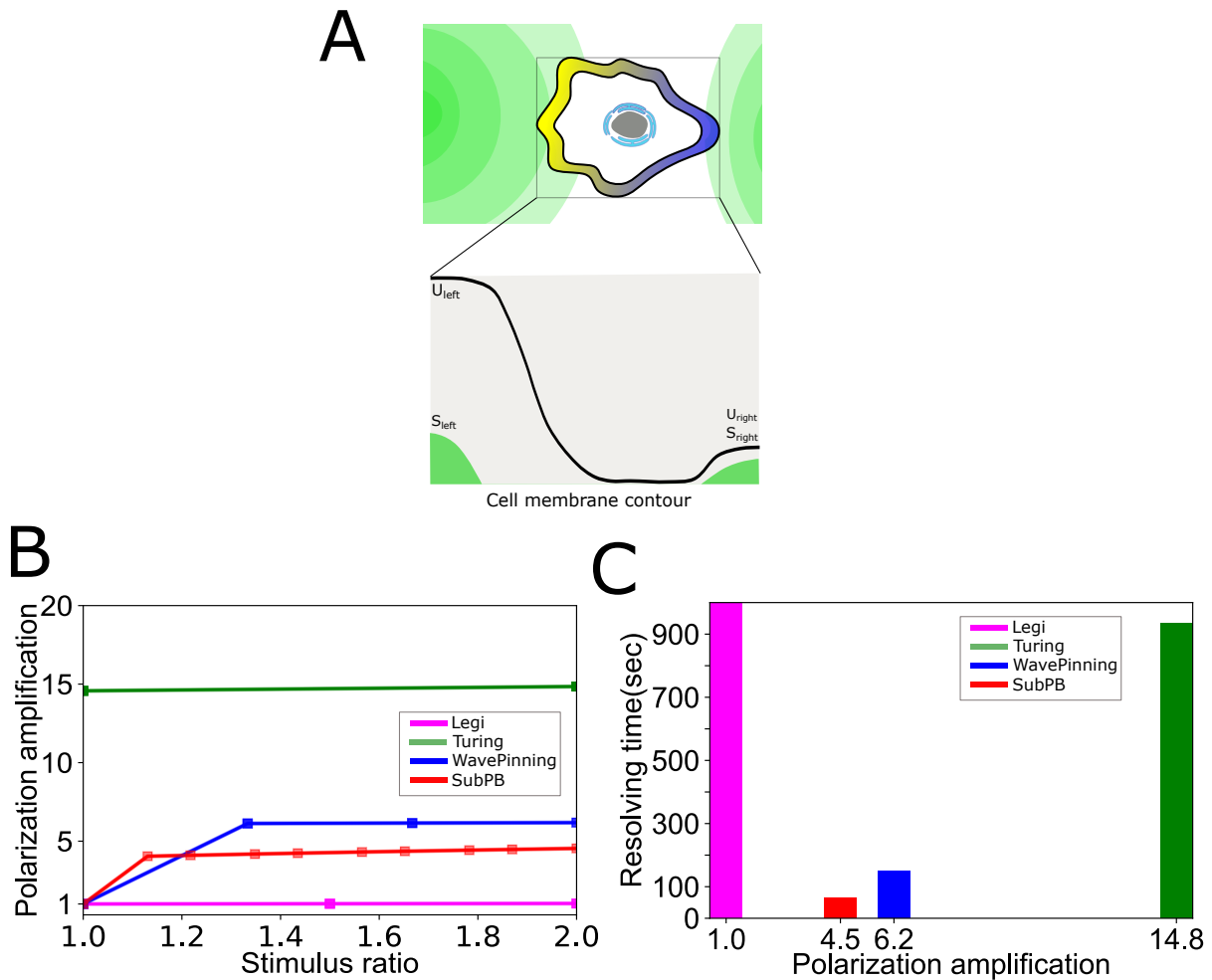
Figure 3.15 Comparison of information processing features between different dynamical mechanisms upon rapid gradient reversal. A, Schematic of simultaneous stimuli protocol and resolving polarization response *u* across cell membrane contour. B, Polarization amplification as a function of stimulus ratio. C, Time for resolving and corresponding polarization amplification at stimulus ratio = 2. Mean ± s.d from 5 independent RD realizations of the respective system are shown. Colour same as in Figure3.12.

side and the temporal evolution of response at that location was examined for each model. The activity profiles demonstrate that only the SubPB mechanism showed a transient memory after the stimulus removal (Figure 3.16A, top). Both WP- and Turing-type display permanent memory of previous signal localization by continuously maintaining the polarized state after the signal removal (Figure 3.16B, C top). The LEGI-type model displays a monotonous increase of response in signal presence and rapidly decaying after signal removal exponentially (Figure 3.16D, top).

As previously mentioned, the transient memory exhibited by the SubPB mechanism results from the "ghost" saddle node that is generated upon removal of the signal. It has been previously demonstrated that maintenance of receptor activity via such a meta-stable state provides an advantage over a simple exponential decay, displayed by LEGI-type, as it enables to avoid a trade-off between history-dependent signal integration and adaptation to the temporal partitioning of complex signals [35]. This can be illustrated by subjecting the cells with a subsequent pulsed localized signal from the same direction. The cellular responsiveness to a second stimulus is retained within the SubPB model and the polarization state is subsequently adapted depending on the signal sequence, thereby demonstrating signal-integration capabilities (Figure 3.16A, middle). Due to the permanent memory of the polarized state established within the WP- and Turing-type models after the initial signal, sensing of the subsequent signal is completely hindered (Figure 3.16B, C middle). While for LEGI-type, the polarization response directly follows the signal addition, and thereby signal-integration cannot be achieved (Figure 3.16D middle).

In summary, the reduced state-space description corresponding to different mechanisms (Figure 3.16, third row) captures the plasticity of their polarization responses. In the SubPB mechanism, a metastable state (triangle) in which the memory of the polarized state is maintained enables switching to the polarized state (square) or unpolarized state (circle) depending on the temporal behavior of the external signal. In WP- and Turing-type this temporal variation of the signal is not significant because of the permanent memory that is endowed by the polarized state. Lack of such a memory in LEGI-type on the other hand only allows for response to follow the signal profile.

3.6.3   Metastability of SubPB mechanism renders optimal response features

Optimal response features of the SubPB mechanism stems from the unification of properties of two distinct bifurcations: *PB* that enables rapid and robust polarization and *SN$_{PB}$*s with plasticity in that response. This unification is a direct consequence of organization at criticality. The shallow slope of the potential landscape at this critical organization causes a prolonged transition period from activated to the basal state where this flexible transient state retains information of recent encounter with a signal source without compromising the sensitivity to novel stimuli (Figs. 3.4, 3.16A). The presence of a permanent memory state as in the case of WP- or Turing-type or lack of a memory state as in the case of LEGI- type leads to loss of responsiveness or signal
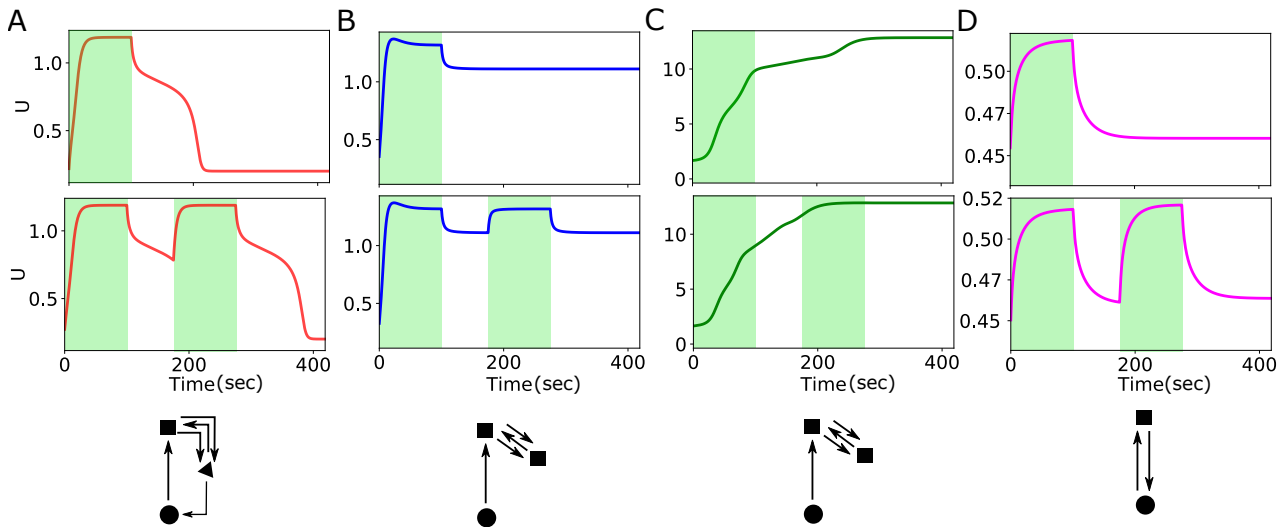
Figure 3.16 Transient memory state in SubPB mechanism enables signal integration.
A, top: Temporal polarization response of SubPB mechanism at the stimulus side upon a pulsed localized gradient stimulus (green shade). Middle: Same as in top, but for response to subsequent signals with equivalent localization. Bottom: Reduced state representation corresponding to response to subsequent signals. Circle: basal-, square: polarized-, triangle: memory- state. Arrows: transitions. B,C,D same as in A but for WP-, Turing-, and LEGI-type.

integration capabilities or both. The parameter organization of WP-type is equivalent to the organization in Region II of sub-critical pitchfork bifurcation in which the stable inhomogeneous state represents the polarized state. This stable attractor endows a long-term memory to polarized response and hence locks it in a continuously activated state (Figs. 3.5C, 3.16B). In Turing-type, even though a distinct mechanism causes symmetry breaking, again a stable state characterizes the polarized state and exhibits a similar permanent memory. In LEGI-type a stable state for polarization does not exist but polarization is achieved through a local activation and this activated state is a monostable state that has a linear dependency towards signal strength. Thus the time spend in this stable attractor, in turn, the time in the polarized state, is equivalent to the administration time of the gradient stimulus. Such a linear dependency results in the absence of prolonged polarization upon gradient removal. So WP-, Turing- and LEGI-types that relies on computations with stable states are less suited for real-time computation of signals that vary in time and space [35] because this canonical view of cellular computations based on stable attractors fails to account for plasticity in polarization response - a ubiquitous feature that can be realized through computation away from steady-state.

These results, therefore, demonstrate that the SubPB mechanism proposed here uniquely enables sensing and responsiveness to dynamic signals, as a result of the critical organization that enables utilization of a meta-stable state to adapt to dynamic signals in the environment. This mechanism provides robust maintenance of the polarized state after signal removal while retaining at the same time responsiveness to upcoming signals, as well as the capability to resolve multiple simultaneous signals, and thereby represents a unique mechanism for history-dependent responsiveness of cells.

3.7 Viscoelastic description of the cell captures shape changes during cell motility

Cell shape changes are a ubiquitous part of directed cell motility. It involves multiple interrelated processes. The first level is signal sensing and it happens at the level of cell surface receptor proteins. In the presence of gradient signal, the information of this asymmetry in the surrounding will be translated as a polarized response on the membrane as we have demonstrated before. Then this response is transmitted from the sensing modules to the machinery that executes the actual movement, which is the cytoskeleton by actin and microtubules [101, 102]. The polarized cytoskeletal machinery then generates asymmetric forces within the cell and enables subsequent migration. The change in geometry of the cell membrane associated with the shape change can in turn affect the signaling activity, rendering cellular navigation a complex scenario to deal with [103]. In a simplistic description, we can summarize that a polarized receptor protein activity at the membrane causes polarized cell shape response. Different approaches exist to model cellular shape changes as a function of receptor activity. For this, in addition to the physical properties of the cell membrane, molecular details of polarization to shape change are required. One of the initial steps after protein activity polarization is regulation of downstream small Rho GTPases activity that affects reorganization of actin and myosin. It is known that cell surface receptors such as RTKs, G-protein coupled receptors can regulate Ras, Rac, Cdc42, RhoA, and other downstream proteins, which in turn can control dynamic changes in actin and myosin [104, 105]. In an un-polarized cell, actin and myosin constitute a cortex in the vicinity of the plasma membrane. In the presence of a gradient of signal, cellular motility results from the coordination of leading-edge protrusion and cell-body contraction together with the detachment from sites at the rear. Actin polymerization

at the leading edge and myosin enabled contraction at the trailing edge result from the polarized intracellular response of the small Rho GTPases which are actuated by cell surface receptor activity. This spatially and temporally coordinated activity thereby induces signal-dependent cell shape changes and migration [106–108].

In order to link receptor signaling activity with morphodynamics, we modeled the cell as a viscoelastic cortex surrounding a viscous core, where receptor signaling dynamics affect cell shape changes. To couple a mechanical model of the cell with the receptor polarization mechanism as a means to simulate global cellular deformations, we utilized the Level Set Method (LSM) as described in [109]. In this formalism, the cell boundary at time t is described on a two-dimensional Cartesian grid by the closed-contour $\Gamma(t) = \{\mathbf{x}|\Psi(\mathbf{x},t) = 0\}$, that represent the zero-level set of the potential function $\Psi(\mathbf{x},t)$ (Figure 3.17A), taken to have an initial form:

$$\Psi(\mathbf{x},0) = \begin{cases} -d(\mathbf{x},\Gamma), & \text{if } \mathbf{x} \in S \\ d(\mathbf{x},\Gamma), & \text{if } \mathbf{x} \notin S \\ 0, & \text{if } \mathbf{x} \in \Gamma \end{cases} \tag{3.22}$$

where S identifies the initial area occupied by the cell and $d(\mathbf{x}, \Gamma)$ is the distance of position $\mathbf{x}$ to the curve Γ. Thus, the cell membrane is represented implicitly through the potential function which is defined on the fixed Cartesian grid, eliminating the need to parameterize the boundary, and thereby enabling to handle of complex cell boundary geometries.

The shape of the cell ($\Gamma(\mathbf{x},t)$) evolves according to the Hamilton-Jacobi equation:

$$\frac{\partial \Psi(\mathbf{x},t)}{\partial t} + \mathbf{v}(\mathbf{x},t) \cdot \nabla \Psi(\mathbf{x},t) = 0 \tag{3.23}$$

The vector $\mathbf{v}(\mathbf{x},t)$ is the velocity of the level set moving in the outward direction, thereby intrinsically describing the cell's membrane protrusion and retraction velocities that are driven by internally generated mechanical forces from actin polymerization or myosin-II retraction (Figure 3.17B, black arrows). However, these forces do not translate directly into local membrane velocities. The viscoelastic nature of the interaction between the cell membrane and cortex also affects the effective local membrane velocities. Thus, a mechanical model that describes the viscoelastic behavior of the cell represented as a viscoelastic cortex needs to be implemented. Following [109],

the cortex connecting the cell membrane and the cytoplasm is represented by a Voigt-dashpot model (Figure 3.17B, a gray rectangular unit that connects cytoplasm and membrane). This model consists of a parallel connection of an elastic element k_c and a viscous element τ_a (Voigt unit) and this unit is connected in series with cytoplasm which is modeled as a purely viscous element (dashpot unit, τ_c)

A

B
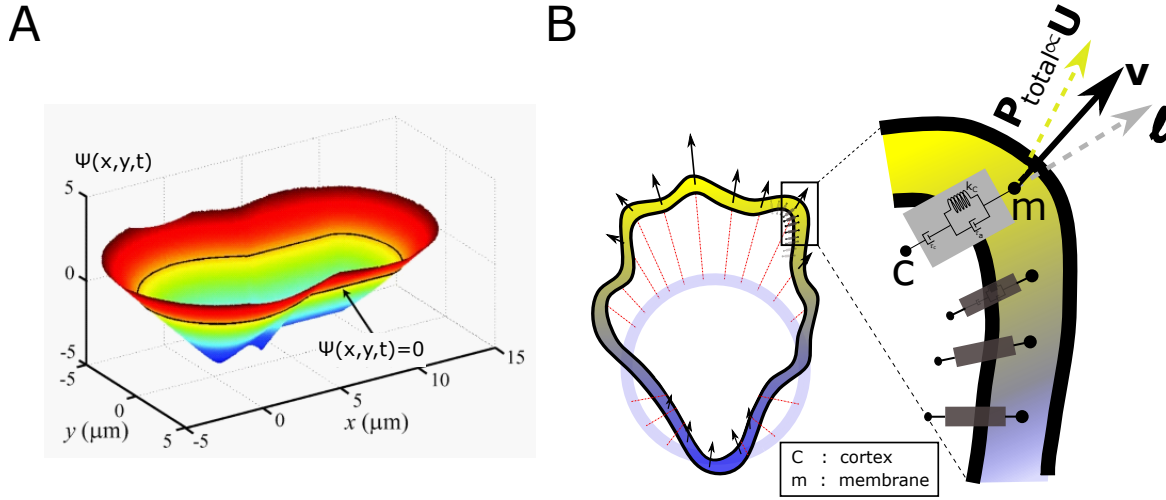
Figure 3.17 Physical model of single cell chemotaxis and shape change using level set method (LSM). A, Representation of a level set potential $\psi(x,y)$ given by the Euclidean distance to the cell boundary with positive (negative) sign when outside (inside) the cell. Black contour is level set zero ($\psi(x,y) = 0$). Scheme reprinted from [109]. B, Signal induced shape changes during cell polarization. Arrows: local edge velocity direction. Zoom: Viscoelastic model of the cell- parallel connection of an elastic and a viscous element. P_{total}: total pressure; **v**: local membrane velocity; **l**: viscoelastic state. Bold letters: vectors. Cell membrane contour: $[0, 2\pi]$.

Let $\mathbf{l}(\mathbf{x},t)$, $\mathbf{x} \in \Gamma(t)$ be the viscoelastic state of the cell at time t and at a position $\mathbf{x}$ on the membrane, such that $|\mathbf{l}|$ represents the length of the numerous parallel unconnected spring-damper systems. The viscoelastic state of the cell then evolves according to:

$$\frac{\partial \mathbf{l}(t)}{\partial t} + \nabla \mathbf{l} \cdot \mathbf{v(t)} = \frac{-k_c}{\tau_c}\mathbf{l}(t) + \frac{1}{\tau_c}\mathbf{P_{total}}(t) \qquad (3.24)$$

where ∇ is the gradient operator, the pressure $\mathbf{P_{total}}(t) = \mathbf{P_{prot}}(t) + \mathbf{P_{retr}}(t) + \mathbf{P_{area}}(t) - \mathbf{P_{ten}}(t)$ is sum of the protrusion, retraction, area conservation, and cortical tension pressures, respectively. The receptor signaling state ($u(x,t)$) directly determines the protrusion/retraction pressure, since high/low signaling activity triggers actin polymer-

ization / myosin-II retraction following:

$\mathbf{P_{prot}}(t) = K_{prot} \dfrac{u - <u>}{u_{max} - <u>} \mathbf{n}$ and $\mathbf{P_{ret}}(t) = -K_{retr} \dfrac{<u> - u}{<u> - u_{max}} \mathbf{n}$, where $<.>$ de-
notes mean at the membrane, K_{prot}, K_{retr} - proportionality constants, $\mathbf{n}$- direction of normal vector at the membrane. The cell is assumed to be flat with uniform thickness, such that the 2D area $(A(t))$ of the cell is conserved. A pressure is implemented to check this conservation and is given by $\mathbf{P_{area}(t)} = K_{area}(A(0) - A(t))\mathbf{n}$, K_{area} - proportionality constant. The pressure generated by the cortical tension therefore depends only on the 2D local surface curvature and the 2D equilibrium pressure, rendering the rounding pressure due to cortical tension to be $\mathbf{P_{ten}}(t) = K_{ten}(\kappa(\Gamma) - 1/R)\mathbf{n}$, with $\kappa(x)$ being the local membrane curvature, R - initial cell radius, and K_{ten} - proportionality constant. At every instant, the local membrane velocity $\mathbf{v}(\mathbf{x})$, $\mathbf{x} \in \Gamma(t)$ depends both on the viscoelastic nature of the cell and on the effective pressure profile $(\mathbf{P_{total}}(t))$ and is given by,

$$\mathbf{v} = \frac{-k_c}{\tau_c}\mathbf{l} + (\frac{1}{\tau_c} + \frac{1}{\tau_a})\mathbf{P_{total}} \qquad (3.25)$$

For the numerical simulation, the spatial discretization of these advection equations (Eqs.(3.24),(3.25)) was performed using the *upwindENO2* scheme, as described in the Level Set Toolbox [110] and was integrated with first order forward Euler method. The time step was set to $0.01min$ and the potential function was solved on a 2D Cartesian grid with spatial discretization of 5 points per μm. Parameters used were: $k_c = 0.1 \quad nN/\mu m^3$, $\tau_c = 0.08 \quad nNmin/\mu m^3$, $\tau_a = 0.1 \quad nNmin/\mu m^3$, $K_{prot} = 0.08 \quad nN/\mu m^2$, $K_{retr} = 0.05 \quad nN/\mu m^2$, $K_{area} = 0.02 \quad nN/\mu m^4$, $K_{ten} = 0.1 \quad nN/\mu m$. K_{ten} was taken from the literature, corresponding to an experimentally measured range of cell cortical tension values [111].

In Figure 3.16A, two subsequent localized gradient stimuli from the same direction showed that the SubPB mechanism enables optimal polarization response by storing information in a metastable state. Now the viscoelastic model for capturing morphological changes can be used to link this polarization response to shape changes in order to understand how metastability in polarization response translates into shape change and further into signal integration at the level of morphology. To incorporate the fluctuations in cell shape in the absence of signals, this time stochastic partial differential equations corresponding to each of the models were solved to obtain the kymographs of u activity which then was used as an input to the viscoelastic simulation.
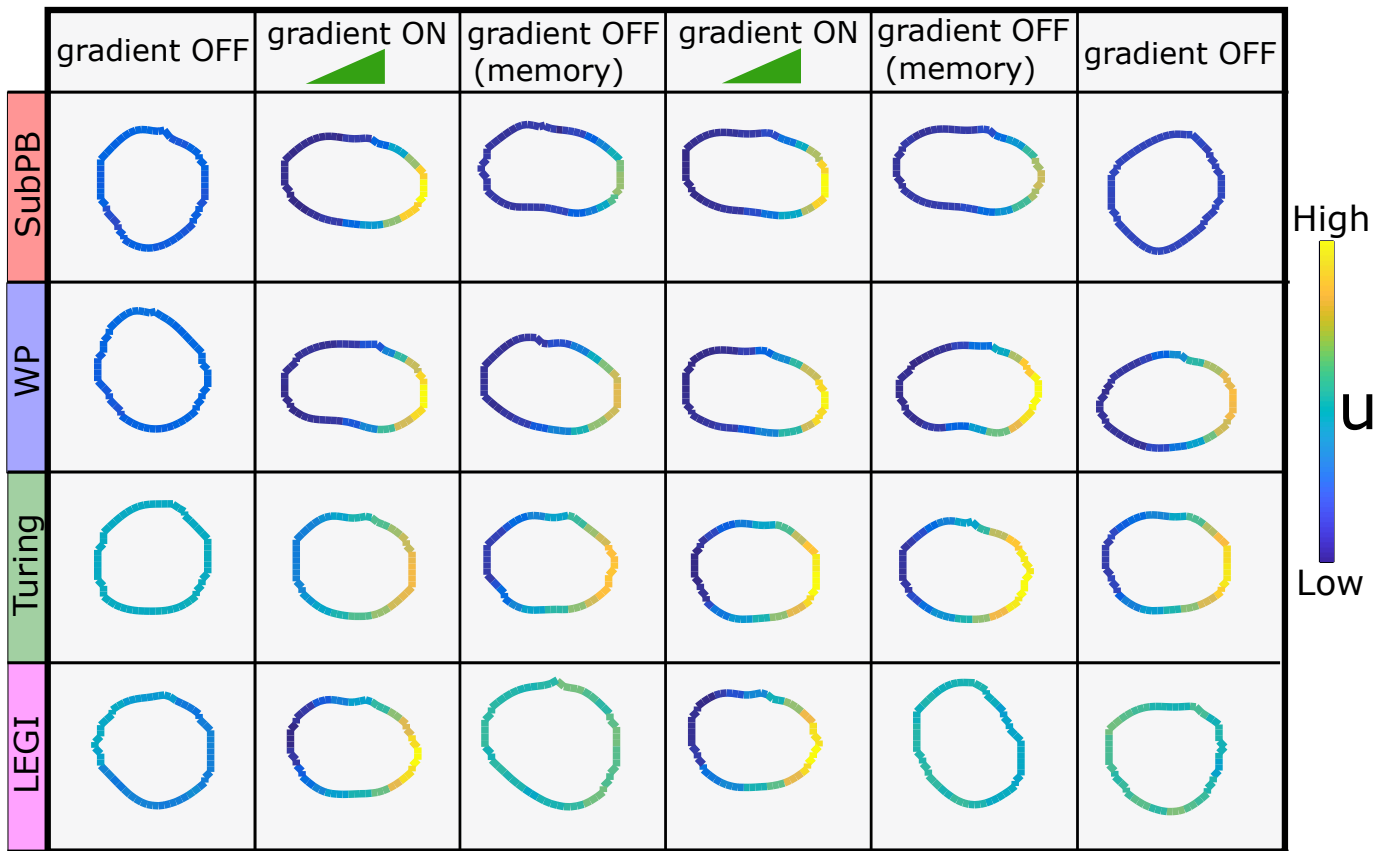
Figure 3.18 Different polarity models responding to subsequent gradient signals from same direction with shape changes. Rows: different polarity models. Columns: Snapshot of cell shape at time points from Figure 3.16 middle row. Cell shapes obtained using model in Figure 3.17B. Color coding: normalized u values from corresponding model and time point. High=1, low=0.

The molecular noise in the system is mimicked by adding a Gaussian white noise to u at each time step.

The tabular summary in Figure 3.18 shows cell shapes at distinct time points corresponding to all four mechanisms for comparison. The distinct time points were chosen to show how cell shape changes depending on the presence or absence of gradient (columns from left to right: before the first gradient, during the first gradient, during the memory of the first gradient, during the second gradient, during the memory of the second gradient and after the memory of the second gradient). For all the four models, the cell is initiated as a circle with radius, $R_0 = 2\mu m$. Snapshots of the shape (Figure 3.18, column 1) during the absence of the gradient shows fluctuating boundary due to the noise in receptor activity. The sequence of morphological changes for

the SubPB mechanism (row 1) shows the transition from this un-polarized shape to a polarized shape during the first gradient (row 1- column 2). Overlay of protein activity on the membrane contour shows that the asymmetric elongated shape of the cell results from the polarized protein activity. After the gradient is gone (row 1 - column 3), the memory of this polarized activity causes the polarized shape to be retained until the second gradient. Similar to the memory state in the activity (Figure 3.16, top panels), this memory of polarized shape does not hinder responsiveness to the second gradient (row 1 - column 4). The cell shape during the second gradient is further retained after the gradient removal (row 1 - column 5) and eventually goes back to an un-polarized shape (row 1 - column 6) similar to the initial state. The signal integration at the level of protein activity is reflected at the level shape changes because of the presence of a transient memory of polarized shape. This suggests that metastability in signaling response enables optimal shape changes during navigation as well. A similar shape change in WP- (row 2) and Turing-type (row 3) shows that once the cell achieves a polarized shape during the first gradient, that shape is maintained irrespective of temporal variation in gradient field endowing a permanent memory. In LEGI- type (row 4) the reversible changes between un-polarized to polarized shapes happen as a function of the gradient signal. These transitions leave no memory state equivalent to the polarization response hence do not allow for signal integration and hinder continuous migration over a long range.

The theoretical results suggest that the SubPB mechanism endows biochemical networks with features that enable robust polarization and information processing not only at the level of protein activity but also at the level of cell morphology during motility. Computations using stable attractors leave other known mechanisms less suitable for real-time information processing.

3.8 SubPB mechanism underlies Epidermal growth factor sensing in epithelial cells

To test the proposed mechanism experimentally, we used the well-characterized EGFR sensing network [1] that was discussed in section 1.5. EGFR response to time-varying uniform pulse of EGF has revealed that the network has an organization in the vicinity of a *SN*. In order to test the network's response to spatial EGF cues, we extended the model to have spatial dimensions by considering the diffusivity of the components (A. Das (2022), doctoral dissertation).

3.8.1   Polarization in EGFR phosphorylation response has transient memory due to metastability
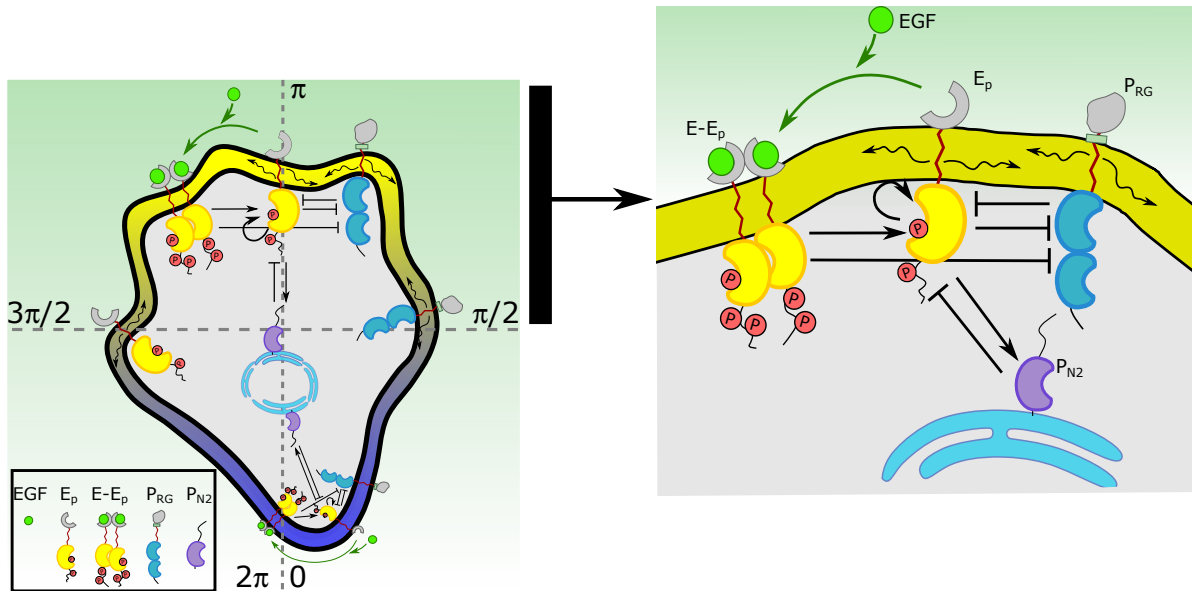
Figure 3.19 Scheme of the spatially distributed EGFR-PTP interaction network. Ligandless EGFR (E_p) interacts with PTPRG (P_{RG}) and PTPN2 (P_{N2}). Liganded EGFR ($E - E_p$) promotes autocatalysis of E_p. Solid black lines: causal links; wiggly arrows: diffusion. Zoom: Upper half of the cell for clarity.

The experimentally identified spatially extended Epidermal growth factor sensing network [21, 25, 1] constitutes of double negative and negative feedback interactions of ligandless EGFR (E_p) with two enzymes, the phosphatases PTPRG (P_{RG}) and PTPN2 (P_{N2}), respectively (Figure 3.19). E_p and P_{RG} laterally diffuse on the membrane (wiggly arrows) and inhibit each other. The negative feedback between the non-diffusing P_{N2} and E_p is established through spatial recycling of E_p. These molecular interactions can be mathematically described using mass action kinetics and are given by the following one-dimensional system of partial differential equations (PDEs):

$$\frac{\partial [E_p]}{\partial t} = f_1([E_p], [E-E_p], [RG_a], [N2_a], [EGF_t]) + D_{E_p}\frac{\partial^2 [E_p]}{\partial x^2}$$

$$\frac{\partial [E-E_p]}{\partial t} = f_2([E_p], [E-E_p], [EGF_t]) + D_{E-E_p}\frac{\partial^2 [E-E_p]}{\partial x^2}$$

$$\frac{\partial [RG_a]}{\partial t} = f_3([E_p], [E-E_p], [RG_a]) + D_{RG_a}\frac{\partial^2 [RG_a]}{\partial x^2} \qquad (3.26)$$

$$\frac{\partial [N2_a]}{\partial t} = f_4([E_p], [E-E_p], [N2_a])$$

with

$$f_1 = ([E_t] - [E_p] - [E-E_p])(\alpha_1([E_t] - [E_p] - [E-E_p]) + \alpha_2[E_p] + \alpha_3[E-E_p]) -$$

$$\gamma_1[RG_a][E_p] - \gamma_2[N2_a][E_p] - k_{on}([EGF_t] - [E-E_p])[E_p]^2 + 0.5k_{off}[EE_p];$$

$$f_2 = k_{on}([EGF_t] - [E-E_p])([E_p]^2 + ([E_t] - [E_p] - [E-E_p])^2) - k_{off}[E-E_p];$$

$$f_3 = k_1([RG_t] - [RG_a]) - k_2[RG_a] - \beta_1[RG_a]([E_p] + [E-E_p]);$$

and

$$f_4 = \varepsilon(k_1([N2_t] - [N2_a]) - k_2[N2_a] + \beta_2([E_p] + [E-E_p])([N2_t] - [N2_a])).$$

The reaction terms are described in [1]. $[E-E_p]$ is the phosphorylated ligand-bound EGFR, $[E_p]$ - ligandless phosphorylated EGFR, $[E_t]$ - total amount of EGFR, $[RG_a], [RG_t]$ and $[N2_a], [N2_t]$ - the active and total amount of the membrane localized PTPRG and the ER-bound PTPN2, respectively. The parameters in the model Eqs.(3.26) have been described in [1], where they were calibrated with experimental data: $\alpha_1 = 0.001$, $\alpha_2 = 0.3$, $\alpha_3 = 0.7$, $\beta_1 = 11$, $\beta_2 = 1.1$, $k_1 = 0.5$, $k_2 = 0.5$, $g_1 = 1.9$, $g_2 = 0.1$, $k_{on} = 0.05$, $k_{off} = 0.28$, $\varepsilon = 0.01$, $RG_t = 1$, $N2_t = 1$; and the diffusion-like terms have been scaled from the values derived in [112]: $D_{RG_a} = 0.02$, $D_{E_p} = 0.02$.

Both the receiver and the deactivating enzymes have active and inactive states, and the model equations describe their state transition rates. Therefore, mass is conserved in the system and the total protein concentrations of the three species ($[E_t]$, $[RG_t]$ and $[N2_t]$) are constant parameters. Autonomous, autocatalytic, and ligand-bound-induced activation of ligandless EGFR ensue from biomolecular interactions with distinct rate constants α_{1-3}, respectively. Other parameters are as follows: k_1/k_2 — activation/inactivation rate constants of the phosphatases, β_1/β_2 - receptor-induced regulation rate constants of $PTPRG/PTPN2$, γ_1/γ_2 - specific reactivity of the enzymes ($PTPRG/PTPN2$) towards the receptor. The EGFR-PTPN2 negative feedback is on a time scale (ε) approximately two orders of magnitude slower than the phosphorylation-dephosphorylation reaction, as estimated from the $\sim 4min$ recycling time of $EGFR_p$ [1]. This enables, when necessary, to consider a quasi-steady-state approximation for the dynamics of PTPN2 for simplicity:

$$[N2_a]_{qss} = [N2_t] \cdot \frac{(k_1 + \beta_2 \cdot ([E_p] + [E - E_p]))}{k_1 + k_2 + \beta_2 \cdot ([E_p] + [E - E_p])} \tag{3.27}$$

$[EGF_t]$ denotes the total ligand concentration. Assuming that at low, physiologically relevant EGF doses, the ligand will be depleted from the solution due to binding to EGFR [113], ligand-binding unbinding was explicitly modeled (k_{on}, k_{off}) in Eqs.3.26. The diffusion terms model the lateral diffusion of the EGFR and PTPRG molecules on the plasma membrane, whereas PTPN2 is ER-bound and does not diffuse. Single-particle tracking studies have demonstrated that EGFR molecules on the plasma membrane occupy three distinct mobility states, free, confined, and immobile, with the occupations of the free and immobile states decreasing and increasing significantly after EGF stimulation (2 min after EGF stimulation, corresponding with the time-scale of EGF binding) [114]. In the reaction-diffusion (RD) simulations therefore for simplicity, it is assumed that $D_{E-E_p} \approx 0$, whereas diffusion constants of same order are assumed for the ligandless EGFR and PTPRG ($D_{E_p} \sim D_{RG_a}$).

To identify analytically the existence of a SN_{PB} in the EGFR receptor network we performed a weakly nonlinear analysis analogous to section 1.2. For this, we considered the system Eqs.(3.26), where the dynamics of PTPN2 is at quasi-steady state (Eq.(3.27)), $[E - E_p] = 0$, and rest of the dependent and independent variables were scaled to have a dimensionless form. Let $[\tilde{E}_p] = [E_p]/E_0$, $[\tilde{RG}_a] = [RG_a]/RG_0$, $\tilde{x} = x/x_0$, $\tau = t/t_0$, such that $t_0 = 1/(k_1 + k_2)$, $E_0 = k_1/\beta_2$, $RG_0 = (k_1 + k_2)/\gamma_1$ and

$t_0/x_0^2 = 1/D_{E_p}$. Substituting these into Eqs.(3.26) yields the system of dimensionless equations:

$$\frac{\partial [\tilde{E}_p]}{\partial \tau} = q_1 + q_2[\tilde{E}_p] + q_3[\tilde{E}_p]^2 - [R\tilde{G}_a][\tilde{E}_p] - \frac{q_4(1+[\tilde{E}_p])[\tilde{E}_p]}{(1+k+[\tilde{E}_p])} + \frac{\partial^2 [\tilde{E}_p]}{\partial \tilde{x}^2}$$

$$\frac{\partial [R\tilde{G}_a]}{\partial \tau} = r_1 - [R\tilde{G}_a] - r_2[R\tilde{G}_a][\tilde{E}_p] + D\frac{\partial^2 [R\tilde{G}_a]}{\partial \tilde{x}^2} \tag{3.28}$$

with $q_1 = \frac{a_1 \cdot [E_t]^2 \cdot k_3}{(k_1+k_2)\cdot\beta_2}$, $q_2 = \frac{(a_2 - 2 \cdot a_1) \cdot [E_t]}{k_1+k_2}$, $q_3 = \frac{(a_1 - a_2) \cdot k_1}{(k_1+k_2)\cdot\beta_2}$, $q_4 = \frac{\gamma_2 \cdot [N2_t]}{k_1+k_2}$, $k = k_2/k_1$, $r_1 = \frac{k_1 \cdot [RG_t] \cdot \gamma_1}{(k_1+k_2)^2}$, $r_2 = \frac{\beta_1 \cdot k_1}{(k_1+k_2)\cdot\beta_2}$ and $D = \frac{D_{RG_a}}{D_{E_p}}$.

We further simplify the system Eqs.(3.28) by taking the Talyor series expansion of the quasi-steady state approximation of $[N2_a]$ around E_s, the steady state of $[\tilde{E}_p]$:

$$\frac{q_4(1+[\tilde{E}_p])[\tilde{E}_p]}{1+k+[\tilde{E}_p]} = q_7 + q_8[\tilde{E}_p] + q_9[\tilde{E}_p]^2 + o([\tilde{E}_p]^2) \tag{3.29}$$

with $q_7 = \frac{E_s q_4}{1+k+E_s} - \frac{E_s q_4 (1+k)}{(1+k+E_s)^2}$, $q_8 = \frac{E_s q_4}{1+k+E_s} + \frac{q_4(1+k)}{(1+k+E_s)^2}(1-E_s)$ and $q_9 = \frac{q_4(1+k)}{(1+k+E_s)^2}$, thus yielding:

$$\frac{\partial [\tilde{E}_p]}{\partial \tau} = q_9 + q_{10}[\tilde{E}_p] + q_{11}[\tilde{E}_p]^2 - [R\tilde{G}_a][\tilde{E}_p] + \frac{\partial^2 [\tilde{E}_p]}{\partial \tilde{x}^2}$$

$$\frac{\partial [R\tilde{G}_a]}{\partial \tau} = r_1 - [R\tilde{G}_a] - r_2[R\tilde{G}_a][\tilde{E}_p] + D\frac{\partial^2 [R\tilde{G}_a]}{\partial \tilde{x}^2} \tag{3.30}$$

with $q_9 = q_1 - q_7$, $q_{10} = q_2 - q_8$ and $q_{11} = q_3 - q_9$.

To avoid long expression in the further analysis, we re-name the dependent variables as $u_1 = [\tilde{E}_p]$ and $u_2 = [R\tilde{G}_a]$, and the independent variables as $\tilde{x} = x$, $\tau = t$. The system Eqs.(3.28) therefore obtains the generic form:

$$\frac{\partial u_1}{\partial t} = F_1(u_1, u_2) + \frac{\partial^2 u_1}{\partial x^2}$$

$$\frac{\partial u_2}{\partial t} = F_2(u_1, u_2) + D\frac{\partial^2 u_2}{\partial x^2}. \tag{3.31}$$

In order to perform numerical bifurcation analysis and thereby identify the symmetry breaking mechanism, a one-dimensional projection of Eq.(3.31) is considered for simplicity,

$$\frac{du_{1L}}{dt} = F_1(u_{1L}, u_{2L}) - (u_{1L} - u_{1R}) = G_1(u_{1L}, u_{2L}, u_{1R})$$

$$\frac{du_{2L}}{dt} = F_2(u_{1L}, u_{2L}) - D(u_{2L} - u_{2R}) = G_2(u_{1L}, u_{2L}, u_{2R})$$

$$\frac{du_{1R}}{dt} = F_1(u_{1R}, u_{2R}) - (u_{1R} - u_{1L}) = G_3(u_{1R}, u_{2R}, u_{1L}) \tag{3.32}$$

$$\frac{du_{2R}}{dt} = F_2(u_{1R}, u_{2R}) - D(u_{2R} - u_{2L}) = G_4(u_{1R}, u_{2R}, u_{2L})$$

Let, $\mathbf{U_s} = \begin{pmatrix} u_{1Ls} \\ u_{2Ls} \\ u_{1Rs} \\ u_{2Rs} \end{pmatrix}$ be the stable symmetric steady state of the system ($u_{1Ls} = u_{1Rs}$, $u_{2Ls} = u_{2Rs}$). A small amplitude perturbation on this symmetric steady state of the form,

$$\begin{pmatrix} u_{1L}(t) \\ u_{2L}(t) \\ u_{1R}(t) \\ u_{2R}(t) \end{pmatrix} = \begin{pmatrix} u_{1Ls} \\ u_{2Ls} \\ u_{1Rs} \\ u_{2Rs} \end{pmatrix} + \begin{pmatrix} \delta u_{1L} \\ \delta u_{2L} \\ \delta u_{1R} \\ \delta u_{2R} \end{pmatrix} \cdot e^{\lambda t} \tag{3.33}$$

yields a linearized equation,

$$\lambda \begin{pmatrix} \delta u_{1L} \\ \delta u_{2L} \\ \delta u_{1R} \\ \delta u_{2R} \end{pmatrix} = \mathbf{J} \begin{pmatrix} \delta u_{1L} \\ \delta u_{2L} \\ \delta u_{1R} \\ \delta u_{2R} \end{pmatrix} \tag{3.34}$$

where $\mathbf{J} = \begin{pmatrix} \frac{\partial G_1}{\partial u_{1L}} & \frac{\partial G_1}{\partial u_{2L}} & \frac{\partial G_1}{\partial u_{1R}} & 0 \\ \frac{\partial G_2}{\partial u_{1L}} & \frac{\partial G_2}{\partial u_{2L}} & 0 & \frac{\partial G_2}{\partial u_{2R}} \\ \frac{\partial G_3}{\partial u_{1L}} & 0 & \frac{\partial G_3}{\partial u_{1R}} & \frac{\partial G_3}{\partial u_{2R}} \\ 0 & \frac{\partial G_4}{\partial u_{2L}} & \frac{\partial G_4}{\partial u_{1R}} & \frac{\partial G_4}{\partial u_{2R}} \end{pmatrix}$

is the Jacobian of the system evaluated at the symmetric steady state. In order to identify existence of PB in the system, the condition given in Eq.(3.3) should be satisfied for an odd mode of the perturbation. For the one-dimensional projection (Eqs.(3.32)), the odd mode of the perturbation $(\delta \mathbf{U}(-\mathbf{x})) = -\delta \mathbf{U}(\mathbf{x}))$ must yield: $\delta u_{1L} = -\delta u_{1R}$ and $\delta u_{2L} = -\delta u_{2R}$. Substituting this into Eq.(3.34) to obtain $F_-(\lambda)$, in the limit $\lambda \to 0$ renders:

$$\lim_{\lambda \to 0} F_-(\lambda) = det \begin{pmatrix} (\frac{\partial G_1}{\partial u_{1L}} + \frac{\partial G_3}{\partial u_{1R}}) - (\frac{\partial G_1}{\partial u_{1R}} + \frac{\partial G_3}{\partial u_{1L}}) & (\frac{\partial G_1}{\partial u_{2L}} + \frac{\partial G_2}{\partial u_{2R}}) \\ (\frac{\partial G_2}{\partial u_{1L}} + \frac{\partial G_4}{\partial u_{1R}}) & (\frac{\partial G_2}{\partial u_{2L}} + \frac{\partial G_4}{\partial u_{2R}}) - (\frac{\partial G_2}{\partial u_{2R}} + \frac{\partial G_4}{\partial u_{2L}}) \end{pmatrix} = 0$$
$$\tag{3.35}$$

Thus, there exists a parameter set for which the existence of PB in the system Eq.(3.32) is guaranteed.

To identify whether the PB is sub-critical and thereby identify the existence of a SN_{PB}, the solution of the system Eqs.(3.31) is approximated as in Eq.(3.4):

$$u(x,t) = \phi(t)e^{ik_m\lambda} + \phi^*(t)e^{-ik_m\lambda} + u_0(t) + \sum_{n=2}^{3}(u_n(t)e^{nik_m\lambda} + u_n^*(t)e^{-nik_m\lambda})$$

$$v(x,t) = \phi(t)e^{ik_m\lambda} + \phi^*(t)e^{-ik_m\lambda} + v_0(t) + \sum_{n=2}^{3}(v_n(t)e^{nik_m\lambda} + v_n^*(t)e^{-nik_m\lambda})$$

(3.36)

The expansion is taken to $n = 3^{rd}$ order, rendering an amplitude equation of 5th order. As described in [65], the complex coefficients of the $n = 0^{th}, n = 2^{nd}$ and $n = 3^{rd}$ harmonics can be approximated as power series of $\phi(t)$. Substituting into Eqs.(3.31) allows to derive these coefficients. This yields a system of coupled ODEs representing the time evolution of the complex amplitudes, in this case, for $\phi(t)$, $u_0(t)$, $v_0(t)$, $u_1(t)$, $v_1(t)$, $u_2(t)$, $v_2(t)$, $u_3(t)$ and $v_3(t)$. Assuming that the dynamics of the higher order harmonics reaches their steady state much faster than the leading perturbation does, the derivatives of their amplitudes can be set to zero. This allows to obtain expressions of the amplitudes purely as functions ϕ and the parameters of the system as:

$$u_0(\phi) = (\frac{1}{q_{10}}(2(1-q_{11}) - \frac{q_9}{|\phi|^2}))|\phi|^2$$

$$v_0(\phi) = (\frac{r_1}{|\phi|^2} - 2r_2)|\phi|^2$$

$$u_2(\phi) = u_2^{(2)}\phi^2$$

$$v_2(\phi) = v_2^{(2)}\phi^2$$ (3.37)

$$u_3(\phi) = u_3^{(3)}\phi^3$$

$$v_3(\phi) = v_3^{(3)}\phi^3$$

where $u_2^{(2)} = \frac{1-q_{11}}{q_{10}-4k_m^2}$, $v_2^{(2)} = \frac{-r_2}{1+4Dk_m^2}$, $u_3^{(3)} = \frac{u_2^{(2)}+v_2^{(2)}-2q_{11}u_2^{(2)}}{q_{10}-9k_m^2}$ and $v_3^{(3)} = \frac{-r_2(u_2^{(2)}+v_2^{(2)})}{1+9Dk_m^2}$.
The dynamics of the leading harmonics ($n = 1$) can be written as:

$$\frac{d\phi}{dt} = c_1\phi + c_2\phi^3 - c_3\phi^5$$ (3.38)

where $c_1 = q_{10} - k_m^2 - r_1 + \frac{q_9(1-2q_{11})}{q_{10}}$, $c_2 = (1-q_{11})(2q_{11}-1)(\frac{2}{q_{10}} - \frac{1}{q_{10}-4k_m^2}) + r_2(2 + \frac{1}{1+4Dk_m^2})$ and $c_3 = 2q_{11}u_2^{(2)}u_3^{(3)} - u_2^{(2)}v_3^{(3)}$. Eq.(3.38) is of Stuart-Landau type and represents a normal form of a sub-critical pitchfork bifurcation. This shows the existence of SN_{PB} in the EGFR-PTP network.

To corroborate this, we also performed numerical bifurcation analysis on one-dimensional projection (Eqs.(3.32)) where the reaction terms have the form as defined in Eqs.(3.26), including the full form for $[N2_a]$, when $[E - E_p] = 0$.
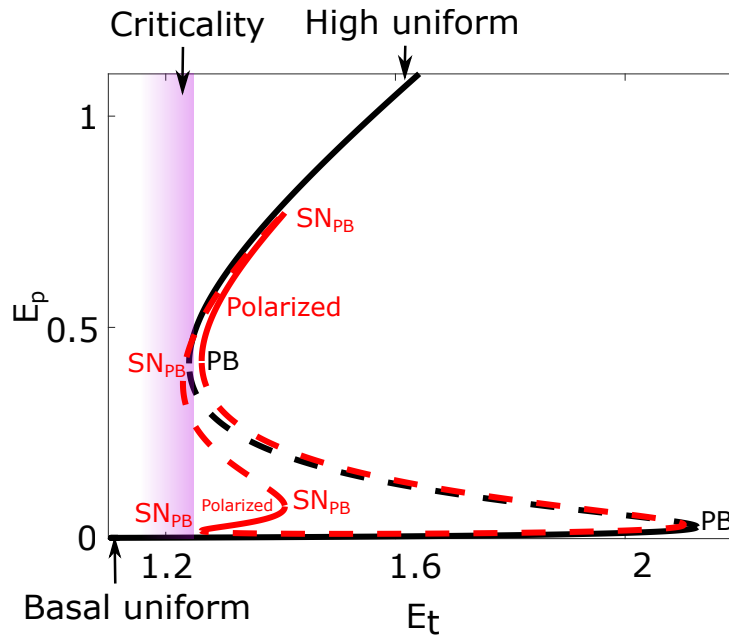
Figure 3.20 SubPB mechanism underlies EGF sensing in EGFR-PTP network. Bifurcation diagram corresponding to one-dimensional projection of Eqn. 3.26. E_p: ligandless phosphorylated EGFR, E_t: total EGFR on the plasma membrane. Magenta shaded region: critical organization. Stable/unstable steady states (solid/dashed lines): basal (homogeneous, black) and polarized (inhomogeneous, red) receptor activity. SN_{PB}: saddle-node bifurcation through which pitchfork bifurcation (*PB*) is stabilized.

The bifurcation analysis demonstrates that for the spatially-distributed EGFR network, the homogeneous steady state (HSS, the black solid line in Figure 3.20) loses stability via a symmetry-breaking pitchfork bifurcation (*PB*), giving rise to inhomogeneous steady states (IHSSs), stabilized via saddle-node bifurcations (SN_{PB}) (red branched lines). There is a coexistence between the HSS and the IHSS before the *PB*, rendering it sub-critical. Thus a SubPB mechanism underlies EGF sensing in epithelial cells.

In order to understand the responsiveness of EGFR phosphorylation to gradient EGF stimulation, stochastic reaction-diffusion simulations were performed using the full

system Eqs 3.26 by assuming PTPN2 at a quasi-steady state. For total EGFR concentration on the membrane that corresponds to the organization at criticality (magenta shaded region in Figure 3.20) in absence of stimulus, basal EGFR phosphorylation is uniformly distributed along the cell membrane as depicted in the response kymograph (Figure 3.21A bottom, time = 0-10 min).
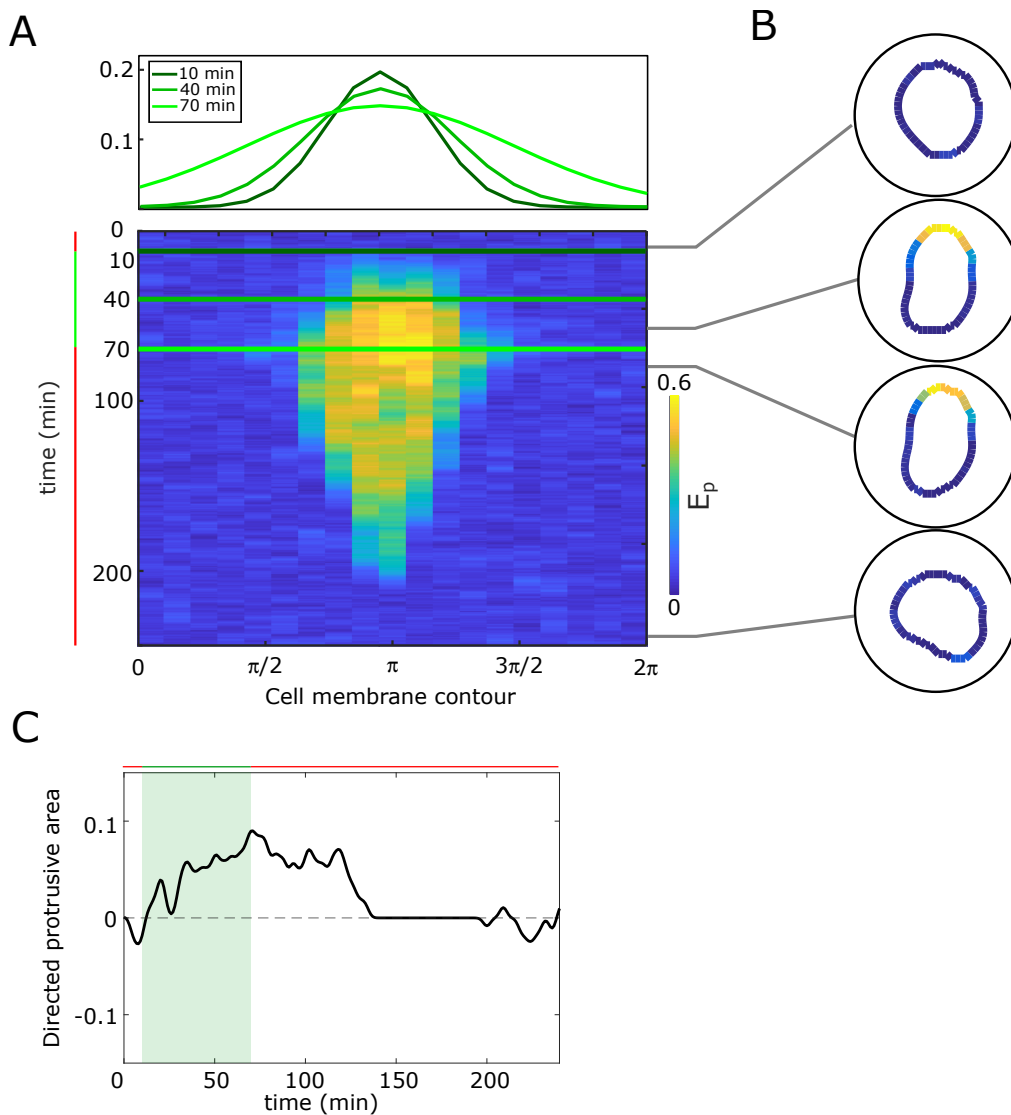
Figure 3.21 SubPB mechanism enables optimal sensing of spatial-temporal EGF signals through activity and shape changes. A, Top: Evolution of spatial EGF distribution. Bottom: Kymograph of E_p for organization at criticality from reaction-diffusion simulations of the network in Figure 3.19. B, Corresponding exemplary cell shapes with color coded E_p, obtained with the viscoelastic model in Figure 3.17B. C, Quantification of cell morphological changes from the example in B. green/red lines: gradient presence/absence.

The corresponding morphology obtained using viscoelastic simulation (discussed in section 3.7) shows a symmetrical cell shape (Figure 3.21B). A dynamic gradient stimulus whose slope changes from steep to shallow over time (Figure 3.21A, top) was introduced in the simulation (from time=10 min to 70 min) and it leads to rapid polarization of EGFR phosphorylation in the direction of the maximal EGF concentration (bottom). This response generates a cell shape with a clear front and back (Figure 3.21B). The polarized signaling state was maintained for a transient period after removal of the gradient, corresponding to the manifestation of memory of the localization of the previously encountered signal. The corresponding cell shape shows that memory of receptor polarization is also reflected in the shape as a memory of polarized shape. This transient memory state then transits back to the basal uniform state rendering again a symmetric cell shape (Figure 3.21B, top to bottom). The continuous morphological changes are quantified using directed protrusive area which captures net area change towards the gradient source and the temporal evolution of this quantity in Figure 3.21C show polarized cell shape during the gradient(green shaded region) is transiently maintained for approximately 60 min after the gradient removal. Equivalent feature of EGFRp polarization in epithelial cells are reported in A. Das (2022), doctoral dissertation.

In contrast, if the total EGFR concentrations on the membrane are higher and therefore the system is organized in the stable inhomogeneous state (Region II of sub-critical pitchfork bifurcation), even a transient signal induces switching to the polarized state that is permanently maintained, generating a long-term memory of the direction on the initial signal (Figure 3.22A). Thus, the cell is insensitive to subsequent stimuli from the same direction (Figure 3.22B, left), whereas consecutive gradients from opposite directions generate conflicting information that cannot be resolved (Figure 3.22B).

If the total EGFR concentration is low such that the organization is in the basal homogeneous (basal uniform in Figure 3.20), the cells remain insensitive to consecutive gradient stimuli (Figure 3.23A). On the other hand, an organization in the high uniform state renders uniform activation across the cell membrane within the first gradient and again remains insensitive to the consecutive stimulus (Figure 3.23B). Because of the homogeneous nature of the steady-state, lateral propagation aided by autocatalysis and diffusion of E_p together causes a global membrane activation. Thus, the organization in the homogeneous, symmetric regimes of sub-critical pitchfork bifurcation cannot project the information about gradient source localization onto cell contour.
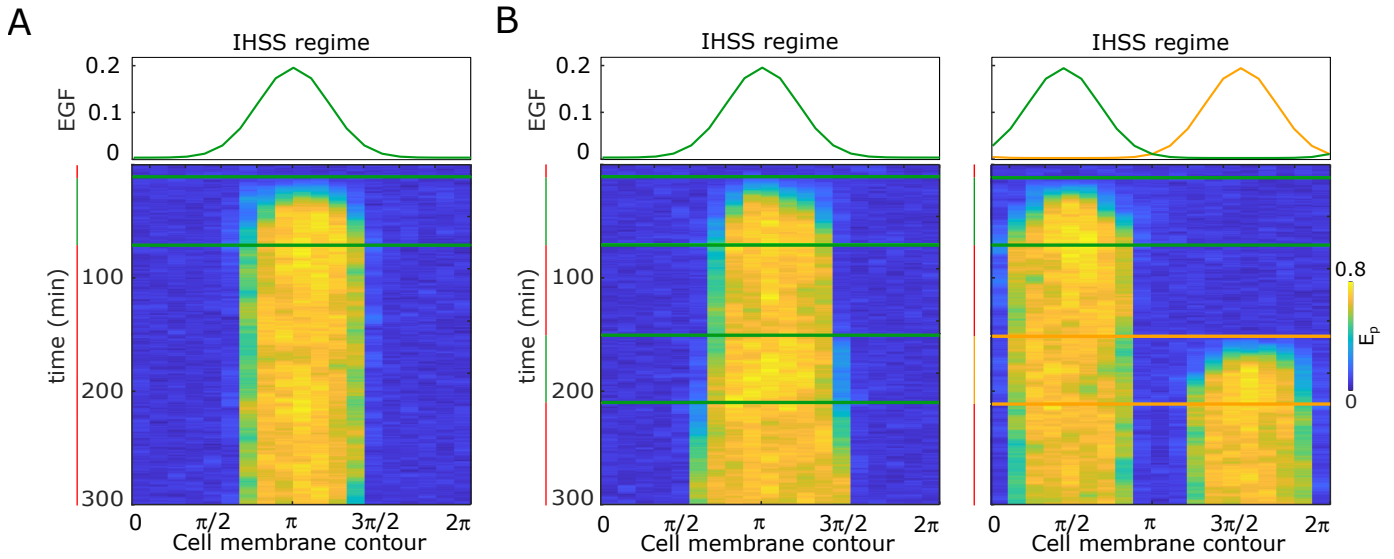
Figure 3.22 Permanent memory in receptor activity due to organization in stable inhomogeneous steady state hinders responsiveness. A, Top: Snapshot of position of dynamic EGF signals. Bottom: Respective kymograph of E_p changes showing permanent memory. B, Left: Same as A for two temporally disrupted dynamic gradients from the same direction. Right: for two temporally disrupted dynamic gradients with opposite localization. Vertical green(orange)/red lines: gradient presence/absence.

3.8.2 Molecular working memory enables epithelial cells to navigate in dynamic chemoattractant fields

To test whether the identified memory enables cellular navigation in environments where signals are disrupted, but also change over time and space, we subjected cells in the simulations and experiments to a changing EGF field as in Figure 3.8A. In the simulation, the kymograph analysis shows the E_p response where the first two gradients with similar localization are integrated and adapted the direction of polarization according to the reverse localization of the third gradient (Figure 3.24B). Simultaneously the shape and migration trajectory of the cell is captured using the viscoelastic model (Figure 3.24C). The cell sensed the initial dynamic gradient and polarized in the direction of maximal EGF concentration (green concentric circles at the top right corner), resulting in directed migration. The memory of the previously encountered signal localization enabled maintaining robust directional migration even when signals were disrupted while remaining sensitive to the newly emerging signals in the environment. Thus, the cell also rapidly adapted the orientation when encountering the third signal with opposite localization (orange concentric circles at the bottom
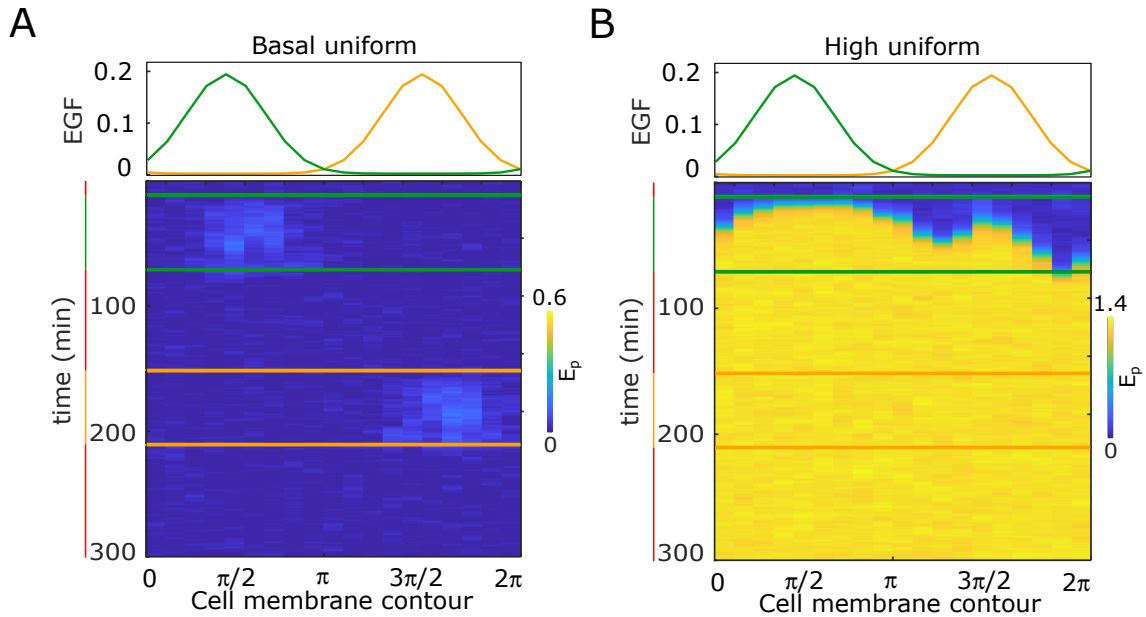
Figure 3.23 Organization in the homogeneous, symmetric steady state causes insensitivity in response. A, Organization at basal uniform steady state. Top: Snapshot of position of two temporally disrupted dynamic EGF signals with opposite localization. Bottom: Corresponding kymograph of E_p. B, Same as in A but for organization in uniform high steady state. Vertical green(orange)/red lines: gradient presence/absence.

right). On the other hand, the long-term memory resulting from the organization in the stable inhomogeneous steady-state regime hinders cellular adaptation to a changing gradient field. The initial dynamic gradient shifts the system to the stable polarization steady state where the system is maintained in a long-term, such that sensitivity to upcoming signals from the same direction is hindered (Figure 3.25A). Even more, the cell cannot resolve the conflicting information from a subsequent gradient from the opposite direction. Viscoelastic simulation shows that even though the cell has directional migration looks similar to the critical organization (Figure 3.24C) during the first two dynamic gradients, due to this conflicting information on the membrane the migration is halted (Figure 3.25B). Also, if the third gradient is absent the cell would persistently migrate in the same initial direction without stopping due to the irreversibility in the activation (results not shown).

We next tested these predictions experimentally by establishing an equivalent dynamic EGF spatial-temporal field. The field was generated in a computer-programmable microfluidic device (Figure 3.26A, left. See methods). For instance, the first gradient from top to bottom was created by a controlled flow of EGF (fluorescently tagged:
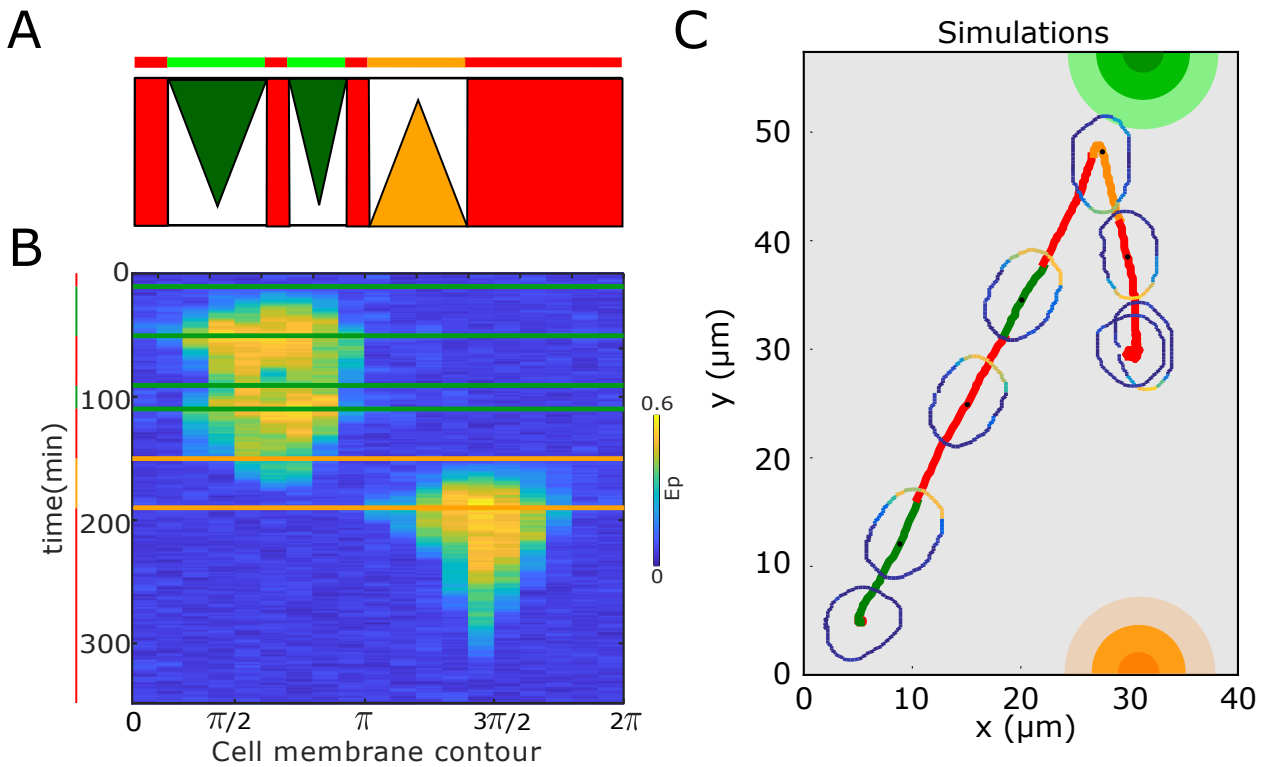
Figure 3.24 SubPB mechanism enables history-dependent single cell migration in changing chemoattractant field. A, Scheme of dynamic spatial-temporal EGF field implemented in the simulations Green(orange)/red: gradient presence/absence. B, Kymograph response of E_p for organization at criticality. C, Cellular response to the sequence of gradients as depicted in A, showing changes in E_p, cellular morphology and respective motility trajectory over time. Trajectory color coding corresponding to that in A, cell contour color coding with respective E_p values as in B. Cell size is magnified for better visibility. Coloured concentric circles: location of EGF gradient sources with opposite localization.

EGF[647]) with a maximal amplitude of 30ng/ml applied from the top and imaging media (IM) from the bottom (see materials and methods). Breast epithelial MCF10A cells were seeded in the cell chamber sandwiched between these flow inlets. Dynamic/static gradients can be generated across this chamber by controlling the pressure of media flow. The machine enables gradient direction reversal by switching the media between these inlets (Figure 3.26A, right). The duration of both dynamic gradients (1st and 3rd) were set to 4 hrs and the static gradient (2nd) duration to 1hr. From experiments conducted with single gradient stimulation (A. Das (2022), doctoral dissertation), the memory duration in directional migration of MCF10A cells after the gradient removal was estimated to be 50min. Therefore, the duration of inter gradient disruption for the gradient field (Figure 3.24A) was set to 30min in order to present the subsequent

A

B
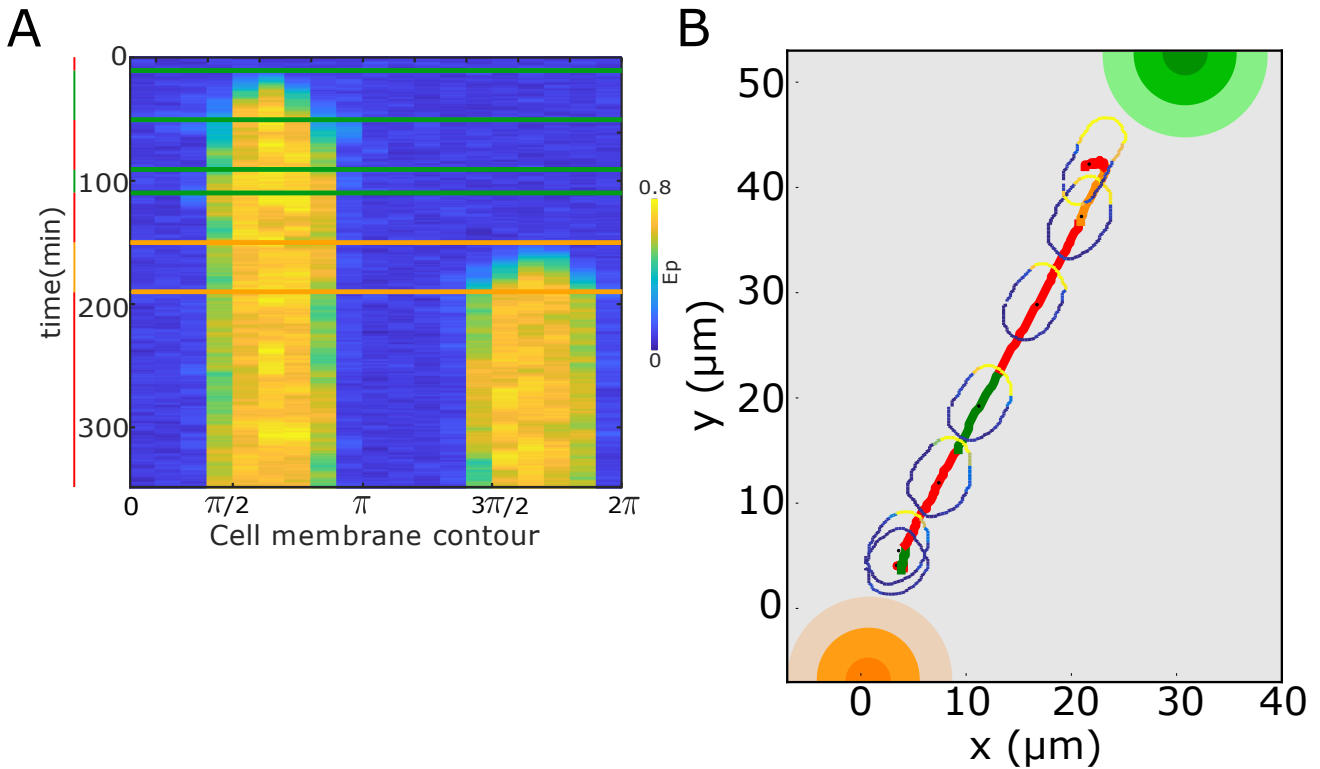
Figure 3.25 Organization in stable inhomogeneous steady state does not allow for history dependent response. A, Kymograph showing E_p response to gradient field in Figure 3.24A. B, Corresponding cell motility depicting halted migration trajectory. Colour schemes and descriptions as in Figure 3.24.

gradient within the memory of the previous. Cells were subjected to this gradient field and single-cell migration trajectories were tracked. An exemplary MCF10A migration track in Figure 3.26B shows that the MCF10A cell sensed the initial dynamic gradient from the top and migrated in the direction of the largest EGF concentration ($i \to ii$), maintaining the directionality even when the signal was temporary disrupted (*iii*).

Despite the memory in directional migration, cells remained responsive and adapted the duration of directional migration when presented with a second static gradient from the same direction, and subsequently prioritized the third, newly encountered signal with opposed orientation (*iv*). The cell also maintained the direction of migration after the third gradient (*v*) before becoming random (*vi*). The cell shape changes depicted along with the cell track show the polarized shape is also continuously being adapted. Migration trajectories of an ensemble of cells showing the same responsiveness are shown in Figure 3.26C. The various extent of migration distance is a consequence of cell-to-cell variability and their relative position within the cell chamber because
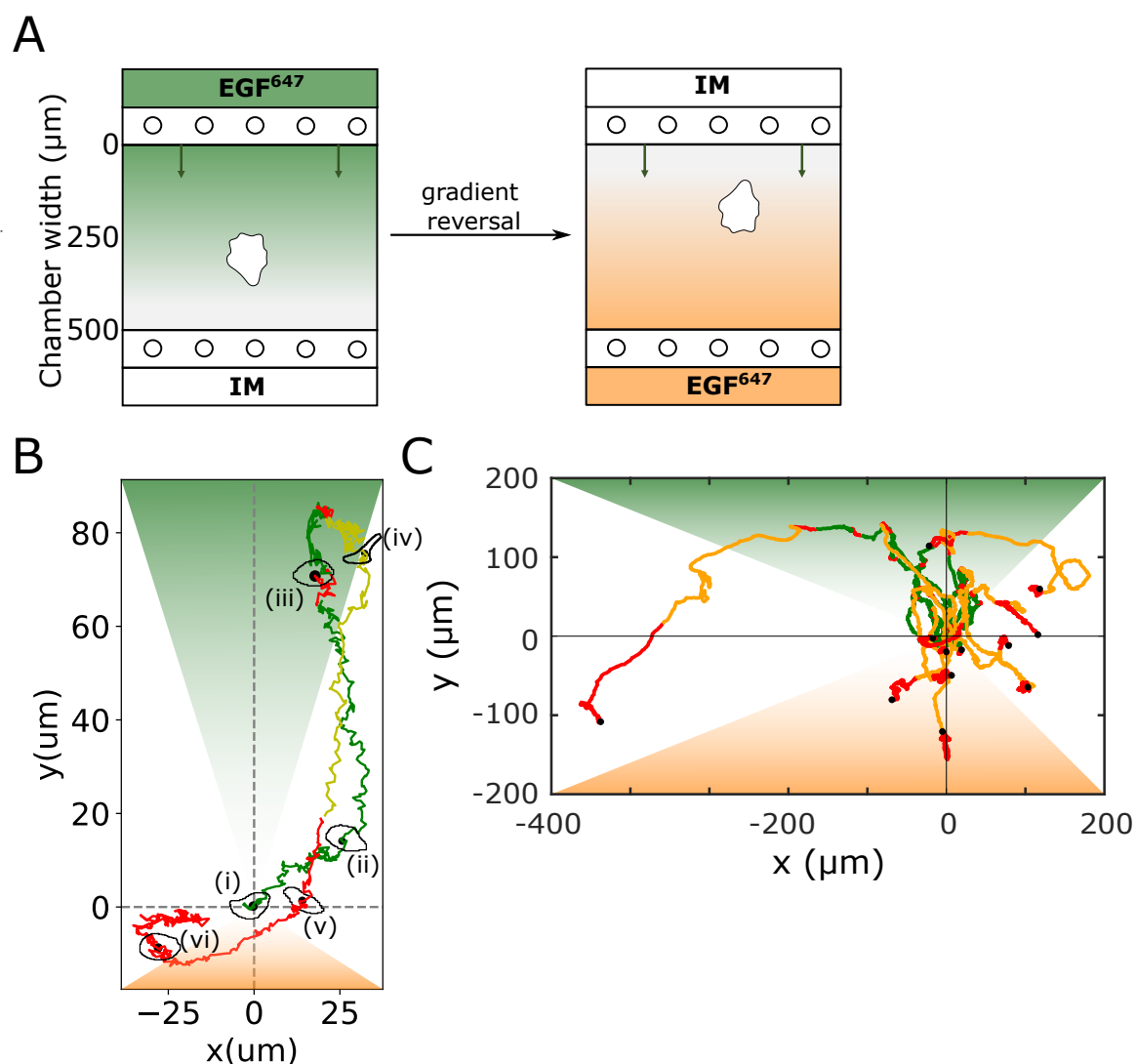
Figure 3.26 Working memory in directional migration enables epithelial cells to achieve long range navigation under changing gradient fields. A, Scheme of EGF^{647}-gradient generation and reversal in microfluidic chamber. B, Representative MCF10A single cell divergent plot and cellular morphologies at distinct time-points, when subjected to dynamic EGF^{647} gradient field as in Figure 3.24A. C, Divergence plots of all MCF10A single cell trajectories quantified during migration in dynamic EGF^{647} gradient same as in Figure 3.24A. n=12, N=5. Black dots: end of track. In B,C: Trajectory color coding corresponding to that in Figure 3.24A.

of which they sense varying strength of EGF gradients across their size. In order to quantify the temporal memory in directional migration as well as the continuous adaptation of MCF10A cells to novel cues, the projection of the cell's relative turning angles was quantified. Instantaneous turning angles of cell migration with respect to
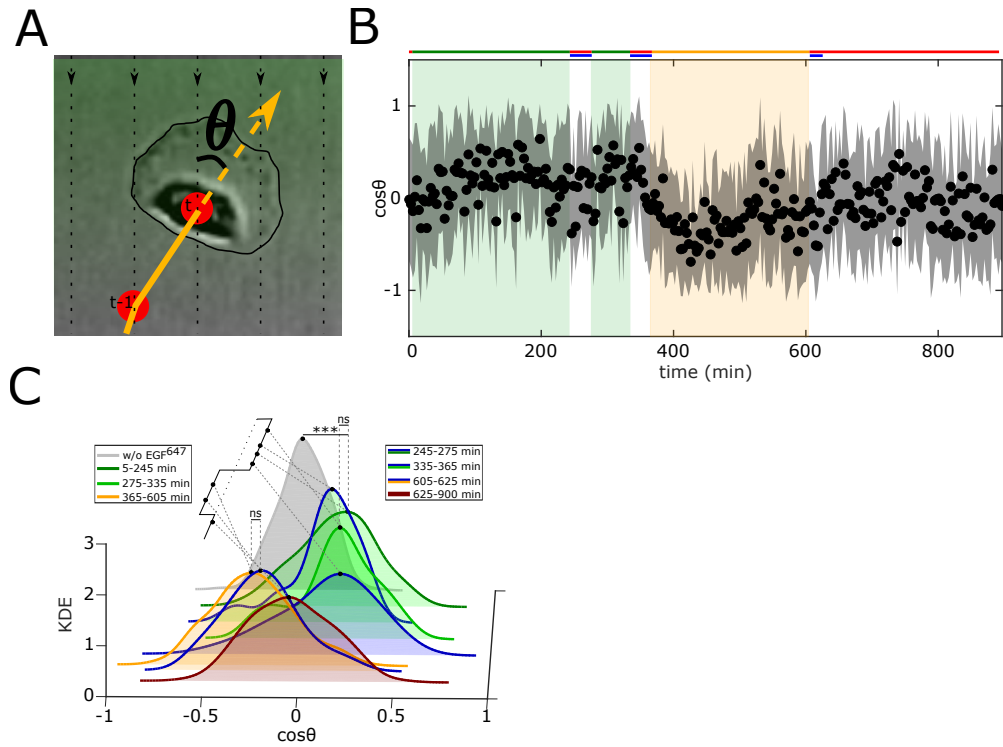
Figure 3.27 Quantification of dynamic memory in directional motility using relative turning angle. A, Scheme of single-cell turning angle estimation ($\cos\theta$). Dashed yellow arrow: direction of migration. vertical dashed lines: direction of gradient. B, Projection of cells' relative turning angles ($\cos\theta$) depicting their orientation towards the respective localized signals. Mean±s.d. from cells in Figure 3.26C. C, Corresponding kernel density estimates (intervals and color coding in legend). p-values: $***$, $p \leq 0.001$, ns: not significant, KS-test.

the gradient direction (θ) were estimated (Figure 3.27A) and the temporal evolution of cosine of that angle is shown in Figure 3.27B. The cellular migration trajectories aligned with the source direction ($\cos\theta$ approached 1) during the first gradient (first green shaded region) and are maintained temporally after gradient removal. Upon the second gradient (second green shaded region) the $\cos\theta$ values remained at the same level and are maintained until the onset of the reversed gradient (orange shaded region). Rapid reversal of direction of migration causes the $\cos\theta$ values to approach -1 and this value is maintained for a duration of $\approx$ 20min after the gradient is switched off and before returning to a migration pattern characteristic for stimulus absence or during uniform stimulation ($\cos\theta \approx 0$). Additionally, the respective KDE distributions derived from the subsequent time-intervals of gradient presence/absence corroborate

that cells maintain the same migration characteristics within the memory intervals as during the immediately recent gradient phase (Figure 3.27C).

These results demonstrate that cells navigate in changing gradient fields by utilizing a molecular mechanism of working memory that is an intrinsic feature of receptor tyrosine kinase networks.

Chapter 4

Discussion

Single cells within tissues and organisms continuously sense spatially and temporally varying signals from their surroundings. Surface receptors embedded in biochemical networks within these cells act as a sensing entity that reliably transmits specific information about the extracellular environment, allowing the cell to adjust its physiological state to changing conditions. However, the underlying mechanisms involving this detection, integration, and processing of external signals are not well understood especially during chemotaxis, a directed movement of the cell towards the signal source. In this thesis, the main objective was to identify such a minimal guidance mechanism that enables biochemical networks within cells to process dynamic spatial-temporal cues.

4.1 Attractor based cellular computation

A system-level description of cellular states brings in the idea of stable attractors from dynamical systems theory. These attractors are maintained by energy-driven intracellular processes and capture the nonequilibrium nature associated with cellular states. The attractor concept has found a broad implementation in developmental studies and was pioneered by Waddington in 1957 where he metaphorically depicted how a cell progresses from an undifferentiated state to one of a number of differentiated cell fates during development [115]. The attractor description was used to capture stable gene expression patterns within a cell that determined its identity. The cell was represented as a ball that rolls on terrain with multiple valleys of stable attractors separated by ridges that prevent state transitions between them once the cell identity is determined [116]. These landscapes and the attractors are shaped by gene regulatory

networks (GRN). Experimental evidence has recently demonstrated the existence of higher-dimensional stable attractors within GNR that represent distinct cellular phenotype [117] and the possible coexistence of multiple attractors corresponding to different differentiated states [118].

During the symmetry-breaking transition from an un-differentiated multilineage primed state to a differentiated state, the cell encodes specific information into its identity similar to how cells respond to spatial cues by undergoing a transition from an un-polarized state to a polarized state. There were several mathematical concepts that tried to capture the symmetry-breaking nature during the differentiation process. Many such approaches were based on single-cell multistability [119]. In those models, cell states (differentiated or undifferentiated) were represented by different homogenous attractors so the differentiation process largely depended on the initial state of the cell. Due to this reason, those models failed to account for robustness in differentiated cell type proportions. A recent study [120] has shown that a population-based symmetry-breaking mechanism, based on a sub-critical pitchfork bifurcation, captures this essential feature. It was shown that reliable proportioning is a dynamical consequence of inhomogeneous steady-state (IHSS) solutions that arise from the sub-critical pitchfork bifurcation. An initial undifferentiated state, realized through a homogeneous steady state, was possible because of the parameter organization before this IHSS, and the timing of the differentiation was then triggered in a self-organizing manner by cell number increase as the population grows in size. During cellular differentiation process, an attractor-based cell fate commitment enabled irreversibility which was a crucial required feature.

4.2 Limitations of cellular sensing through stable attractors

This poses a question whether mechanisms based on stable attractors apply in general to information processing in cells, especially during processes such as chemotaxis? A major disadvantage associated with storing information about the extracellular signal in a stable attractor is that the cell becomes insensitive to spatial and temporal variations in the signal. Due to the lack of plasticity, the response cannot follow the dynamics of external signals. Since cell polarization is a crucial step during cells' response to chemical cues, several mathematical models based on positive feedbacks, incoherent feed-forward, excitable or Turing-like networks have been proposed to describe the

features associated with it. Each of these models was tailored to account for only a few of the observed features local to the different cell types that they were associated with. In order to account for the rest of the features, addition of other feedbacks motif was necessary, with components whose biochemical identity is not known (Figure 1.16). This poses a difficulty for experimental testing.

Identification of symmetry breaking mechanisms associated with those models showed that their operation principles are stable attractor-based. The three main types of models that we considered differed in their type of stable attractor as well. The wave pinning- and Turing-type models have an inhomogeneous attractor organization (Figure 3.9B, 3.10B) while the LEGI-type model that lacked an inherent symmetry breaking mechanism has a homogenous attractor organization (Figure 3.11B). Further quantitative analysis has shown that the difference in their underlying mechanisms caused significant differences in their polarization responses as well. Wave pinning-type models require a threshold for activation, thus accounting for a nonpolar state (Figure 3.12B, blue) that was experimentally observed in many cell types such as neutrophils and fibroblasts. The Turing-type models inherently had an unstable nonpolar state spontaneously polarizing even in the absence of any signals (Figure 3.12B, green). Both of these model types showed permanent memory in the achieved polarization response which hindered their responsiveness towards upcoming signals irrespective of signal's localization (Figure 3.14, 3.16B,C). LEGI-type models, on the other hand, only polarized in the presence of a gradient and didn't exhibit any memory in the response (Figs. 3.12 magenta, 3.16D). In a dynamic environment, history-dependent sensing is crucial and requires an ability to memorize and store information about previous signal encounters. Neither the permanent memory arising from a stable inhomogenous attractor nor the lack of memory from a stable homogeneous attractor can account for this (Figure 3.6B,C). In our previous study, we have shown that the memory should be transient and dynamic to allow for signal integration while sensing time-varying homogeneous signals [35]. We demonstrated here that the existing mathematical models for the polarization that encode information using stable attractors could not account for sensing of dynamic environments.

4.3 SubPB is a generic mechanism for cellular information processing

A subcritical pitchfork bifurcation captures the transition from a homogeneous steady state (HSS) to an inhomogeneous steady-state (IHSS) through a *PB* (Figure 1.1A). Different inhomogeneous steady state branches, that correspond to polarization in different directions, emerge from the *PB* are initially unstable and they are stabilized by saddle-node bifurcation (*SN*) making it sub-critical. The proposed SubPB mechanism has such a sub-critical pitchfork bifurcation together with the critical organization in the vicinity of *SN*. This unique organization unifies different characteristic features emerging from the two bifurcations:

- Robust polarization features through the signal-induced unfolding of *PB*. It accounts for both the existence of a threshold for activation as well as nonlinear amplification in polarized response (Figure 3.2).

- Dynamic transient memory from "ghost" of *SN* that stores information about the direction of previously encountered signals through maintaining a prolonged polarized state enabling a history-dependent signal integration (Figure 3.4).

We have shown both using experiments and theory that the EGFR sensing network in epithelial cells has an underlying SubPB mechanism [121]. Investigation into other RTKs and GPCRs have shown that they also exhibit similar spatial organizations as well as the type of network topologies and I therefore suggest that SubPB mechanism is not limited to epithelial cells alone but is likely a generic mechanism that governs cellular sensing.

One of the interesting future directions is to investigate how SubPB mechanism, so far explored at a single cell level, manifests during collective cell migration which is also crucial during wound healing, morphogenesis, cancer progression [122]. Like in single cells, growth factor sensing and maintenance of collective cell polarity is crucial for their migration [123] and are shown to exhibit enhanced gradient sensing capabilities than single cells [124]. This raises the possibility of efficient mechanisms for sensing that emerge through intercellular communication. Within the population, cell-cell variability of receptor abundance would imply that some individual cells might be posed away from the critical region that affects their sensitivity. There are evidence about the transport of receptors, such as EGFR, between cells via extracellular vesicles [125, 126]. Such intercellular communication could compensate for the variability

and the emergence of a population level mechanism that shares dynamical features of SubPB mechanism.

4.4 Dynamic transient memory in signaling and shape enables history dependent navigation

In tissues of multicellular organisms, natural chemoattractant gradients are often dynamic and disrupted in both time and space [50, 4, 127]. Cells that need to execute long-range migration through such complex tissue environments need to sense those signals and move continuously (Figure 4.1). Both *in silico* and *in vitro* experiments have captured that the SubPB mechanism not only enables robust sensing of such signals but also the transient memory in signaling is translated to transient memory in shape (Figure 3.24C, 3.26B)(A. Das (2022), doctoral dissertation). During such process, the cellular shape can be considered as a repository of information that flows through the cell signaling network [41] and has been shown to store the information about chemical sources through long-lived cytoskeletal structures actuated by signaling [128]. The metastable characteristics associated with signaling and shape enable responsiveness and adaptability towards novel signals. For instance, in the presence of conflicting signals from different directions, the cell can resolve that information and can continue to migrate towards the strongest signal source (Figure 4.1).

A dynamical mechanism for transient memory in the biochemical network has long been investigated since it provides a solution to several unsolved questions like the "back of the wave problem" associated with *Dictyostelium discoideum* aggregation in response to cAMP waves that was discussed in section 1.1. When the wave of chemoattractant sweeps across the cells, the initial polarization direction during the rising part of the wave needs to be maintained during the falling part in order to avoid repolarization and loss of information about the direction to the wave source. The presence of a dynamic transient memory in both signaling and shape, whose duration is longer than the duration of the falling part, would enable the cells to surpass this problem and SubPB mechanism could account for such a response.

Similar inferences about advantages of transient memory was described previously in the context of goal directed behavior of an artificial network of self-recurrent units in response to non-stationary environment [129]. It was shown that organization near *SN* bifurcation give rise to this transient memory that enabled the network to
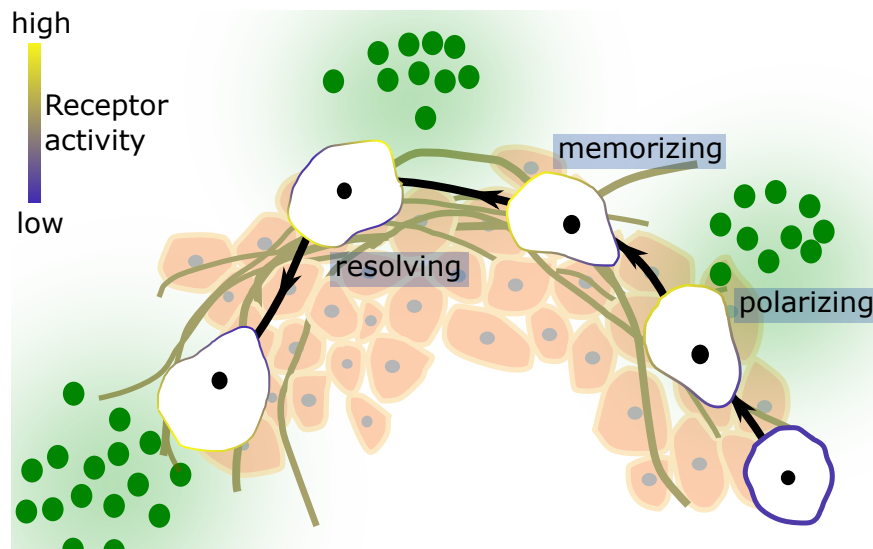
Figure 4.1 Schematic of a single cell executing a long-range migration through a complex tissue environment by sensing spatially and temporally disrupted chemoattractant fields. The SubPB mechanism enables both robust polarization in signaling and shape as well as its transient maintenance while the signals are absent, resulting in a history-dependent dynamical signal sensing.

simultaneously have two opposing features: maintenance and quick transition which were required for attention during such behavior and enabled them to outperform other memory-less networks.

4.5 Steady state independent information processing through transient trajectories

Memory-guided migration of cells as in Figure 4.1 suggest that, in the biochemical network, the information about previously encountered signals can be continuously encoded in the protein activity trajectories rather than the steady-state. The advantage of this trajectory-based sensing is that during an encounter with new signals, the trajectories can be re-triggered easily since they are not bound to any stable attractor. Similar ideas of trajectory-based computations are so far explored in neuronal dynamics [130].

Different studies have shown that neuronal networks encode information about temporally varying inputs into the trajectory of neuronal activity [130, 131]. They did this

by measuring the firing rates of each neuron in the network in response to external signals. The entire state-space of the network, where each dimension represents one of the neurons, cannot be visualized. Therefore they have used principal component analysis to map those higher-dimensional trajectories into three-dimensional state spaces. In [130] it was shown that, upon stimulating with time-varying odor signal, the three-dimensional trajectories showed an initial transient phase before settling into a stable attractor. They found that depending on the temporal features of the signal, odor-specific trajectories were separated in space during the transients itself. This separation, they conjectured is key to odor discrimination in the studied organism. A similar observation of trajectory divergence that leads to distinct behavioral response was made in the central nervous system of medicinal leech [131]. It was found that trajectories all start in one region in state space and then diverge towards two different regions. The separation between the trajectories again serves as an objective measure of the decision-making. These studies have suggested that steady-state measures of neuronal activity are inappropriate to understand information encoding of transient signals.

This idea has found applications in various other fields such as in information processing technology. In order to perform real-time computations on continuous streams of data, different frameworks such as reservoir computing have developed principles similar to the neuronal networks that are steady-state independent [132, 133]. In such frameworks, the input data are transformed into spatiotemporal patterns in a high-dimensional space by a recurrent neural network in the reservoir. A fading memory property of this reservoir together with the higher dimensional representation enabled classification of originally inseparable inputs during prediction tasks.

It is possible to envision such a higher-dimensional representation of the input signals in single cells through activities of different protein that are in the cytoplasm which mimics a reservoir. The information from signals that are translated by the receptor network is then relayed to this pool with proteins having various recurrent interactions with each other. These proteins such as Akt, ERK, etc are key regulators of transcription factors in GRNs [134] which can, in turn, modulate gene expressions and cell fates. This establishes an extended, multi-component sensing entity with transient dynamics similar to a neuronal network.

A recent study [135] in PC-12 cells has shown that stimulation using the same growth factor with different temporal frequencies induced different physiological responses raising questions about how temporal features of the same growth factor could possibly bias cell fate determination. Conceptually, a trajectory-based information encoding,

analogous to the one in the neuronal network, could be used to address this problem. The difference in temporal features of the signal could result in the separation of trajectories in the state space, where each dimension corresponds to the activity of each protein in the cytoplasm pool. The separation could lead to differential regulation of immediate-early genes (IEGs) and cell fate determination. Recent advancements towards the simultaneous measurement of the temporal response of multiple protein activities [136] would enable more insights into this signal-specific, trajectory-based information processing by single cells.

Information-theoretic approaches have revealed that single cells, especially during chemotaxis, exhibit the highest information flow rate through signaling networks. This information flow rate, which captures how well information from signals are processed, was quantified using channel capacity or mutual information between the input signal and a downstream response element [137–140]. Parallel theoretical analysis on dynamical systems has shown that mutual information between input and output is maximal at bifurcation points [141, 142]. Taking these together, the results suggest that a mechanism that inherently has a critical organization could be enabling higher information transfer during a single cell's response to extracellular signals. These approaches so far have demonstrated information content between one signal input and one output variable. However, this can be improved by the measurement of multiple protein activities from the cytoplasm pool upon time-varying input signals. Further genetic perturbations can be used to tune the parametric organization of receptor networks away from the critical organization to test its effect on cells' information transfer efficiency.

Bibliography

[1] A. Stanoev, A. Mhamane, K.C. Schuermann, H.E. Grecco, W. Stallaert, M. Baumdick, Y. Brüggemann, M.S. Joshi, P. Roda-Navarro, S. Fengler, R. Stockert, L. Roßmannek, J. Luig, A. Koseska, and P.I.H. Bastiaens. Interdependence between EGFR and Phosphatases Spatially Established by Vesicular Dynamics Generates a Growth Factor Sensing and Responding Network. *Cell Systems*, 7(3):295–309.e11, 2018.

[2] Lacy J Barton, Michelle G LeBlanc, and Ruth Lehmann. Finding their way: themes in germ cell migration. *Current opinion in cell biology*, 42:128–137, 2016.

[3] Adam Shellard and Roberto Mayor. Chemotaxis during neural crest migration. *Seminars in cell & developmental biology*, 55:111–8, 2016.

[4] Tim Lämmermann, Philippe V. Afonso, Bastian R. Angermann, Ji Ming Wang, Wolfgang Kastenmüller, Carole A. Parent, and Ronald N. Germain. Neutrophil swarms require ltb4 and integrins at sites of cell death in vivo. *Nature*, 498(7454):371–375, Jun 2013.

[5] Erik S. Welf, Shoeb Ahmed, Heath E. Johnson, Adam T. Melvin, and Jason M. Haugh. Migrating fibroblasts reorient directionality by a metastable, pi3k-dependent mechanism. *The Journal of Cell Biology*, 197:105 – 114, 2012.

[6] Pauline Schaap, Johan E. Pinas, and Mei-Jing Wang. Patterns of cell differentiation in several cellular slime mold species. *Developmental Biology*, 111:51–61, 1985.

[7] Dirk Dormann and Cornelis J. Weijer. Chemotactic cell movement during development. *Current opinion in genetics & development*, 13 4:358–64, 2003.

[8] Hiroko Sano, Andrew D Renault, and Ruth Lehmann. Control of lateral migration and germ cell elimination by the drosophila melanogaster lipid phosphate phosphatases wunen and wunen 2. *The Journal of Cell Biology*, 171:675 – 683, 2005.

[9] K J Tomchik and Peter N. Devreotes. Adenosine 3',5'-monophosphate waves in dictyostelium discoideum: a demonstration by isotope dilution–fluorography. *Science*, 212 4493:443–6, 1981.

[10] Thomas Gregor, Koichi Fujimoto, Noritaka Masaki, and Satoshi Sawai. The onset of collective behavior in social amoebae. *Science*, 328:1021 – 1025, 2010.

[11] Goldstein. Traveling-wave chemotaxis. *Physical review letters*, 77 4:775–778, 1996.

[12] Howard C. Berg and Edward M. Purcell. Physics of chemoreception. *Biophysical journal*, 20 2:193–219, 1977.

[13] PA Insel, A Snead, F Murray, L Zhang, H Yokouchi, T Katakia, O Kwon, D Dimucci, and A Wilderman. Gpcr expression in tissues and cells: Are the optimal receptors being used as drug targets? *British Journal of Pharmacology*, 165(6):1613–1616, 2012.

[14] Joseph Schlessinger. Cell signaling by receptor tyrosine kinases. *Cell*, 103:211–225, 2000.

[15] Anton Arkhipov, Yibing Shan, Rahul K Das, Nicholas F. Endres, Michael P. Eastwood, David E. Wemmer, John Kuriyan, and David E. Shaw. Architecture and Membrane Interactions of the EGF Receptor. *Cell*, 152:557–569, 2013.

[16] Joseph Schlessinger. Ligand-Induced, Receptor-Mediated Dimerization and Activation of EGF Receptor. *Cell*, 110:669–672, 2002.

[17] Joseph Schlessinger. Cell signaling by receptor tyrosine kinases. *Cell*, 103(2):211–225, 2000.

[18] Tony Pawson and Piers Nash. Assembly of cell regulatory systems through protein interaction domains. *Science*, 300(5618):445–452, 2003.

[19] M. Wagner, Melissa M. Stacey, Bernard A. Liu, and Tony Pawson. Molecular mechanisms of sh2- and ptb-domain-containing proteins in receptor tyrosine kinase signaling. *Cold Spring Harbor perspectives in biology*, 5 12:a008987, 2013.

[20] Peter J. Verveer, Fred Silvester Wouters, Andrew R. Reynolds, and Philippe I. H. Bastiaens. Quantitative imaging of lateral erbb1 receptor signal propagation in the plasma membrane. *Science*, 290 5496:1567–70, 2000.

[21] AR. Reynolds, C. Tischer, PJ. Verveer, O. Rocks, and P.I.H. Bastiaens. EGFR activation coupled to inhibition of tyrosine phosphatases causes lateral signal propagation. *Nat Cell Biol*, 5:447–453, 2003.

[22] Christian Tischer and Philippe I. H. Bastiaens. Lateral phosphorylation propagation: an aspect of feedback signalling? *Nature Reviews Molecular Cell Biology*, 4:971–975, 2003.

[23] Weiguang Mao, Rosalyn B. Irby, Domenico Coppola, Lingmin Fu, Marek Wloch, Joel G. Turner, Hua Yu, Roy Garcia, Richard Jove, and Timothy Yeatman. Activation of c-src by receptor tyrosine kinases in human colon cancer cells with high metastatic potential. *Oncogene*, 15:3083–3090, 1997.

[24] Martin E Baumdick, Márton Gelléri, Chayasith Uttamapinant, Václav Beránek, Jason W. Chin, and Philippe I. H. Bastiaens. A conformational sensor based on genetic code expansion reveals an autocatalytic component in EGFR activation. *Nature Communications*, 9:3847, 2018.

[25] Martin Baumdick, Yannick Brüggemann, Malte Schmick, Georgia Xouri, Ola Sabet, Lloyd Davis, Jason W Chin, and Philippe IH Bastiaens. EGF-dependent re-routing of vesicular recycling switches spontaneous phosphorylation suppression to EGFR signaling. *eLife*, 4:e12223, nov 2015.

[26] Aneta Koseska and Philippe I.H. Bastiaens. Processing temporal growth factor patterns by an epidermal growth factor receptor network dynamically established in space. *Annual Review of Cell and Developmental Biology*, 36(1):359–383, 2020.

[27] Mina D. Marmor and Yosef Yarden. Role of protein ubiquitylation in regulating endocytosis of receptor tyrosine kinases. *Oncogene*, 23:2057–2070, 2004.

[28] Michael R Dores and JoAnn Trejo. Endo-lysosomal sorting of g-protein-coupled receptors by ubiquitin: Diverse pathways for g-protein-coupled receptor destruction and beyond. *Traffic*, 20:101 − 109, 2019.

[29] Nicholas K. Tonks. Protein tyrosine phosphatases: from genes, to function, to disease. *Nature Reviews Molecular Cell Biology*, 7:833–846, 2006.

[30] Yosef Yarden and Mark X. Sliwkowski. Untangling the erbb signalling network. *Nature Reviews Molecular Cell Biology*, 2:127–137, 2001.

[31] Y. S. Bae, Sang Won Kang, Min Seok Seo, Ivan C. Baines, Ephrem Tekle, P. Boon Chock, and Sue Goo Rhee. Epidermal Growth Factor (EGF)-induced Generation of Hydrogen Peroxide. *The Journal of Biological Chemistry*, 272:217 − 221, 1997.

[32] Steven H Strogatz and Robert M Westervelt. Predicted power laws for delayed switching of charge-density waves. *Physical Review B*, 40(15):10501, 1989.

[33] Steven H Strogatz. *Nonlinear dynamics and chaos: with applications to physics, biology, chemistry, and engineering*. Westview Press, 2014.

[34] Eugene M. Izhikevich. *Dynamical Systems in Neuroscience: The Geometry of Excitability and Bursting*. The MIT Press, 2010.

[35] Angel Stanoev, Akhilesh P. Nandan, and Aneta Koseska. Organization at criticality enables processing of time-varying signals by receptor networks. *Mol Syst Biol*, 16:e8870, 2020.

[36] Strogatz and Westervelt. Predicted power laws for delayed switching of charge-density waves. *Physical review. B, Condensed matter*, 40 15:10501–10508, 1989.

[37] Josep Sardenyes and Ricard V. Sole. Ghosts in the origins of life? *International Journal of Bifurcation and Chaos*, 16(09):2761–2765, 2006.

[38] Kristina S. Stapornwongkul and Jean-Paul Vincent. Generation of extracellular morphogen gradients: the case for diffusion. *Nature reviews. Genetics*, 22:393–411, 2021.

[39] Flora Llense and Sandrine Etienne-Manneville. *Front-to-Rear Polarity in Migrating Cells*, pages 115–146. Springer International Publishing, Cham, 2015.

[40] Konstantin Gavriljuk, Bruno Scocozza, Farid Ghasemalizadeh, Hans Seidel, Akhilesh P. Nandan, Manuel Campos-Medina, Malte Schmick, Aneta Koseska, and Philippe I. H. Bastiaens. A self-organized synthetic morphogenic liposome responds with shape changes to local light cues. *Nature Communications*, 12, 2021.

[41] Malte Schmick and Philippe I. H. Bastiaens. The interdependence of membrane shape and cellular signal processing. *Cell*, 156:1132–1138, 2014.

[42] Chris Janetopoulos, Lan Ma, Peter N. Devreotes, and Pablo A. Iglesias. Chemoattractant-induced phosphatidylinositol 3,4,5-trisphosphate accumulation is spatially amplified and adapts, independent of the actin cytoskeleton. *Proceedings of the National Academy of Sciences*, 101(24):8951–8956, 2004.

[43] Monica Skoge, Haicen Yue, Michael Erickstad, Albert Bae, Herbert Levine, Alex Groisman, William F. Loomis, and Wouter-Jan Rappel. Cellular memory in eukaryotic chemotaxis. *Proceedings of the National Academy of Sciences*, 111(40):14448–14453, 2014.

[44] Satoru Funamoto, Ruedi Meili, Susan Lee, Lisa Parry, and Richard A. Firtel. Spatial and temporal regulation of 3-phosphoinositides by pi 3-kinase and pten mediates chemotaxis. *Cell*, 109:611–623, 2002.

[45] Van Haastert. Sensory adaptation of dictyostelium discoideum cells to chemotactic signals. *Journal of Cell Biology*, 96:1559–1565, 1983.

[46] Tim Lämmermann and Wolfgang Kastenmüller. Concepts of gpcr-controlled navigation in the immune system. *Immunological Reviews*, 289(1):205–231, 2019.

[47] Braedon McDonald, Keir Pittman, Gustavo Batista Menezes, Simon A. Hirota, Ingrid Slaba, Christopher Curtis Matchett Waterhouse, Paul L. Beck, Daniel A. Muruve, and Paul Kubes. Intravascular danger signals guide neutrophils to sites of sterile inflammation. *Science*, 330:362 – 366, 2010.

[48] Mieke Metzemaekers, Mieke Gouwy, and Paul Proost. Neutrophil chemoattractant receptors in health and disease: double-edged swords. *Cellular and Molecular Immunology*, 17:433 – 450, 2020.

[49] Visakan Kadirkamanathan, Sean R. Anderson, Stephen A. Billings, Xiliang Zhang, Geoffrey R. Holmes, Constantino C. Reyes-Aldasoro, Philip M. Elks, and Stephen A. Renshaw. The neutrophil's eye-view: Inference and visualisation of the chemoattractant field driving cell chemotaxis in vivo. *PLOS ONE*, 7(4):1–11, 04 2012.

[50] Philipp Niethammer, Clemens Grabher, A. Thomas Look, and Timothy J. Mitchison. A tissue-scale gradient of hydrogen peroxide mediates rapid wound detection in zebrafish. *Nature*, 459:996 – 999, 2009.

[51] Guy Servant, Orion D. Weiner, Enid R. Neptune, John W. Sedat, and Henry R. Bourne. Dynamics of a chemoattractant receptor in living neutrophils during chemotaxis. *Molecular Biology of the Cell*, 10(4):1163–1178, 1999. PMID: 10198064.

[52] Guy Servant, Orion David Weiner, Paul Herzmark, Tamas Balla, John Sedat, and Henry R. Bourne. Polarization of chemoattractant receptor signaling during neutrophil chemotaxis. *Science*, 287 5455:1037–40, 2000.

[53] Carl-Henrik Heldin and Bengt Westermark. Mechanism of action and in vivo role of platelet-derived growth factor. *Physiological reviews*, 79 4:1283–316, 1999.

[54] Ian C. Schneider and Jason M. Haugh. Quantitative elucidation of a distinct spatial gradient-sensing mechanism in fibroblasts . *Journal of Cell Biology*, 171(5):883–892, 11 2005.

[55] Krithika Mohan, Jamie L Nosbisch, Timothy C. Elston, James E. Bear, and Jason M. Haugh. A reaction-diffusion model explains amplification of the plc/pkc pathway in fibroblast chemotaxis. *Biophysical journal*, 113 1:185–194, 2017.

[56] Alexandra Jilkine and Leah Edelstein-Keshet. A comparison of mathematical models for polarization of single eukaryotic cells in response to guided cues. *PLoS Computational Biology*, 7, 2011.

[57] Alan Turing. The chemical basis of morphogenesis. *Philosophical Transactions of the Royal Society B*, 237:37–72, 1952.

[58] Akiko Nakamasu, Go Takahashi, Akio Kanbe, and Shigeru Kondo. Interactions between zebrafish pigment cells responsible for the generation of turing patterns. *Proceedings of the National Academy of Sciences*, 106:8429 – 8434, 2009.

[59] William R. Holmes, May Anne Mata, and Leah Edelstein-Keshet. Local perturbation analysis: A computational tool for biophysical reaction-diffusion models. *Biophysical Journal*, 108(2):230–236, 2015.

[60] B. Ermentrout. XPPAUT, 2016.

[61] William R. Holmes. An efficient, nonlinear stability analysis for detecting pattern formation in reaction diffusion systems. *Bulletin of Mathematical Biology*, 76:157–183, 2014.

[62] J. P. Kernévez, G. Joly, M Duban, Barry Bunow, and D. Thomas. Hysteresis, oscillations, and pattern formation in realistic immobilized enzyme systems. *Journal of Mathematical Biology*, 7:41–56, 1979.

[63] Leah Edelstein-Keshet, William R. Holmes, Mark Zajac, and Meghan Dutot. From simple to detailed models for cell polarization. *Philosophical Transactions of the Royal Society B: Biological Sciences*, 368(1629):20130003, 2013.

[64] B. Bozzini, G. Gambino, D. Lacitignola, S. Lupo, M. Sammartino, and I. Sgura. Weakly nonlinear analysis of turing patterns in a morphochemical model for metal growth. *Computers and Mathematics with Applications*, 70(8):1948–1969, 2015.

[65] Paul Becherer, Alexander N. Morozov, and Wim van Saarloos. Probing a subcritical instability with an amplitude expansion: An exploration of how far one can get. *Physica D: Nonlinear Phenomena*, 238(18):1827–1840, 2009.

[66] Khanh Gia Pham and Sergey A. Suslov. On the definition of landau constants in amplitude equations away from a critical point. *Royal Society Open Science*, 5(11):180746, 2018.

[67] Onn Brandman and Tobias Meyer. Feedback loops shape cellular signals in space and time. *Science*, 322:390 – 395, 2008.

[68] John J Tyson, Katherine C Chen, and Bela Novak. Sniffers, buzzers, toggles and blinkers: dynamics of regulatory and signaling pathways in the cell. *Current Opinion in Cell Biology*, 15(2):221–231, 2003.

[69] Carole A. Parent and Peter N. Devreotes. A cell's sense of direction. *Science*, 284 5415:765–70, 1999.

[70] Andre Levchenko and Pablo A. Iglesias. Models of eukaryotic gradient sensing: application to chemotaxis of amoebae and neutrophils. *Biophysical journal*, 82 1 Pt 1:50–63, 2002.

[71] Herbert Levine, David A. Kessler, and Wouter-Jan Rappel. Directional sensing in eukaryotic chemotaxis: a balanced inactivation model. *Proceedings of the National Academy of Sciences of the United States of America*, 103 26:9761–6, 2006.

[72] Yuan Xiong, Chuan-Hsiang Huang, Pablo A. Iglesias, and Peter N. Devreotes. Cells navigate with a local-excitation, global-inhibition-biased excitable network. *Proceedings of the National Academy of Sciences*, 107:17079 – 17086, 2010.

[73] Oliver Hoeller and Robert R. Kay. Chemotaxis in the absence of pip3 gradients. *Current Biology*, 17:813–817, 2007.

[74] Kosuke Takeda, Danying Shao, Micha Adler, Pascale G. Charest, William F. Loomis, Herbert Levine, Alex Groisman, Wouter-Jan Rappel, and Richard A. Firtel. Incoherent feedforward control governs adaptation of activated ras in a eukaryotic chemotaxis pathway. *Science Signaling*, 5(205):ra2–ra2, 2012.

[75] Orion David Weiner, William A. Marganski, Lani F. Wu, Steven J. Altschuler, and Marc W. Kirschner. An actin-based wave generator organizes cell motility. *PLoS Biology*, 5, 2007.

[76] Michael Weiger, Chun-Chao Wang, Matej Krajcovic, Adam T. Melvin, John J. Rhoden, and Jason M. Haugh. Spontaneous phosphoinositide 3-kinase signaling dynamics drive spreading and random migration of fibroblasts. *Journal of Cell Science*, 122:313 – 323, 2009.

[77] Hans Meinhardt. Orientation of chemotactic cells and growth cones: models and mechanisms. *Journal of cell science*, 112 (Pt 17):2867–74, 1999.

[78] Atul Narang. Spontaneous polarization in eukaryotic gradient sensing: a mathematical model based on mutual inhibition of frontness and backness pathways. *Journal of theoretical biology*, 240 4:538–53, 2006.

[79] Mikiya Otsuji, Shuji Ishihara, Carl Co, Kozo Kaibuchi, Atsushi Mochizuki, and Shinya Kuroda. A mass conserved reaction–diffusion system captures properties of cell polarity. *PLOS Computational Biology*, 3(6):1–15, 06 2007.

[80] Andrew B. Goryachev and Alexandra V. Pokhilko. Dynamics of CDC42 network embodies a Turing-type mechanism of yeast cell polarity. *FEBS Lett.*, 582(10):1437–1443, 11 2008.

[81] Masamitsu Iino and Makoto Endo. Calcium-dependent immediate feedback control of inositol 1,4,5-trisphosphate-induced ca2+ release. *Nature*, 360:76–78, 1992.

[82] R E Hagar, Angela D. Burgstahler, Michael H. Nathanson, and Barbara E. Ehrlich. Type iii insp3 receptor channel stays open in the presence of increased calcium. *Nature*, 396:81–84, 1998.

[83] Bert Ove Olofsson. Rho guanine dissociation inhibitors: pivotal molecules in cellular signalling. *Cellular signalling*, 11 8:545–54, 1999.

[84] Pablo A. Iglesias and Andre Levchenko. Modeling the cell's guidance system. *Science's STKE*, 2002:re12 – re12, 2002.

[85] James Dickson Murray. *Mathematical Biology I. An Introduction*. Springer, 2002.

[86] Yoichiro Mori, Alexandra Jilkine, and Leah Edelstein-Keshet. Wave-pinning and cell polarity from a bistable reaction-diffusion system. *Biophysical Journal*, 94(9):3684–3697, 2008.

[87] William R. Holmes and Leah Edelstein-Keshet. Analysis of a minimal rho-gtpase circuit regulating cell shape. *Physical biology*, 13 4:046001, 2016.

[88] Simple rho gtpase dynamics generate a complex regulatory landscape associated with cell shape. *Biophysical Journal*, 118(6):1438–1454, 2020.

[89] Heba Sailem, Vicky Bousgouni, Sam Cooper, and Chris Bakal. Cross-talk between rho and rac gtpases drives deterministic exploration of cellular shape space and morphological heterogeneity. *Open Biology*, 4(1):130132, 2014.

[90] Peter J M van Haastert, Ineke Keizer-Gunnink, and Arjan Kortholt. Coupled excitable ras and f-actin activation mediates spontaneous pseudopod formation and directed cell movement. *Molecular Biology of the Cell*, 28:922 – 934, 2017.

[91] Jean-Yves Tinevez, N. Ronald Cambrige Perry, Johannes E. Schindelin, Genevieve M Hoopes, Gregory D Reynolds, Emmanuel Laplantine, Sebastian Y. Bednarek, Spencer L. Shorte, and K. Eliceiri. Trackmate: An open and extensible platform for single-particle tracking. *Methods*, 115:80–90, 2017.

[92] Johannes E. Schindelin, Ignacio Arganda-Carreras, Erwin Frise, Verena Kaynig, Mark Longair, Tobias Pietzsch, Stephan Preibisch, Curtis T. Rueden, Stephan Saalfeld, Benjamin Schmid, Jean-Yves Tinevez, Daniel J. White, Volker Hartenstein, Kevin W. Eliceiri, Pavel Tomançak, and Albert Cardona. Fiji: an open-source platform for biological-image analysis. *Nature Methods*, 9:676–682, 2012.

[93] Frédéric Paquin-Lefebvre, Bin Xu, Kelsey L. DiPietro, Alan E. Lindsay, and Alexandra Jilkine. Pattern formation in a coupled membrane-bulk reaction-diffusion model for intracellular polarization and oscillations. *Journal of Theoretical Biology*, 497:110242, 2020.

[94] Boris Rubinstein, Brian D Slaughter, and Rong Li. Weakly nonlinear analysis of symmetry breaking in cell polarity models. *Physical Biology*, 9(4):045006, aug 2012.

[95] Martin Golubitsky and David G. Schaeffer. *Singularities and Groups in Bifurcation Theory*. Springer, New York, NY, 1985.

[96] B. Verd, A. Crombach, and J. Jaeger. Classification of transient behaviours in a time-dependent toggle switch model. *BMC Systems Biology*, 8:43, 2014.

[97] A. Jimenez, J. Cotterell, A. Munteanu, and J. Sharpe. A spectrum of modularity in multi-functional gene circuits. *Molecular Systems Biology*, 13(4):925, 2017.

[98] Jin Wang, Li Xu, Erkang Wang, and Sui Huang. The potential landscape of genetic circuits imposes the arrow of time in stem cell differentiation. *Biophysical Journal*, 99(1):29–39, 2010.

[99] Pablo A Iglesias and Peter N Devreotes. Biased excitable networks: how cells direct motion in response to gradients. *Current Opinion in Cell Biology*, 24(2):245–253, 2012. Cell regulation.

[100] Changji Shi, Chuan-Hsiang Huang, Peter N. Devreotes, and Pablo A. Iglesias. Interaction of motility, directional sensing, and polarity modules recreates the behaviors of chemotaxing cells. *PLOS Computational Biology*, 9(7):1–17, 07 2013.

[101] Shailaja Seetharaman and Sandrine Etienne-Manneville. Cytoskeletal crosstalk in cell migration. *Trends in Cell Biology*, 30(9):720–735, 2020.

[102] Benoit Ladoux, René-Marc Mège, and Xavier Trepat. Front–rear polarization by mechanical cues: From single cells to tissues. *Trends in Cell Biology*, 26(6):420–433, 2016.

[103] Akira Katsumi, Julie Milanini, William B. Kiosses, Miguel A. del Pozo, Roland Kaunas, Shu Chien, Klaus M. Hahn, and Martin Alexander Schwartz. Effects of cell tension on the small GTPase Rac . *Journal of Cell Biology*, 158(1):153–164, 07 2002.

[104] Pascale G. Charest and Richard A. Firtel. Big roles for small GTPases in the control of directed cell movement. *Biochemical Journal*, 401(2):377–390, 12 2006.

[105] Supriya Srinivasan, Fei Wang, Suzana Glavas, Alexander Ott, Fred Hofmann, Klaus Aktories, Daniel Kalman, and Henry R. Bourne. Rac and Cdc42 play distinct roles in regulating PI(3,4,5)P3 and polarity during neutrophil chemotaxis . *Journal of Cell Biology*, 160(3):375–385, 01 2003.

[106] Christine Chiasson-MacKenize and Andrea I. McClatchey. EGFR-induced cytoskeletal changes drive complex cell behavior: The tip of the iceberg. *Science Signaling*, 11:eaas9473, 2018.

[107] A.J. Ridley and A. Hall. The small GTP-binding protein rho regulates the assembly of focal adhesions and actin stress fibers in response to growth factors. *Cell*, 70:389–399, 1992.

[108] Dennis Bray. *Cell movements: from molecules to motility*. Garland Science, 2000.

[109] Liu Yang, Janet C. Effler, Brett L. Kutscher, Sarah E. Sullivan, Douglas N. Robinson, and Pablo A. Iglesias. Modeling cellular deformations using the level set formalism. *BMC Syst Biol*, 2(68):1–16, 2008.

[110] M. Mitchell. A toolbox of level set methods. *UBC Department of Computer Science Technical Report TR-2007-11*, 2007.

[111] Alexander X. Cartagena-Rivera, Jeremy S Logue, Clare M. Waterman, and Richard S. Chadwick. Actomyosin cortical mechanical properties in nonadherent cells determined by atomic force microscopy. *Biophysical Journal*, 110:2528 – 2539, 2016.

[112] Galya Orr, Dehong Hu, Serdar Ozcelik, Lee K. Opresko, H. Steven Wiley, and Steven D. Colson. Cholesterol dictates the freedom of EGF receptors and HER2 in the plane of the membrane. *Biophysical journal*, 89 2:1362–73, 2005.

[113] D. Lauffenburger and J.J. Linderman. *Receptors: model for binding, trafficking and signaling*. Oxford University Press, 1996.

[114] J. Ibach, Y. Radon, M. Gelleri, M.H. Sonntag, L. Brunsveld, P.I.H. Bastiaens, and P.J. Verveer. Single Particle Tracking Reveals that EGFR Signaling Activity Is Amplified in Clathrin-Coated Pits. *PLoS One*, 10(11):e0143162, 2015.

[115] Conrad Hal Waddington. *The strategy of the genes*. Routledge, 2015.

[116] Naomi Moris, Cristina Pina, and Alfonso Martinez Arias. Transition states and cell fate decisions in epigenetic landscapes. *Nature Reviews Genetics*, 17:693–703, 2016.

[117] Sui Huang, Gabriel S. Eichler, Yaneer Bar-Yam, and Donald E. Ingber. Cell fates as high-dimensional attractor states of a complex gene regulatory network. *Physical review letters*, 94 12:128701, 2005.

[118] Hannah H. Chang, Martin Hemberg, Mauricio Barahona, Donald E. Ingber, and Sui Huang. Transcriptome-wide noise controls lineage choice in mammalian progenitor cells. *Nature*, 453:544–547, 2008.

[119] Laurane De Mot, Didier Gonze, Sylvain Bessonnard, Claire Chazaud, Albert Goldbeter, and Geneviève Dupont. Cell fate specification based on tristability in the inner cell mass of mouse blastocysts. *Biophysical journal*, 110 3:710–722, 2016.

[120] Angel Stanoev, Christian Schröter, and Aneta Koseska. Robustness and timing of cellular differentiation through population-based symmetry breaking. *Development*, 148(3), 02 2021. dev197608.

[121] Akhilesh Nandan, Abhishek Das, Robert Lott, and Aneta Koseska. Cells use molecular working memory to navigate in changing chemoattractant fields. *bioRxiv*, 2021.

[122] Peter Friedl and Darren Gilmour. Collective cell migration in morphogenesis, regeneration and cancer. *Nature Reviews Molecular Cell Biology*, 10:445–457, 2009.

[123] Olga V. Ilina and Peter Friedl. Mechanisms of collective cell migration at a glance. *Journal of Cell Science*, 122:3203 – 3208, 2009.

[124] David Ellison, Andrew Mugler, Matthew D Brennan, Sung Hoon Lee, Robert J Huebner, Eliah R. Shamir, Laura A. Woo, Joseph B. Kim, Patrick Amar, Ilya Nemenman, Andrew Josef Ewald, and Andre Levchenko. Cell–cell communication enhances the capacity of cell ensembles to sense shallow gradients during morphogenesis. *Proceedings of the National Academy of Sciences*, 113:E679 – E688, 2016.

[125] Hamid Cheshmi. Glioblastoma microvesicles transport rna and proteins that promote tumour growth and provide diagnostic biomarkers. *New Cellular and Molecular Biotechnology Journal*, 1:75–88, 2011.

[126] Khalid Al-Nedawi, Brian M. Meehan, Johann Micallef, Vladimír Lhoták, Linda M. May, Abhijit Guha, and Janusz Rak. Intercellular transfer of the oncogenic receptor EGFRvIII by microvesicles derived from tumour cells. *Nature Cell Biology*, 10:619–624, 2008.

[127] Anna Kicheva, Periklis Pantazis, Tobias Bollenbach, Yannis Kalaidzidis, Thomas Bittig, Frank Jülicher, and Marcos Gonzalez-Gaitan. Kinetics of morphogen gradient formation. *Science*, 315:521 – 525, 2007.

[128] Harrison V Prentice-Mott, Yasmine Meroz, Andreas Carlson, Michal A. Levine, Michael W. Davidson, Daniel Irimia, Guillaume T. Charras, Lakshminarayanan Mahadevan, and Jagesh V. Shah. Directional memory arises from long-lived cytoskeletal asymmetries in polarized chemotactic cells. *Proceedings of the National Academy of Sciences*, 113:1267 – 1272, 2016.

[129] Hiroyuki Nakahara and Kenji Doya. Dynamics of attention as near saddle-node bifurcation behavior. In D. Touretzky, M.C. Mozer, and M. Hasselmo, editors, *Advances in Neural Information Processing Systems*, volume 8. MIT Press, 1995.

[130] M. G. Rabinovich, Ramón Huerta, and Gilles Laurent. Transient dynamics for neural processing. *Science*, 321:48 – 50, 2008.

[131] Kevin L. Briggman, Henry D. I. Abarbanel, and William B. Kristan. Optical imaging of neuronal populations during decision-making. *Science*, 307:896 – 901, 2005.

[132] Gouhei Tanaka, Toshiyuki Yamane, Jean Benoit Héroux, Ryosho Nakane, Naoki Kanazawa, Seiji Takeda, Hidetoshi Numata, Daiju Nakano, and Akira Hirose. Recent advances in physical reservoir computing: A review. *Neural networks : the official journal of the International Neural Network Society*, 115:100–123, 2019.

[133] Wolfgang Maass, Thomas Natschläger, and Henry Markram. Real-Time Computing Without Stable States: A New Framework for Neural Computation Based on Perturbations. *Neural Computation*, 14(11):2531–2560, 11 2002.

[134] Anne Brunet, Azad Bonni, Michael J. Zigmond, Michael Z. Lin, Peter Juo, Linda S. Hu, Michael James Anderson, Karen C. Arden, John Blenis, and Michael Eldon Greenberg. Akt promotes cell survival by phosphorylating and inhibiting a forkhead transcription factor. *Cell*, 96:857–868, 1999.

[135] Hyunryul Ryu, Minhwan Chung, Maciej Dobrzyński, Dirk Fey, Yannick Blum, Sung Sik Lee, Matthias Peter, Boris N Kholodenko, Noo Li Jeon, and Olivier Pertz. Frequency modulation of erk activation dynamics rewires cell fate. *Molecular Systems Biology*, 11(11):838, 2015.

[136] Marc-Antoine Jacques, Maciej Dobrzyński, Paolo Armando Gagliardi, Raphael Sznitman, and Olivier Pertz. Codex, a neural network approach to explore signaling dynamics landscapes. *Molecular Systems Biology*, 17(4):e10026, 2021.

[137] Thomas M. Cover and Joy A. Thomas. *Elements of Information Theory*. Wiley-Interscience, 1991.

[138] Raymond Cheong, Alex Rhee, Chiaochun Joanne Wang, Ilya Nemenman, and Andre Levchenko. Information transduction capacity of noisy biochemical signaling networks. *Science*, 334:354 – 358, 2011.

[139] Ryan Suderman, John A. Bachman, Adam Smith, Peter K. Sorger, and Eric J. Deeds. Fundamental trade-offs between information flow in single cells and cellular populations. *Proceedings of the National Academy of Sciences*, 114:5755 – 5760, 2017.

[140] Jangir Selimkhanov, Brooks Taylor, Jason Yao, Anna Pilko, John G. Albeck, Alexander Hoffmann, Lev S. Tsimring, and Roy Wollman. Accurate information transmission through dynamic biochemical signaling networks. *Science*, 346:1370 – 1373, 2014.

[141] Amir Erez, Tommy A. Byrd, Michael Vennettilli, and Andrew Mugler. Cell-to-cell information at a feedback-induced bifurcation point. *Physical review letters*, 125 4:048103, 2020.

[142] Robert T. Wicks, Sandra C. Chapman, and Richard Dendy. Mutual information as a tool for identifying phase transitions in dynamical complex systems with limited data. *Physical review. E, Statistical, nonlinear, and soft matter physics*, 75 5 Pt 1:051125, 2007.

Acknowledgements

There are many people without whom this thesis would have been difficult, less enjoyable, or would not even exist. First and foremost: I would like to acknowledge the relentless support and encouragement that Dr. Aneta koseska has given me over the years. I will be forever grateful for your patience and especially for not postponing a single query irrespective of the time of the day and day of the week.

I would like to thank Prof. Dr. Philippe Bastiaens for the generous support throughout these years, for being part of my thesis advisory committee (TAC), discussions, and for providing a fantastic work environment in the department together with Dr. Peter Beiling, Dr. Christian Schröter, and Dr. Aneta Koseska. I would like to also thank Prof. Dr. Carsten Beta for being in my TAC and for giving valuable scientific inputs.

Next to my colleagues in the lab: Abhishek das for sharing a great deal of knowledge during our collaborative work that shaped the most important paper of our Ph.D. Manish and Robert for the fruitful scientific and non-scientific discussions. Angel stanoev who played a crucial role in the initial years of my Ph.D., a big thanks to you for being always listening and ready to help.

To my colleagues in the Department: people who were always welcoming and interacting. I had a great time with all of them. To mention a few: Sven who was always available to help with the microscope so patiently, over and over again! Kirsten, Manuella from Dortmund, and Antje from Bonn for always being kind and helpful in the lab. Dhruv, Mike, Marina, Hans for always welcoming me with big smiles. Farid for showing that one can watch and enjoy Japanese anime with German subtitles (two languages that he has no idea about). Office mates: Sarah and Mai for the fun-filled, random discussions that fueled the years.

Thank you Christa, Lucia, the IMPRS-LM faculty members, and students. Being part of the school was an honor and an enjoyable experience. Thank you Astrid and Tanja for the support and organization within the department.